**Dissertation**
**submitted to the**
**Combined Faculties for the Natural Sciences and for Mathematics**
**of the Ruperto-Carola-University of Heidelberg, Germany**
**for the degree of**
**Doctor of Natural Sciences**

presented by


| | |
|---|---|
| Dipl.-Inform. Med.: | Ralf B. Schulz |
| born in: | Munich, Germany |


Oral examination: July, 19$^{th}$, 2006

# Development of a Non-Contact Fluorescence Tomography System with Appropriate Reconstruction Techniques

Referees: Prof. Dr. Dr. Wolfhard Semmler
Prof. Dr. Fred Hamprecht

# Zusammenfassung

Molekulare Bildgebung ist ein aktuelles Forschungsgebiet, das auf der Kombination hochspezifischer Kontrastmittel mit passenden Bildgebungstechniken beruht. Sie beschäftigt sich hauptsächlich mit der Erprobung neuartiger Pharmazeutika an kleinen Tieren und ermöglicht die tägliche Beobachtung des Therapiefortschritts am lebenden Tier. Unter den verfügbaren Bildgebungsmodalitäten erfreuen sich fluoreszenzbasierte Techniken großer Beliebtheit, da zugehörige Experimente einfach durchzuführen und zahlreiche Kontrastmittel für den experimentellen Einsatz verfügbar sind. Da Licht im biologischen Gewebe stark gestreut wird, sind aufgenommene Bilder der Fluoreszenz jedoch stark von deren Gewebetiefe abhängig, so dass Bilder nicht untereinander verglichen werden können. Die fluoreszenzbasierte Tomographie (FMT) verspricht diesen Nachteil zu beheben, da sie als quantitative Bildgebungstechnik die Konzentrationsbestimmung von Fluorochromen in vivo erlaubt. Üblicherweise verwenden FMT-Geräte Lichtleiter als Detektoren, die am zu bildgebenden Tier befestigt werden. Neuerdings wurden jedoch berührungsfreie Methoden entwickelt, bei denen von einer CCD-Kamera aufgenommene Bilder als Projektionsdaten verwendet werden. Eine hierin präsentierte Studie zum Vergleich von lichtleiterbasierter und berührungsfreier Bildgebung zeigt zum ersten Mal zuverlässig die überlegenen Eigenschaften der berührungsfreien Technik. Auf diesen Erkenntnissen aufbauend wurde ein neuartiges, berührungsfrei arbeitendes Tomographiesystem für kleine Tiere entwickelt. An Phantomen wie auch anhand einer Tierstudie werden die Fähigkeiten des Gerätes zur Rekonstruktion fluoreszierender Quellen in diffusen Medien gezeigt.

# Abstract

Molecular Imaging is a highly topical research field based on the combination of highly selective markers and appropriate imaging devices. It is mainly concerned with studying the effects of prototype drugs in small animals, following day by day the evolution of the disease in vivo. Amongst the imaging techniques available, fluorescence based imaging is very popular due to the simplicity of the experimental systems and the widespread availability of suitable probes. As however light is heavily scattered in tissue, fluorescence images depend heavily on the inclusion depth so that different images cannot be compared. Fluorescence mediated tomography (FMT) as presented herein is hoped to overcome these shortcomings by providing a quantitative means of estimating fluorochrome concentrations in vivo. Usually, FMT-systems rely on detector readings obtained through light guiding fibers mounted in contact to the imaged animals. Recently, non-contact methods have been proposed, allowing CCD-camera images to be used as projection data. Herein, a study is presented comparing fiber-based and non-contact imaging methods and reliable indicates for the first time the superiority of non-contact techniques. Based on these findings, a novel non-contact tomography system for small animals was developed. In phantoms as well as in an animal study the capabilities of the system to reconstruct fluorescent sources in turbid media are demonstrated.

To my parents
and all the countless people
who have accompanied me on this long journey

When I can look Life in the eyes,
Grown calm and very coldly wise,
Life will have given me the Truth,
And taken in exchange—my youth.
*Sara Teasdale*

# Acknowledgments

MANY are those who helped me in working on the experiments or results presented in this thesis; may it be with new ideas, may it be with experimental support, mechanically preparing system parts, or with food and love, or even travel grants.

First of all, my deepest thanks go to my advisers, Prof. Dr. Dr. Wolfhard Semmler from the German Cancer Research Center (dkfz) and Prof. Dr. Fred Hamprecht from the physics faculty of the university of Heidelberg for accepting me as their PhD student, for enabling the creation of this work, and for giving me the freedom to proceed in any way possible without too many bound constraints. It was a great pleasure to work in the group of Dr. Jörg Peter together with Dr. Oliver Nix, Wolfram Stiller, and Daniel Unholtz. For experimental support when living animals were concerned, I have to acknowledge the help and expertise of Dr. Fabian Kießling and Dr. Manfred Jugold.

I got addicted to the field of biomedical optics while preparing my diploma thesis at the Center for Molecular Imaging Research in Boston, MA, USA, under Prof. Vasilis Ntziachristos, Dr. Jorge Ripoll, and Prof. Ralph Weissleder, whom I also owe a heartfelt thank-you for a great time in Boston, and the many doors this stay opened for me after my return to Germany.

All computations on finite element meshes were performed using the great DEAL.II library developed by Dr. Wolfgang Bangerth, Dr. Guido Kanschat, and Dr. Ralf Rannacher [21]. This library not only is very well written and fast, it is also freely available and support in most cases is immediate and helpful.

Without Heinrich Rühle, Volker Stamm, Dietbert Bucher, Wolfgang Stroh, and the other staff from the mechanics workshop at dkfz, the experimental setups presented herein could not have been set up, manufactured, or improved in such excellent quality and precision. Jürgen Vierling, Thomas Vogt, and the other staff from the electronics workshop at dkfz helped in creating the necessary control electronics for the tomographic scanner. Gernot Echner and Clemens Lang prepared the first CAD drawings of the animal scanner's imaging chamber.

Then there is the laboratory of Prof. Rinaldo Cubeddu, where I not only had the opportunity during a couple of weeks to learn a lot about how good research

should be performed, but also met an abundance of helpful and knowledgeable people, whom I now consider good friends, namely Prof. Dr. Cosimo D'Andrea, Prof. Dr. Gianluca Valentini, Dr. Daniela Comelli, Prof. Dr. Paola Taroni, Prof. Dr. Alessandro Toricelli, Dr. Andrea Bassi, and—last but not least—the man who built numerous apparatus and made nearly everything possible by his machining skills, Luciano Pallaro. The work I was able to perform in their lab is presented in chapter 4.

Further thanks and acknowledgments have to go to my Chinese friends from Huazhong University of Science and Technology in Wuhan, P.R. China, whom I had the opportunity to work with for a couple of weeks. Namely I have to thank Prof. Dr. Qingming Luo, the head of the lab, for inviting me to Wuhan, and Shangbin Chen for letting me participate in his experimental work.

Last but not least, I am very grateful for very helpful and friendly support by Sabine Fritz in all aspects of the logistics concerned in performing PhD research. Also, many thanks go to her husband, Roland Fritz, for support in Latin and ancient Greek.

This thesis was in part supported by a PhD scholarship of the German Cancer Research Center (dkfz), by the EU Laserlab Network under contract RII3-CT-2003-506350 (collaboration with the Politecnico di Milano, Italy), the Boehringer Ingelheim Foundation which allowed me to stay for five weeks at the Key Laboratory for Biomedical Photonics in Wuhan, P.R. China, and Siemens Preclinical Solutions (formerly CTI imaging) who awarded me with a 500$ travel grant to attend the 2005 IEEE Medical Imaging Conference in Fajardo, Puerto Rico.

The document was typeset in LaTeX using Adobe's Utopia font and the text managing IDE TeXnicCenter, a very useful piece of freeware that can be obtained from the developers' web page at `http://www.toolscenter.org`.

# Contents

# Chapter 1.

# Motivation and Introduction

Die Farben sind Taten des Lichts,
Taten und Leiden.

*(Johann Wolfgang v. Goethe, Zur Farbenlehre)*

## 1.1. Overview

OPTICAL TOMOGRAPHY, sometimes more correctly referred to as *Diffuse Optical Tomography* (DOT) [25], in the context of the work presented herein is a tomographic* imaging technique using low energy photons to probe a volume of unknown properties. For imaging of biological tissues, usually photons in the visible or near infrared range are employed, i.e., between approximately 400nm and just over 1000nm. Photons are injected into the imaged object at a certain position, they propagate through the probed volume and either are absorbed or eventually leave the volume through the object's exterior boundaries. Photon detection is performed on or outside the exterior boundaries, yielding *diffuse projection data*. Acquired projection data can then be used in an inverse model of photon propagation to obtain an estimated spatial map of the optical properties within the volume. This process is called *reconstruction*. Nowadays, extensive literature exists on the subject of optical tomographic techniques. For instance, refer to [25, 89] for introductory literature and a list of current articles and reviews.

In principle, optical tomography is closely related to X-ray computerized tomography (CT) as both techniques use photons that propagate through an object of interest. However, as the photon energies employed for transillumination differ by 3–4 orders of magnitude (from eV for optical photons to $10^4$–$10^5$eV for X-rays), photon propagation patterns are significantly different. Unlike CT, the low-energy photons used in optical tomography do not propagate along straight lines, but are heavily scattered, constantly changing their direction of propagation. Thus, more complex inversion algorithms and mathematical models than the inverse Radon

*tomography, from Greek $\tau o \mu o \varsigma$, meaning *section*, and $\gamma \rho \alpha \varphi \varepsilon \iota \nu$, meaning *to write*

transform used for CT [50] are necessary. The most commonly used model, the diffusion equation, will be derived in chapter 2.

If not the intrinsic properties of tissues are of interest but the presence of light-emitting contrast agents, i.e., fluorochromes, the according emission tomographic imaging technique is called *Fluorescence Mediated Tomography* (FMT)[†]. It is especially of importance in the field of molecular imaging, when fluorescence labeled tumor cells need to be imaged. Molecular imaging is a highly topical research field based on the combination of highly selective markers and imaging devices [22]. The main scope of molecular imaging is to study the treatment effects of prototype drugs to treat cancer in small animals, following the day by day evolution of the disease without sacrificing the animals. Amongst the techniques available, optical imaging based on fluorescence is one of the most popular due to the simplicity of the experimental systems and the widespread availability of suitable probes [59, 79]. Molecular imaging will be discussed in detail in section 1.3.

FMT does not require conceptually different image reconstruction algorithms than DOT, but the algorithms used require adaptation to make use of the additionally available information due to the presence of a fluorescence signal. These algorithms will be derived and discussed in chapter 2.

As described below in section 1.2, different detection techniques can be used for acquiring projection data in DOT. Classically, a couple of optical fibers fixed on the imaged object are used. However, over the past few years, also the idea of acquiring projection data with a standard camera system was developed, i.e., imaging through an objective lens. This type of detection is termed *non-contact detection*. The motivation behind using a camera instead of fibers is simple: not only is this approach far easier to calibrate, use, and maintain, as will be shown later on, but it also promises to increase resolution in reconstructed images due to the availability of more detectors—every pixel of a camera could act as a detector. The motivation behind non-contact imaging will be detailed further below, in section 1.2.

Characterizing the properties of non-contact detection and making use of possible advantages over classic approaches in the field of molecular imaging of small animals is the key motivation behind this thesis. The following sections of this chapter will introduce basic terms of optical imaging and photon scattering, and will also give the motivation why to perform optical tomography. Then, in chapter 2, the standard models of photon propagation in tissue are briefly introduced, in particular the diffusion equation. Subsequently, the concept of detection operators is introduced, which facilitates the comparison between standard, fiber-based tech-

[†]Unfortunately there are a number of synonymous terms in use by different researchers. Some authors refer to the technique as fluorescence molecular tomography [38, 67], fluorescence tomography [34, 49, 55], fluorescence(-enhanced) optical tomography [37], or even fluorescence optical diffusion tomography [60]. Herein, the technique will always be named FMT.

niques and non-contact models (chapter 3). Following the theoretical introduction, a comparative study on fiber-based versus non-contact detection is presented and discussed in chapter 4. The results obtained from this study were used in the development and construction of a tomographic imaging system dedicated to small animal imaging, presented and discussed in chapter 5.

All of the results presented in the experimental chapters 4 and 5 are based on a commonly employed reconstruction algorithm called the *normalized Born approximation*. However, the use of alternative algorithms using the same non-contact detection method will be discussed in chapter 3. Results obtained from the experimental studies indicate that non-contact detection offers acquisition of better quality signals, without increasing the complexity of the inverse problems. These results will be valid for any other reconstruction technique as well. The discussion of the results and their implications can be found in chapter 6.

The equations given herein try to follow standard conventions wherever possible. However, in many cases, there are numerous different notation variants being used in the field of diffuse optics. A list of symbols and notations frequently used in this work can be found at page 119 ("List of Symbols and Expressions").

## 1.2. Fluorescence Mediated Tomography (FMT)

### 1.2.1. Description of the Technique

Tomographic imaging is defined as the mathematical recovery of a three-dimensional map of the parameter of interest (*reconstruction*) within the imaged subject by use of data acquired outside of the imaged specimen (*projection data*). For FMT, the parameter of interest is the distribution / concentration of fluorochromes. Projection data is acquired by (trans-)illuminating the imaged object with light at the fluorochrome's excitation wavelength, thus exciting the fluorochrome hidden within the object. The source's photon distribution is changed over time to increase the amount of information obtained. In practice, this is performed by illuminating with a pencil beam, e.g., a collimated laser source, whose point of incidence is varied. Using some kind of photon detector the amount of photons leaving the object through its exterior boundaries (*exitance*) can be acquired at different positions, and photons discriminated by their wavelength through an optical filter to distinguish between photons from the source (excitation) and those emitted by the fluorochrome (fluorescence).

Common setups for optical tomography employ light guiding fibers either in contact with the imaged object itself or with an imaging chamber in which the object is immersed in a diffuse fluid matching the object's mean optical properties (figure

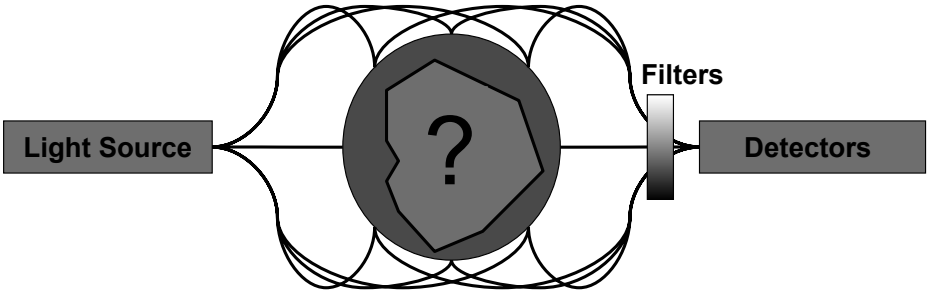


**(a)** Fiber-based setup. The imaged object is usually immersed in a fluid of known properties (intralipid + absorber), filling a volume of known shape (here illustrated by a circular shape).

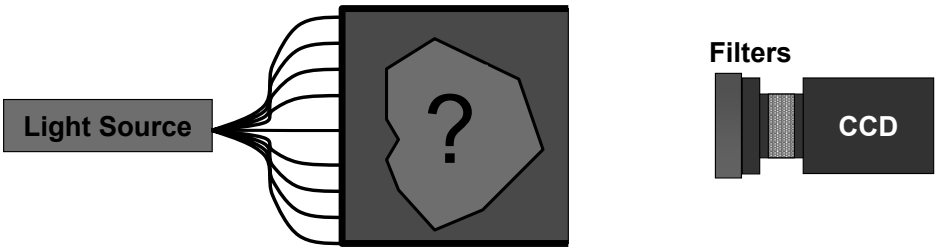


**(b)** High resolution setup. The acquisition of many detector readings by use of a CCD chip providing thousands of pixel readouts enables higher spatial resolution, as even very closely located detectors collect slightly different information [27, 39, 38].

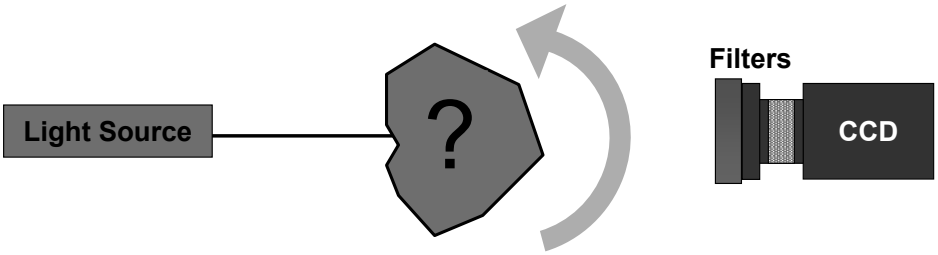


**(c)** Non-contact setup. Different source-detector combinations become available by rotating the object, or rotating the setup around the object, as indicated by the arrow. This type of setup is easy to build and imaging is easy to perform, but boundary effects have to be treated carefully in the mathematical model. Possibly, this type of setup enables high spatial resolution, as many detectors are available and no matching fluid is needed, improving overall attenuation [5].

**Figure 1.1:** Overview of different setup types for optical tomographic imaging.

1.1a). The use of imaging chambers has the advantage of fixing the geometry of the diffuse domain to a slab or a cylinder, which simplifies the incorporation of boundary conditions for the diffusion equation involved in the reconstruction process. For details, please refer to chapter 2. Fibers are used as light sources or to detect photons on the object's or imaging chamber's exterior boundaries. As the number of available fibers is generally limited due to spatial constraints and the significantly increasing complexity of experimental setups involving an large number of fibers, the achievable spatial resolution of the method is usually limited to a few millimeters [5]. Considering the overall dimensions of small animals such as mice and rats, however, high spatial resolution of better than 1mm is desirable.

It has been shown that most of these limitation can be overcome using an imaging chamber of slab-like geometry, where one side of the chamber is replaced by a translucent window through which images can be acquired by a CCD camera instead of fiber detectors, figure 1.1b [27, 38, 39]. Alternatively, in more microscopic setups, as for example for murine brain imaging, also a thick fiber bundle could be used to guide the light onto a CCD [28]. As excitation is now only performed from one side of the object (the slab shaped chamber, or the murine brain, respectively), where source fibers are mounted, available projection angles are reduced from 360° in cylindrical geometry to—in case of the slab-like chamber—approximately 120°. Nevertheless, an imaging resolution of better than 1mm has been reported [39].

Additionally, different models to incorporate boundary conditions for objects of arbitrary shape have been proposed that enable camera-based detection (also called "non-contact detection") without fixed-geometry systems and matching fluids [2, 5, 23, 43]. These are supposed to increase sensitivity, improve the spatial resolution, and increase the overall quality of the detected signals as more detector readings become available, the additional scattering and attenuation by matching fluids is eliminated and fiber coupling issues are resolved. However, for these non-contact setups the ability to quantify fluorochrome concentration has not yet been shown. Furthermore, a fair comparison between fiber-based and non-contact data sets, investigating the possible advantages of non-contact detection itself without additionally changing the theoretical framework—by using different types of boundary conditions and the like—has not yet been performed to the best of the author's knowledge. In chapter 4 results from both imaging methods are presented and discussed which have been obtained under similar experimental conditions. Subsequently, in chapter 5, a small animal imaging device for fully non-contact tomography is presented.

### 1.2.2. Tissue Optics

To understand the fundamental obstacles optical imaging techniques have to overcome for biological tissues, one has to consider the optical properties of tissue. Biological tissues are comprised of millions of cells that exhibit an abundance of different structures (membranes, organelles, etc.) having different optical densities [33]. These structures cause photons with wavelengths in the order of the structure size to scatter. Additionally, some molecules inside cells are also chromophores, like hemoglobin, desoxyhemoglobin, or cytochrome that absorbs light of certain wavebands [31].

Tissues are therefore highly scattering and absorbing for photons in the visible range. While tissue is strongly absorbing ($\mu_a \gg \text{cm}^{-1}$) for light of short wavelength (< 600nm) due to the absorption spectra of intracellular chromophores, light in the near infrared range (NIR) between 600nm and 900nm can penetrate several centimeters deep into tissue [66], as $\mu_a < 0.5\text{cm}^{-1}$, even down to $\mu_a \approx 0.1\text{cm}^{-1}$. In this wavelength region, the absorption due to water is not yet dominant (this is the reason for the wavelength range to be called also "water window") [93], in contrast to the terahertz or microwave regime where tissue imaging becomes extremely difficult. This has led to the development of an abundance of fluorescent molecules that emit in the NIR range; however, in general these fluorochromes are less efficient and less bright than their short-waved counterparts. This also implies that for each specific application the wavelength has to be chosen very carefully: in a more absorbing wavelength range the increase in efficiency and stability of the molecules might outweigh the disadvantages of higher absorption.

The main problem when using visible photons, however, is not attenuation but scattering, with a scattering coefficient in the order of $\mu_s \approx 100\text{cm}^{-1}$—about four orders of magnitude stronger than the absorption—, yielding a mean free path of only 0.1mm. As mentioned before, scattering is caused by the many different diffracting interfaces present in the cells of which tissue is comprised. Light scattering in cells is highly anisotropic with an average scatter angle of less than 25° [33]. The anisotropy $g$, which is introduced in chapter 2.1 and defined as the expected cosine value of the scattering angle therefore is in the order of 0.9. A current and comprehensive review of the optical properties of different tissue types and cell chromophores, as well as sources of tissue autofluorescence and fluorescence properties of single biomolecules can be found in the review by Stratis-Cullum et al [85].

Standard methods for scatter reduction as known for example from nuclear imaging [54] will fail for optical photons due to the extreme number of scattering events photons have undergone during their propagation through tissue. The scattering probability decreases a bit with longer wavelengths, but otherwise remains

relatively constant over the visible range (contrary to the sharp absorption peaks present in tissue due to biological chromophores).

When choosing an appropriate fluorochrome or the optimal wavelength for a specific imaging purpose there is also another, counter-intuitive effect one might have to take into account: the choice of a wavelength in a strongly absorbing region will result in the preferential detection of photons that have undergone fewer scattering events, as scattering increases the length of the propagation path, and the higher absorption will suppress the detection photons propagating for too long. Thus, scattering can be significantly reduced—however, signal intensities are decreased as well.

### 1.2.3. Fluorescence

The term *fluorescence* refers to the emission of a photon caused by a molecule's transition from an excited electronic state to (usually) its ground state [75]. Both states have the same spin multiplicity, which makes fluorescence a singlet-singlet-transition. Fluorescent molecules often consist of a more or less long chain of carbon atoms between two aromatic structures, which as a whole acts as an optical resonator. The length of the chain is related to the emission wavelength.

The excited state is reached by absorption of a photon with sufficient energy, i.e., of a photon of higher energy (shorter wavelength) than the energy difference between excited and ground state. The wavelength difference between the wavelength of maximum absorption and the emission wavelength is called *Stokes shift*. The lifetime of the excited state is termed *fluorescence lifetime* $\tau$ [s] and usually amounts to a timespan between some 100ps to several nanoseconds. The probability that the transition from excited to ground state will lead to the emission of a photon, instead of the energy being thermally lost, is called *quantum yield* $\gamma$ and is a measure of the fluorochrome's efficiency. The absorption efficiency is described by the *Molar extinction coefficient* $\varepsilon$ [$\mathrm{Mol}^{-1}\mathrm{cm}^{-1}$]. The total absorption created by the fluorochrome can be calculated using the relation $\mu_a = \varepsilon c$, where $c$ [Mol/l] is the fluorochrome concentration. It is important that all these factors, including the spectra, are influenced by the chemical environment (pH value, etc.) which could be exploited for imaging purposes.

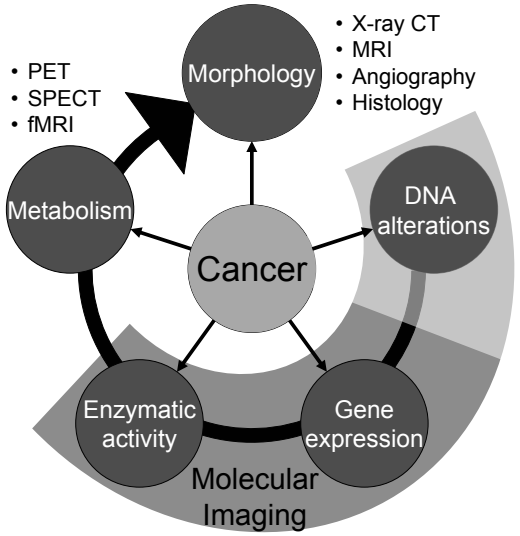


**Figure 1.2:** In the context of cancer it is hoped that molecular imaging will enable early diagnosis and detection of treatment efficacy. Cancer is a disease caused by DNA alterations in individual cells, changing the cell's internal metabolic activities and finally leading to uncontrolled cell multiplication. This will in turn alter tissue function as healthy tissues are more and more infiltrated by defunct cells, and in the end cause a change in morphology, e.g., a detectable tumor mass. Classic techniques enable imaging of morphological or functional aberrations, whereas molecular techniques target intracellular changes occurring at an earlier timepoint, as illustrated in the figure.

## 1.3. Molecular Imaging

### 1.3.1. Definition

The term *molecular imaging* was defined by Wagenaar, Weissleder, and Hengerer as

> "[...] the *in vivo*[‡] characterization and measurement of biologic processes at the cellular and molecular levels [...]" [90].

Measuring processes at cellular or molecular levels does not imply measuring with cellular, subcellular, or even molecular resolution. In fact, none of the molecular imaging techniques available today has a resolution anywhere near to microscopy, which is usually not an *in vivo* technique but often requires slicing and preparation of the specimen under investigation.

[‡]The Latin term *in vivo* translates to "within a living organism" and is the contrary to *ex vivo*. It emphasizes the fact that the imaged specimen has to stay alive, which is not the case for most microscopic imaging applications. The term, however, does not necessarily imply non-invasiveness.

In the context of cancer diagnostics, it is especially desirable to identify cancerous tissue as early as possible in the development of the disease, as survival rates strongly depend on tumor staging and grading. Tumor staging, which is a measure for the size and the stage of the disease, is usually performed using the TNM classification, where *T* describes size and healthy tissue infiltration of the primary tumor, *N* accounts for infiltrated lymph nodes, and *M* describes the presence of metastases [84]. Tumor grading, on the other hand, measures the malignity of tumors and is usually performed by histology; a typical example for tumor grading is the Gleason score used to grade prostate cancer [36].

Regarding treatment, it would be advantageous to detect whether or not a treatment actually induces a therapeutic response; noticing a lack of response within days after beginning of the treatment could then be used to switch to alternative treatments or to increase pharmaceutical dosage. A tractable therapeutic response is of course a decrease in tumor mass; however, this morphologically detectable response takes weeks or months to occur. The molecular response in the cells involved, on the other hand, occur within hours or days after the beginning of treatment. One of these responses is "programmed cell death", *apoptosis*, which could for instance be imaged using the so-called Annexin V marker [73].

For both applications, diagnostics and therapeutics, molecular imaging is of particular interest, as it targets genetic and functional changes on a cellular level, at least as far as sensitivity is concerned. Neoplasms[§] originate from a mutational change in cell DNA, which induces a change in gene expression and subsequently in cell function, expressed by its enzymatic activity (see also figure 1.2). When, due to this change in DNA, cells start to multiply in an uncontrolled fashion, the pure cell mass and occurring infiltration of healthy tissues will start to affect the overall tissue function. This is the earliest point in time when classical approaches, such as morphologic or functional imaging, will be able to detect abnormalities. However, detectable neoplasms have already grown to a size at least in the order of the voxel resolution of the imaging technique used, i.e., in the order of millimeters.

Molecular imaging techniques, it is hoped, can overcome this limitation in resolution by using special contrast agents that increase imaging contrast with respect to certain processes in the cells looked at. Such contrast agents are called "molecular probes". To perform molecular imaging the following three entities are required, according to Massoud [59]:

1. **Biological target specifically related to a certain disease or other process**
   Biological targets can be basically any molecule or molecular interaction occurring in cells, in particular receptors [56, 57, 94], enzymes [68], protein-

[§]An abnormal growth of tissue serving no physiological function; in this case synonymously used for tumor.

protein interactions [74], or the activation and deactivation of whole genes [1, 46]. In some applications even cells themselves become targets, e.g., when their movement through an organism is of interest (cell trafficking), as in current stem cell studies [95].

2. **Highly specific probe with a sufficient biodistribution toward the target**
   When looking for structures present in only a few cells, contrast is obviously of utmost importance. False positive signals which result from unspecific binding of the probe to a non-target biomolecule will decrease the significance of resulting images. While high specificity reduces false positive signals, false negative signals result from the inability of probe molecules to bind to the target, or to even reach the target in the body. Probe molecules thus need sufficient kinetic properties in the body and also must be able to cross any blood-tissue barriers involved.

3. **Imaging modality with sufficient sensitivity and low background signal**
   Again, resolution is not utterly important; but it is desired to enable detection of the signal created by only a single cell. For receptor imaging for instance it is desirable to have detection capabilities in the region of picomoles per liter (pMol/l).

The determination of biological targets (1.) is independent of the imaging strategy employed, while the choice of the imaging method (3.) is not. Probe development also needs to take into account the desired modality, as a probe usually consists of two parts, one to bind to the target and one to increase contrast or produce a signal. With respect to optical imaging techniques, a large number of optical probes do exist for in vitro imaging, i.e. for imaging cells in culture using microscopic techniques or similar. As far as the availability of in vivo imaging strategies is concerned, usually so-called *planar techniques* come into play. For these techniques, usually a sensitive CCD-camera is used to acquire images of the specimen. For bioluminescence applications, no excitation is necessary in this case: Specimen and detecting camera just have to be placed in a light-tight chamber as the detectable light intensities are very low, and so any possible source of stray light has to be eliminated. For probe systems based on fluorescence, excitation light is usually applied from the same view as the camera. The camera then detects reflected fluorescence signal through a set of filters optimized for the fluorochrome's emission spectrum. Fluorescence is more difficult to image than bioluminescent signals due to the presence of autofluorescence [85] in tissues.

While both techniques, planar bioluminescence and fluorescence imaging, are very sensitive—usually, a sensitivity in the 100-femtomolar range is stated in the

literature [93]—, acquired images do not yield information about the depth of inclusions detected in planar images of tissue, nor about the actual concentration of probe molecules that accumulated there. Light intensities recorded on the exterior boundaries of a diffuse object are heavily surface-weighted.

In other words, depth and concentration are intertwined properties, the problem of determining both of them at the same time is not unique. This can be illustrated very easily: Imagine any light intensity distribution of emitted fluorescence light as measured on the outer boundaries of the specimen. This light distribution was created by the excitation of probe distributed inside the specimen. There is always at least one other possible distribution of probe leading to the same intensities; all fluorescent molecules could be superficially located, with a concentration matching the measurement intensities. Note that this problem of non-uniqueness is the same for radiographic projection images as well, where the exact depth of detected absorbers is unknown, but because there is nearly no scattering, at least the measured absorption values are accurate independent of the actual absorber location.

However, for optical tomographic techniques where point sources located at different positions are used sequentially for fluorochrome excitation, the uniqueness of the inverse problem regarding the determination of concentration *and* localization of fluorescent inclusions has been shown theoretically [19]. This is also the main motivation for the use of optical tomography in the context of molecular imaging.

### 1.3.2. Optically Active Molecular Probes

According to Weissleder [92], the following types of optical probe systems can be distinguished:

- **Compartmental fluorescent probes**
  Fluorescent molecules are applied to a certain compartment of the body, e.g., the vascular system, and their distribution is imaged. This is the classical contrast agent approach and only of minor interest for molecular imaging.
- **Targeted Probes**
  A fluorescent molecule is attached to, for example, an antibody that binds specifically to some kind of biochemical target, e.g., a cell receptor. After metabolic clearance of the unbound probe, only probe molecules bound to a receptor still emit a signal and thus the receptor distribution can be imaged. In general, the concentration of bound probe particles should relate to the concentration of that specific receptor, if target-probe binding occurs with sufficient specificity.

- **Activatable probes**
  Activatable probes are used, for instance, to detect enzymatic[¶] activity. Fluorescent molecules will quench if located very close to each other due to resonant energy transfer in addition with thermal loss. If these quenched molecules become spatially separated however, quenching will be stopped and fluorescence can be detected again. This effect can be used to detect any process that involves structural changes of a molecule on which two resonant molecules could be placed. Such a structural change is, for example, enzymatic cleavage of a peptide where the peptide is cut in two parts at a specific location. If resonant fluorescent molecules are placed close enough on the opposite sides of the cleavage site, fluorescence will occur only after cleavage. If the cleavage is specifically induced by a certain enzyme, the detectable signal is directly related to the activity of that enzyme.

Furthermore, there are two other approaches available that employ endogenous probes (i.e., probes internally synthesized by the cells), namely

- **Bioluminescence**
  The light emitted by fireflies, as observable on warm summer evenings, is created by a biological process known as *bioluminescence*. It originates from the activity of an enzyme called firefly luciferase, which metabolizes a substance named luciferin under photon emission. Other types of luciferase have been discovered in deep sea organisms. The biological systems looked at in molecular imaging research—which are mostly mice and rats or other vertebrae—do not exhibit bioluminescence. This enables researchers to genetically engineer cells to produce luciferase; if these cells are introduced to a host system, and if luciferin is then applied to the host, bioluminescent signals from these engineered cells may be observed. If the luciferase gene is inserted in a specific gene of the cell, bioluminescence can only occur when this gene is activated, as otherwise no luciferase will be available. Thus, light emission will be related to the activity of the gene [59]. This enables indirect imaging of gene activation, but of course requires targeted cells to be genetically engineered beforehand. Bioluminescence has the advantage of not having any background signal due to the lack of autoluminescence in the hosts. Thus, it can be used to detect light even from deep sources within the body.
- **Autosynthesis of fluorescent proteins**
  An alternative to the luciferase approach is the use of fluorescent proteins. Again, these have to be genetically engineered into the cell genome, but in

[¶]Enzymes are proteins, i.e., sequences of amino acids, that function as biochemical catalysts

contrast to bioluminescent system, no substrate like luciferin is required to induce light emission. Instead, as the name suggests, the created proteins can be excited with an external light source and will then exhibit fluorescence. A number of fluorescent proteins (FP) are available nowadays [86, 82]. FPs have, however, the disadvantage of being usually unstable and sometimes cytotoxic. Also, light used for excitation might also undesirably induce autofluorescence in observed tissues. The emission wavelength of these proteins have been engineered to reach deep into the important red part of the visible spectrum with emission wavelengths going beyond 650nm, having sufficient brightness and stability for in vivo tomographic imaging purposes, as demonstrated in [96].

# Chapter 2.

# Photon Propagation Models

> Truth is much too complicated to allow anything but approximations.
>
> *(John v. Neumann)*

THIS chapter contains, in compressed form, a complete derivation of the linear reconstruction model for FMT starting from the radiative transfer equation. The equations described herein are mainly state of the art in the field of biomedical optics. Obviously, the contents of this chapter have been published many times before; however, to the author's best knowledge, they are not available in this compiled form in a single publication.

There are as many mathematical notations used as there are authors publishing in the field. Herein, the notation for the radiative transfer equation was mainly taken from Anikonov [17], the diffusion approximation and its derivation is given according to Arridge [19], the derivation of the Born approach was inspired by Kak and Slaney [50], but changed to the diffusion model by the author.

## 2.1. The Radiative Transfer Equation

The standard model for photon propagation in turbid media is the *Radiative Transfer Equation* (RTE), which was originally developed in the 1940's to describe neutron transport in nuclear science [80]. It models the propagation of classical, non-interacting point particles through a connected open subset (*domain*) $\Omega \subset \mathbb{R}^3$. The propagating particles are absorbed and / or scattered during their passage through the domain. The exterior boundary of domain $\Omega$ will be denoted by $\partial\Omega$.

For photons, which are highly non-classical, the model is still generally accepted and experimentally well established [47, 51, 64, 76] albeit not completely accurate in all cases. In particular it does not suitably model phenomenons connected to the wave nature of photons, thus making it impossible to describe interference effects. In particular, the RTE is actually invalid for coherent light, which in turn is

often used for illumination in optical tomography due to the excellent monochromatic property of coherent laser light. Because of the many scattering events photons undergo in tissues, however, coherence is lost after a few scattering lengths [6].

The RTE, as given by Anikonov [17], describes the change in *photon radiance* $u(\mathbf{r},\mathbf{s},t)$ [Photons$\cdot$s$^{-1}$cm$^{-2}$sr$^{-1}$] at time $t$ and position $\mathbf{r}\in\Omega$. The change in radiance is modeled along propagation direction $\mathbf{s}\in S$, where $S$ is the unit sphere. The whole formula is given by*

$$\left[\tfrac{\partial}{v\partial t}+\mathbf{s}\cdot\nabla+\mu_a(\mathbf{r})+\mu_s(\mathbf{r})\right]u(\mathbf{r},\mathbf{s},t)=\mu_s(\mathbf{r})\int_S p(\mathbf{r},\mathbf{s},\mathbf{s}')\,u(\mathbf{r},\mathbf{s},t)\,d\mathbf{s}'+q(\mathbf{r},\mathbf{s},t). \quad (2.1)$$

In equation (2.1), $v$ is the speed of light in the medium, $\mu_a(\mathbf{r})$ [cm$^{-1}$] and $\mu_s(\mathbf{r})$ [cm$^{-1}$] are *attenuation* and *scattering coefficients*, respectively. The *scattering kernel* $p(\mathbf{r},\mathbf{s},\mathbf{s}')$ describes the spatially varying probability at $\mathbf{r}$ that a photon is scattered from direction $\mathbf{s}'$ into $\mathbf{s}$. As the scattering kernel $p$ describes a probability, it is normalized, i.e., $\forall\mathbf{s}\in S:\int_S p(\mathbf{r},\mathbf{s},\mathbf{s}')\,d\mathbf{s}'=1$. Any radiance created by internal sources is given by the *source function* $q(\mathbf{r},\mathbf{s})$. A visual interpretation of terms used in the formulation of the RTE can be found in figure 2.1.

Equation (2.1) is time-dependent and considers only a single energy or wavelength, i.e., only inelastic scattering events without change in wavelength are accounted for. However, these are the only scattering events present at low photon energies—fluorescence is usually not modeled as a scattering event, as described later in section 2.3.2. Furthermore, it is assumed that optical coefficient functions $\mu_a(\mathbf{r})$ and $\mu_s(\mathbf{r})$ are invariant of time, at least on the time scales considered for imaging.

The time-dependence of the photon radiance in equation (2.1) was not taken into account in experiments presented in later chapters. Instead, only time-integrating detectors and continuous sources were employed in measurement setups. Neglecting the time-dependence of radiance $u$ results in the time-independent version of the RTE:

$$\left[\mathbf{s}\cdot\nabla+\mu_a(\mathbf{r})+\mu_s(\mathbf{r})\right]u(\mathbf{r},\mathbf{s})=\mu_s(\mathbf{r})\int_S p(\mathbf{r},\mathbf{s},\mathbf{s}')\,u(\mathbf{r},\mathbf{s})\,d\mathbf{s}'+q(\mathbf{r},\mathbf{s}). \quad (2.2)$$

For both equations (2.1) and (2.2) it is necessary to define certain boundary conditions if only a domain $\Omega\subset\mathbb{R}^3$ is to be considered. Boundary conditions constrain the photons entering ($u^-$) or leaving ($u^+$) the domain through its exterior boundary $\partial\Omega$, i.e., constrain either

$$u^+=u(\mathbf{r},\mathbf{s})\Big|_{\substack{\mathbf{r}\in\partial\Omega,\ \mathbf{s}\in S\\ \mathbf{s}\cdot\mathbf{n}(\mathbf{r})>0}} \qquad \text{or} \qquad u^-=u(\mathbf{r},\mathbf{s})\Big|_{\substack{\mathbf{r}\in\partial\Omega,\ \mathbf{s}\in S\\ \mathbf{s}\cdot\mathbf{n}(\mathbf{r})<0}}$$

*The notation used is very close to the one employed by Anikonov [17]; some symbols have been changed only to better comply with the notational style used in this thesis. Often, the scattering kernel $p$ is chosen to only depend on scattering angle $\mathbf{s}\cdot\mathbf{s}'$, see Nieto-Vesperinas [63] or Ripoll [76]. However, for the cases considered in this thesis, these notations are equivalent.

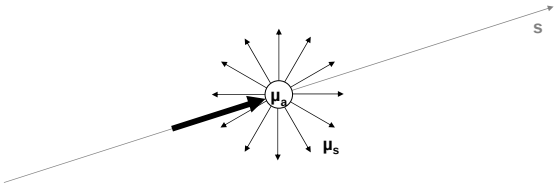


**(a)** Left hand side terms in the RTE

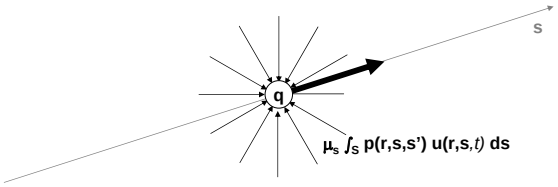


**(b)** Right hand side term in the RTE

**Figure 2.1:** Illustration of left and right hand side expressions of the RTE as given by equations (2.1) or (2.2). The RTE models the change in radiance $u$ at a point $r$ in direction $\mathbf{s}$, and—in case of the time-dependent equation—also in time $t$. The change is described by the differential operator $\left(\frac{\partial}{v\partial t} + \mathbf{s}\cdot\nabla\right)$. In the figures above, $\mathbf{s}$ is denoted by the long gray arrow, while an arbitrary $\mathbf{r}$ is depicted by the circle in the center. (a) On the left hand side of the equation, apart from the differential operator, all absorbing terms are given, i.e. photon absorption $\mu_a(\mathbf{r})$ and the total scattering $\mu_s(\mathbf{r})$ of photons scattering away from $\mathbf{s}$, as depicted by the many arrows. (b) On the right hand side, all source terms are given. These are $q(\mathbf{r},\mathbf{s},t)$, the source function, which creates new photons at $\mathbf{r}$ into direction $\mathbf{s}$, and the scattering integral $\mu_s \int_S p(\mathbf{r},\mathbf{s},\mathbf{s}')\,u(\mathbf{r},\mathbf{s},t)$. The latter expression is equal to the number of photons scattered into direction $\mathbf{s}$ from all other directions.

---

where $\mathbf{n}(\mathbf{r})$ is the outward pointing surface normal at $\mathbf{r} \in \partial\Omega$. Function $u^+$ is called *exitance*, and $u^-$ is called *incidence*. Due to different usage of the normal vector's direction, some authors define $u^+$ as incidence, and $u^-$ as exitance. Also, often the symbols $\Gamma^+$ and $\Gamma^-$ are used. For the RTE, either incidence or exitance may be constrained by boundary conditions, but not both simultaneously, to yield a solution.

For the purpose of optical tomography, the commonly employed boundary conditions define that photons leaving $\Omega$ will not re-enter the domain [19]. Thus, the boundary condition is given by $u^- = 0$. The incidence created by sources outside domain $\Omega$, the boundary condition can be changed to include the incident light, i.e. $u^- = q|_{\partial\Omega}$.

To simplify equations (2.1) and (2.2), often an analytical scattering kernel is used, most commonly the Henyey-Greenstein function [45]. This function was de-

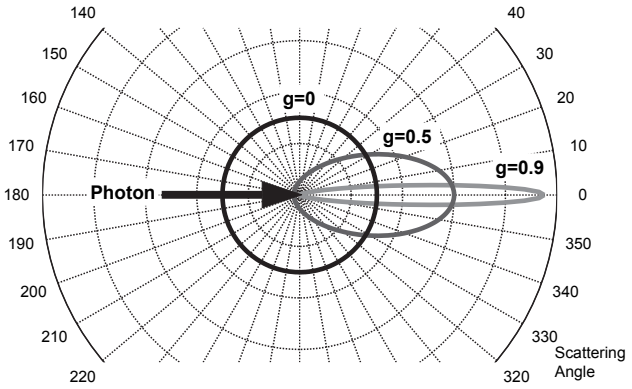


**Figure 2.2:** Visualization of the Henyey-Greenstein scattering kernel for different values of anisotropy $g$, from $g = 0$ (isotropic scattering) to $g = 0.9$ (strong forward scattering). The scattering kernel is normalized so that integration over the unit sphere evaluates to 1; however, for illustration purposes, functions have been scaled to fit in the plot. In reality the plots for $g > 0$ reach far out to the right.

veloped to model photon scattering in galactic dust clouds, but it has also successfully been applied to tissue optics [33]:

$$p_{\mathrm{hg}}(\mathbf{r},\mathbf{s},\mathbf{s}') = \frac{1-g^2}{4\pi\left(1-2g\mathbf{s}\cdot\mathbf{s}'+g^2\right)^{3/2}} \tag{2.3}$$

As can be seen from (2.3), the scattering probability in case of Henyey-Greenstein scattering does not depend on the absolute angles $\mathbf{s}$ and $\mathbf{s}'$, but only on the cosine of the angle $\theta$ between these two vectors, i.e., $\cos\theta = \mathbf{s}\cdot\mathbf{s}'$. Additionally, a parameter $g$ called the *anisotropy* is introduced, defined as the expectation value of $\cos\theta$, $g = \langle \mathbf{s}\cdot\mathbf{s}' \rangle \in [-1\cdots+1]$. The influence of anisotropy on the angular probability distribution (2.3) is illustrated in figure 2.2. A value of $g = 0$ is equal to completely isotropic scattering, a value of $g = 1$ means complete forward scattering, and $g = -1$ means complete backward scattering. For tissues a value of $g > 0.9$ is usually assumed. Although often used, it should be noted that the scattering probability in highly structured tissues (like muscle fibers or dentin, for example) might actually depend on the absolute directions and not just the scattering angle [52, 53], so that the scattering kernel (2.3) cannot be used in these cases.

## 2.2. The Diffusion Approximation

A common approximation to the RTE is the diffusion equation. It is obtained from the RTE using a spherical harmonics expansion of $u$ as given by [19],

$$u(\mathbf{r},\mathbf{s},t) = \sum_{l=0}^{\infty} \sum_{m=-l}^{l} u_{m,l}(\mathbf{r},t)\, Y_{m,l}(\mathbf{s}). \tag{2.4}$$

In equation (2.4), $Y_{m,l}$ are the spherical harmonics. Instead of radiance $u$ two derived quantities are then used in the equations, photon density $\Phi$ and photon current $J$, which are equal to the expressions in (2.4) for $l = 0$ and $l = 1$:

$$\Phi(\mathbf{r},t) = \int_S u(\mathbf{r},\mathbf{s},t)\, d\mathbf{s} \tag{2.5a}$$

$$J(\mathbf{r},t) = \int_S \mathbf{s} \cdot u(\mathbf{r},\mathbf{s},t)\, d\mathbf{s} \tag{2.5b}$$

Furthermore, scattering is considered to be non-zero and isotropic, i.e., $p = \frac{1}{4\pi}$. For anisotropic scattering with $g \neq 0$, the scattering coefficient is reduced to an equivalent of isotropic scattering, $\mu_s' = (1-g)\mu_s$, and still isotropy of scattering is assumed. Also, only isotropic sources $q(\mathbf{r},t)$ are allowed. Up to now, the approximations made can lead to the so-called $P_1$-approximation, which requires in fact a lengthy derivation as given by Arridge [19]. The $P_1$-approximation is given by the following two coupled equations for $\Phi$ and $J$:

$$\left(\frac{\partial}{v\partial t} + \mu_a(\mathbf{r})\right) \Phi(\mathbf{r},t) + \nabla \cdot J(\mathbf{r},t) = q(\mathbf{r},t) \tag{2.6a}$$

$$\left(\frac{\partial}{v\partial t} + \left(\mu_a(\mathbf{r}) + \mu_s'(\mathbf{r})\right)\right) J(\mathbf{r},t) + \tfrac{1}{3}\nabla\Phi(\mathbf{r},t) = 0 \tag{2.6b}$$

Assuming that $\frac{\partial}{\partial t} J = 0$, which is difficult to justify for time-dependent problems—but which on the other side is clearly valid for the time-independent equilibrium, where also $\frac{\partial}{\partial t}\Phi = 0$—, equation (2.6b) transforms to Fick's law of diffusion,

$$J(\mathbf{r},t) = -\frac{1}{3\left(\mu_a(\mathbf{r}) + \mu_s'(\mathbf{r})\right)} \nabla\Phi(\mathbf{r},t) = -D\nabla\Phi(\mathbf{r},t). \tag{2.7a}$$

In (2.7a), $D$ [cm] is called *diffusion length* or *diffusion coefficient*. As shown above, it is defined by $D = \frac{1}{3}(\mu_a + \mu_s')^{-1}$. The constant time derivative of $J$ is justified by $\mu_a \ll \mu_s'$ [19], which simply means that there is only little to no loss of photons, i.e., no damping of the system. If it is instead assumed that in first order $J(\mathbf{r},t) = J(\mathbf{r},0)e^{v\alpha t}$,

i.e., that the photon current is damped exponentially instead of remaining constant, the resulting equation becomes

$$J(\mathbf{r},t) = -\frac{1}{3(\mu_a+\mu_s'+\alpha)}\nabla\Phi(\mathbf{r},t), \tag{2.7b}$$

so that the definition of the diffusion coefficient changes. It is argued that $\alpha = \mu_a$ (see [19] and references therein), leading to $D = \frac{1}{3\mu_s'}$; or that $\alpha = \beta\mu_a$ for some constant $\beta$. As long as $\mu_a \ll \mu_s'$, however, $D = \frac{1}{3\mu_s'}$ is a good approximation in any case and will be used throughout this thesis. Either equation (2.7a) or (2.7b) can be used in (2.6a) to finally yield the diffusion equation,

$$\left[\frac{\partial}{v\partial t} - \nabla D(\mathbf{r})\nabla + \mu_a(\mathbf{r})\right]\Phi(\mathbf{r},t) = -q(\mathbf{r},t). \tag{2.8a}$$

For equation (2.8a) there also exists a time-independent version, which will exclusively be considered in this work:

$$\left[-\nabla D(\mathbf{r})\nabla + \mu_a(\mathbf{r})\right]\Phi(\mathbf{r}) = -q(\mathbf{r}) \tag{2.8b}$$

As mentioned in section 2.1, boundary conditions have to be considered. Within the diffusion equation there is no direct possibility to formulate a condition based on exitance or incidence. Instead, the total integral over the photon density leaving the boundary has to be calculated and used in a boundary condition [18, 42]. This integral has to take into account total internal reflection caused by the refractive index mismatch between diffuse medium and air. The resulting boundary condition is given in the form of a differential equation,

$$\Phi(\mathbf{r},t)|_{\partial\Omega} + 2AD(\mathbf{r})\mathbf{n}(\mathbf{r})\cdot\nabla\Phi(\mathbf{r},t)|_{\partial\Omega} = 0, \tag{2.9}$$

where $\mathbf{n}$ is the outward pointing surface normal at $\mathbf{r}$ and $A$ takes into account the refractive index mismatch at the boundary, i.e., the effects of total internal reflection. Different definitions of $A$ have been used in the literature [18]. The type of boundary condition given in (2.9) is called *Robin boundary condition*. For the case of the diffusion equation, it is also possible to use extend the size of the domain going outward from the real boundary and then use a zero boundary condition, i.e. $\Phi|_{\partial\Omega} = 0$ [18, 81].

## 2.3. Using the Diffusion Equation in Optical Tomography

In the following section, the diffusion equation (2.8b) will be reformulated to create an analytical reconstruction algorithm, the so-called *normalized Born approach*, used in subsequent chapters.

Reconstruction requires uniqueness of the inverse problem, i.e., that any given distribution of photon densities on the boundary $\partial\Omega$ can be created by only one possible distribution of optical parameters. It has been shown that the inverse problem of estimating $\mu_a$ and $D$ is unique for the time-dependent diffusion equation (2.8a), but that it is not for the time-independent case (2.8b) [19], although there are regularization algorithms available to minimize the parameter crosstalk [72]. The following derivations, on the other hand, simplify the problem by assuming $D$ to be constant. Reconstruction is only performed on $\mu_a$.

### 2.3.1. Born Approximation

Within the Born approximation, a constant homogeneous background $D^0$, $\mu_a^0$ of optical properties is assumed from which small perturbations $\delta D(\mathbf{r})$, $\delta\mu_a(\mathbf{r})$ exist. In the time-independent diffusion equation, due to the non-uniqueness of the inverse problem [19], diffusion length $D$ is assumed constant, i.e., $D = D^0$, and only a small perturbation of the absorption coefficient is allowed, i.e., $\mu_a(\mathbf{r}) = \mu_a^0 + \delta\mu_a(\mathbf{r})$. The perturbation $\delta\mu_a$ leads to a perturbation of the photon density $\Phi(\mathbf{r}) = \Phi^0(\mathbf{r}) + \delta\Phi(\mathbf{r})$, where $\Phi^0(\mathbf{r})$ is the solution to the homogeneous diffusion equation,

$$\left[-D^0\nabla^2 + \mu_a^0\right]\Phi^0(\mathbf{r}) = -q(\mathbf{r}). \tag{2.10}$$

Under these presumptions, the time-independent diffusion equation (2.8b) can be written as

$$\left[-D^0\nabla^2 + \mu_a^0 + \delta\mu_a(\mathbf{r})\right]\left[\Phi^0(\mathbf{r}) + \delta\Phi(\mathbf{r})\right] = -q(\mathbf{r}). \tag{2.11}$$

Combining (2.11) and (2.10) yields

$$\left[-D^0\nabla^2 + \mu_a^0\right]\delta\Phi(\mathbf{r}) = -\delta\mu_a(\mathbf{r})\left[\Phi^0(\mathbf{r}) + \delta\Phi(\mathbf{r})\right]. \tag{2.12}$$

As $\delta\mu_a$ is supposed to be small, it can be assumed in first order that the perturbation $\delta\Phi$ of the photon density is small, $\delta\Phi \ll \Phi^0$, therefore $\Phi \approx \Phi^0$. This leads to the first order Born approximation:

$$\left[-D^0\nabla^2 + \mu_a^0\right]\delta\Phi(\mathbf{r}) = -\delta\mu_a(\mathbf{r})\Phi^0(\mathbf{r}) \tag{2.13}$$

How does equation (2.13) enable reconstruction? Be reminded that the entity of interest for reconstruction is $\delta\mu_a(\mathbf{r})$; it is supposed that $\delta\Phi(\mathbf{r})$ can be measured at least on some points $\mathbf{r}_b \in \partial\Omega$ of the domain boundary, i.e., $\{\mathbf{r}_b\} \subset \partial\Omega$. To allow reconstruction, we make use of the so-called *homogeneous Green's function* $G(\mathbf{r}, \mathbf{r}_s)$, which is the solution to the equation

$$\left[-D^0\nabla^2 + \mu_a^0\right]G(\mathbf{r}, \mathbf{r}_s) = -\delta_0(\mathbf{r} - \mathbf{r}_s). \tag{2.14}$$

In equation (2.14), $\delta_0$ is Dirac's delta function. $G$ is called *homogeneous* as the coefficients of the differential operator are constants. If the Green's function is known, $\Phi^0$ of equation (2.13) can be rewritten as the convolution of source function $q$ and Green's function $G$,

$$\Phi^0(\mathbf{r}) = \int_{\mathbf{r}_S \in \Omega} G(\mathbf{r}, \mathbf{r}_s) q(\mathbf{r}_s) \, d\mathbf{r}_s. \tag{2.15}$$

Using (2.15) in (2.13) yields

$$\left[-D^0 \nabla^2 + \mu_a^0\right] \delta\Phi(\mathbf{r}) = \int_{\mathbf{r}_s \in \Omega} \delta\mu_a(\mathbf{r}) G(\mathbf{r}, \mathbf{r}_s) q(\mathbf{r}_s) \, d\mathbf{r}_s, \tag{2.16}$$

where $\delta\Phi$ can again be expressed in terms of the Green's function convoluted with the right hand side of (2.16)—analogously to equation (2.15)—, resulting in

$$\delta\Phi(\mathbf{r}) = \iint_{\substack{\mathbf{r}' \in \Omega \\ \mathbf{r}_s \in \Omega}} G(\mathbf{r}, \mathbf{r}') \delta\mu_a(\mathbf{r}') G(\mathbf{r}', \mathbf{r}_s) q(\mathbf{r}_s) \, d\mathbf{r}_s \, d\mathbf{r}'. \tag{2.17a}$$

In an experimental setting where a pencil beam of light is used as an external source incident on a point $\mathbf{r}_b$ of the exterior domain boundary $\partial\Omega$, this pencil beam can be modeled as a single point source at one diffusion length into the medium $\mathbf{r}_s = \mathbf{r}_b + D^0\mathbf{s}$, where $\mathbf{s}$ is the pencil beam's propagation direction inside the medium (i.e. after refraction at the exterior boundary). Source function $q(\mathbf{r})$ is then modeled as $q(\mathbf{r}) = \Theta_s \delta_0(\mathbf{r} - \mathbf{r}_s)$ [19, 81] with $\Theta_s$ being source power. Inserting this into (2.17a) simplifies the double integral and yields:

$$\delta\Phi(\mathbf{r}) = \Theta_s \int_{\mathbf{r}' \in \Omega} G(\mathbf{r}, \mathbf{r}') \delta\mu_a(\mathbf{r}') G(\mathbf{r}', \mathbf{r}_s) \, d\mathbf{r}' \tag{2.17b}$$

Of course, equation (2.17b) only leads to a simplification of the problem posed in (2.13) if $G$ is known or can be determined easily. For an infinite domain $\Omega = \mathbb{R}^3$, the Green's function evaluates to the exponential term

$$G^{\text{inf}}(\mathbf{r}_1, \mathbf{r}_2) = \frac{\exp\left(\sqrt{\frac{\mu_a^0}{D^0}} |\mathbf{r}_1 - \mathbf{r}2|\right)}{|\mathbf{r}_1 - \mathbf{r}2|}.$$

However, for finite domains boundary conditions need to be taken into account. On the calculation of Green's functions, please refer to section 2.4 below.

The first order Born approximation was obtained by assuming $\Phi = \Phi_0$, leading to equation (2.12) above. The $n$-th order approximations are obtained by letting $\Phi = \Phi_0 + \delta\Phi_{n-1}$ on the right hand side of equation (2.12), where $\delta\Phi_n$ is the $n$-th order approximation for $\delta\Phi$. The first order approximation $\delta\Phi_1$ evaluates to the expression given in equation (2.17b). See the book by Kak and Slaney [50] for more details.

For computational efficiency it is helpful to mention the reciprocity of the Green's function of the diffusion equation [19], i.e.,

$$G(\mathbf{r}, \mathbf{r}') = G(\mathbf{r}', \mathbf{r}). \tag{2.18}$$

The importance of this property for calculations will be shown later, in section 2.4.

### 2.3.2. Modeling of Fluorescence

As described in chapter 1.2.3, fluorescence is a complex process. A common approach for simplification is the approximation of fluorescence as a two state quantum process, assuming that a fluorophore can only be excited at a single wavelength $\lambda_x$—the *excitation wavelength*—and will only emit at a single wavelength $\lambda_m$—the *emission wavelength*. According to such a model, the presence of chromophores will increase the absorption exactly by $\varepsilon c(\mathbf{r})$, where $\varepsilon$ is the Molar extinction coefficient, and $c(\mathbf{r})$ is the chromophore concentration at $\mathbf{r}$. Thus, the propagation of light at the excitation wavelength will be governed by

$$\left[-\nabla D_x(\mathbf{r})\nabla + \mu_{ax}(\mathbf{r}) + \varepsilon c(\mathbf{r})\right]\Phi_x(\mathbf{r}) = -q_x(\mathbf{r}), \tag{2.19a}$$

with subscript $x$ indicating that the according function depends actually on wavelength, i.e. $D_x$ is the diffusion coefficient at $\lambda_x$.

The propagation of emitted light will also be governed by the diffusion equation, but the source function and the attenuation term will be different: as the fluorophore shall not absorb at the emission wavelength, and as external sources emitting at $\lambda_m$ shall not exist, the fluorophore will emit a fraction $\gamma$ (the quantum efficiency) of the absorbed light, i.e.,

$$\left[-\nabla D_m(\mathbf{r})\nabla + \mu_{am}(\mathbf{r})\right]\Phi_m(\mathbf{r}) = -\gamma\varepsilon c(\mathbf{r})\Phi_x(\mathbf{r}). \tag{2.19b}$$

Another often used though critical approximation consists in assuming no change in optical parameters due to the small difference between $\lambda_x$ and $\lambda_m$ (the Stokes shift), i.e. assuming $D_x = D_m = D$ and $\mu_{ax} = \mu_{am} = \mu_a$. Note that this assumption is only approximately valid for small Stokes shifts (for Cy5.5, for instance, it is around 20nm) but not for larger shifts as obtainable with quantum dot nanoparticles or two photon excitation.

However, if differences in optical properties can be neglected for the two wavelengths, and if scattering and absorption coefficients can be considered constants, equation (2.19b) turns into an equivalent of (2.13). The term $\varepsilon c$ then takes the role of the perturbation in absorption, i.e. $\varepsilon c(\mathbf{r}) \equiv \delta\mu_a(\mathbf{r})$, and photon density $\gamma^{-1}\Phi_m$, which is the photon density created by fluorescence and normalized by quantum yield, becomes equivalent to the perturbed photon density, $\gamma^{-1}\Phi_m(\mathbf{r}) \equiv \delta\Phi(\mathbf{r})$, which gives for an excitation point source of power $\Theta_s$ located at $\mathbf{r}_s$:

$$\left[-D^0\nabla^2 + \mu_a^0\right]\tfrac{1}{\gamma}\Phi_m(\mathbf{r}) = \Theta_s \int\limits_{\mathbf{r}_s\in\Omega} \varepsilon c(\mathbf{r})G(\mathbf{r},\mathbf{r}_s)\,d\mathbf{r}_s \tag{2.20}$$

As photon densities from fluorescence are several orders of magnitude smaller than the densities caused by the excitation light source, in a further approximation it is assumed that the excitation photon density is approximately equal to the homogeneous solution of the diffusion equation, $\Phi_x \approx \Phi^0$, and thus $\Phi_x(\mathbf{r}) \approx \Theta_s G(\mathbf{r},\mathbf{r}_s)$.

The ratio of photon flux $\Phi_m$ at the emission wavelength $\lambda_m$ of a fluorochrome and the photon flux $\Phi_x$ at the excitation wavelength $\lambda_x$, both created by a point source at $\mathbf{r}_s \in \Omega$ and detected at position $\mathbf{r}_d \in \Omega$ is then given by [70]:

$$\frac{\Phi_m(\mathbf{r}_d)}{\Phi_x(\mathbf{r}_d)} = \int_\Omega \frac{G(\mathbf{r},\mathbf{r}_m)\gamma\varepsilon c(\mathbf{r}_m)G(\mathbf{r}_m,\mathbf{r}_s)}{G(\mathbf{r},\mathbf{r}_s)}\,d\mathbf{r}_m \tag{2.21}$$

where $G(\mathbf{r}_1,\mathbf{r}_2)$ denotes the Green function at $\mathbf{r}_1$ inside the diffuse domain due to a point source at $\mathbf{r}_2$, while $\gamma\varepsilon c(\mathbf{r}_m)$ is the unknown attenuation $\varepsilon c$ caused by the fluorochromes and multiplied with the quantum efficiency $\gamma$. The integral is defined within the whole volume $\Omega$ considered for reconstruction. Here, "detection" is defined as a direct measurement of photon densities $\Phi_x$ and $\Phi_m$ inside the domain $\Omega$. Equation (2.21) will be modified in chapter 3 to support actual detector measurements, i.e., measurements using optical fiber detectors or a CCD camera.

### 2.3.3. Combined Fluorescence and Absorption Modeling

Under the assumption of a constant and known quantum yield and similar optical properties for both emission and excitation wavelength, equations (2.19a) and (2.19b) can be combined into a new, decoupled system of equations, namely by rewriting (2.19a) as

$$\left[-\nabla D(\mathbf{r})\nabla + \mu_a(\mathbf{r})\right]\Phi_x(\mathbf{r}) + q(\mathbf{r}) = -\varepsilon c(\mathbf{r})\Phi_x(\mathbf{r}). \tag{2.22}$$

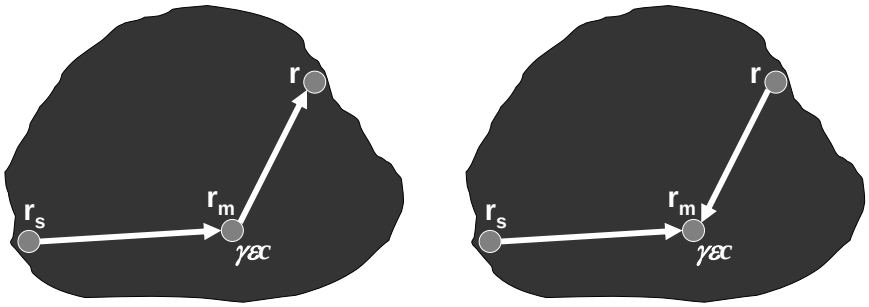


**(a)** Original problem

**(b)** Adjoint fluorescence excitation

**Figure 2.3:** This figure depicts the meaning of the integrals in equations (2.17b) or (2.21). Starting from a source point $\mathbf{r}_s$, the excitation light diffuses through the domain $\Omega$ shown as a black shape in the drawing. When it reaches $\mathbf{r}'$, it will possibly excite a fluorophore there, leading to an emission that is proportional to the amount of excitation light times $\gamma\varepsilon c$. This emitted light will then diffuse further through the domain and eventually be detected at $\mathbf{r}$. Part (b) illustrates the use of the adjoint Green's function for emitted light; due to the reciprocity relation (2.18), (a) and (b) are equal.

As the right hand side of equation (2.22) is equal to the right hand side of (2.19b), it can be inserted there, yielding the following set of uncoupled equations:

$$\left[-\nabla D(\mathbf{r})\nabla + \mu_a(\mathbf{r}) + \varepsilon c(\mathbf{r})\right]\Phi_x(\mathbf{r}) = -q(\mathbf{r}) \tag{2.23a}$$

$$\left[-\nabla D(\mathbf{r})\nabla + \mu_a(\mathbf{r})\right] \underbrace{\left(\Phi_x(\mathbf{r}) - \tfrac{1}{\gamma}\Phi_m(\mathbf{r})\right)}_{=\Phi_t(\mathbf{r})} = -q(\mathbf{r}) \tag{2.23b}$$

The uncoupled system of equations (2.23a) and (2.23b) was first proposed by the author of this thesis [12]. An advantage in comparison to the coupled system of equations (2.19a) and (2.19b) is given by the ability to simultaneously perform reconstructions of the attenuation coefficient with each of the two equations, and consecutively subtract the resulting distribution of attenuation values from each other. Reconstructions could be performed with any algorithm including the Born reconstruction without normalization. Necessary measurements of the new mixed photon density $\Phi_t$ can easily be derived, because $\Phi_t$ is only a linear combination of excitation and emission densities.

Possibly, this provides a better way of normalization than the normalized Born approach given in equation (2.21), as the normalization in the latter equation is used only for calibration of detector sensitivities and source intensities. However, in case of heterogeneous media, i.e., in the presence of absorbers, reconstruction algorithms based on fluorescence intensities alone will not be able to give quantitatively correct results [69]. With the system of equations as given above, on the other

hand, both absorption and emission coefficients will be computed simultaneously. Unfortunately, the behavior of the system of equations (2.23a) / (2.23b) did not yet undergo thorough investigation.

### 2.3.4. Linearized Model

Equation (2.17b) can be approximated by a linear system if the domain $\Omega$ is partitioned into a set of $v$ disjoint voxels of Volume $\Delta V_i$ each having its center at $\mathbf{r}'_i$ completely covering the domain $\Omega$:

$$\delta\Phi(\mathbf{r}_d) = \sum_i \underbrace{\Theta_s G(\mathbf{r}_d, \mathbf{r}'_i) G(\mathbf{r}'_i, \mathbf{r}_s) \Delta V_i}_{=w_{s,d,i}} \delta\mu_a(\mathbf{r}'_i) \tag{2.24}$$

For $n$ different source positions $\mathbf{r}_{s,1\ldots n}$, and $m$ different locations $\mathbf{r}_{d,1\ldots m}$ from which measurements are acquired per source position, equation (2.24) can be written as a linear system of the following structure:

$$\begin{pmatrix} \begin{pmatrix} \delta\Phi_{1,1} \\ \vdots \\ \delta\Phi_{1,m} \end{pmatrix} \\ \begin{pmatrix} \delta\Phi_{2,1} \\ \vdots \\ \delta\Phi_{2,m} \end{pmatrix} \\ \vdots \\ \begin{pmatrix} \delta\Phi_{n,1} \\ \vdots \\ \delta\Phi_{n,m} \end{pmatrix} \end{pmatrix} = \begin{pmatrix} \begin{pmatrix} w_{1,1,1} & \ldots & w_{1,1,v} \\ \vdots & \ddots & \vdots \\ w_{1,m,1} & \ldots & w_{1,m,v} \end{pmatrix} \\ \begin{pmatrix} w_{2,1,1} & \ldots & w_{2,1,v} \\ \vdots & \ddots & \vdots \\ w_{2,m,1} & \ldots & w_{2,m,v} \end{pmatrix} \\ \vdots \\ \begin{pmatrix} w_{n,1,1} & \ldots & w_{n,1,v} \\ \vdots & \ddots & \vdots \\ w_{n,m,1} & \ldots & w_{n,m,v} \end{pmatrix} \end{pmatrix} \begin{pmatrix} \delta\mu_{a,1} \\ \vdots \\ \delta\mu_{a,i} \\ \vdots \\ \delta\mu_{a,v} \end{pmatrix} \tag{2.25}$$

where $\delta\tilde{\Phi}_{k,j}$ is the photon density at $\mathbf{r}_{d,j}$ due to a point source at $\mathbf{r}_{s,k}$, $w_{k,j,i}$ is the *weight* of voxel $i$ with respect to source-detector combination $(k, j)$, and $\delta\mu_{a,i}$ is the average attenuation coefficient for voxel $i$. In short, equation (2.25) is denoted by $\boldsymbol{\delta\Phi} = \mathbf{W}\boldsymbol{\delta\mu_a}$ with $\boldsymbol{\delta\Phi}$ being the vector of measurements, $\mathbf{W}$ being the *weight matrix*, and $\boldsymbol{\delta\mu_a}$ denoting the vector of attenuation changes for all voxels considered. Reconstruction of these changes—which are the unknowns—can now be formulated as

$$\boldsymbol{\delta\mu_a} = \mathbf{W}^{-1}\boldsymbol{\delta\Phi}. \tag{2.26}$$

As $\mathbf{W}$ is not quadratic but rectangular with dimensions $mn \times v$, $\mathbf{W}^{-1}$ denotes a suitable pseudo inverse of $\mathbf{W}$ with $\mathbf{W}^{-1}\mathbf{W}^{\mathrm{T}} = \mathbf{Id}$. The weight matrix $\mathbf{W}$ is fully populated;

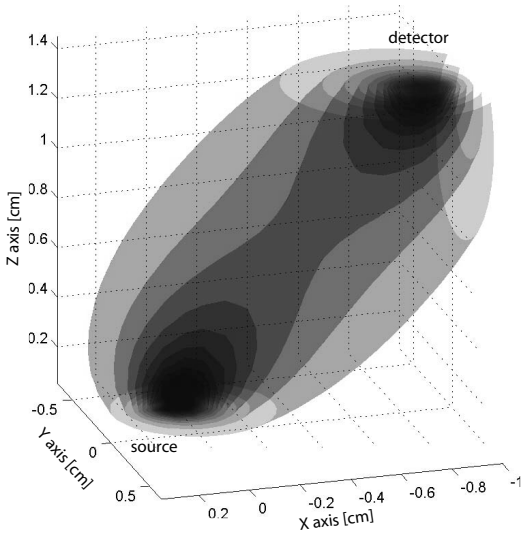


**Figure 2.4:** 3D-Visualization of the weight function for an arbitrary source-detector pair

however, most of the entries contain very low values. This is illustrated in figure 2.4, where for a source-detector pair the weights' amplitudes within the unknown volume are depicted by ten equidistant isosurfaces. The source / detector symmetry of the Green's function, see (2.18), is clearly depicted. Also it can be seen that at positions far away from source and detector, weights rapidly decay.

The weight function, as shown in figure 2.4, models the sensitivity of the given source / detector combination with respect to a perturbation in the absorption (for example due to a fluorophore) spatially resolved for all voxel positions.

### 2.3.5. Algebraic Reconstruction Technique (ART)

Within this thesis, weight matrix inversion was performed using the so-called Algebraic Reconstruction Technique (ART) with randomized row selection (r-ART) [5, 50]. While there are many matrix inversion techniques available, ART was chosen due to its simplicity, and comparability to results published earlier [4, 5, 70]. The algorithm will be shortly derived herein to facilitate understanding of the reconstruction method.

Each line $\delta\Phi_{i,j} = \sum_{k=1}^{v} w_{i,j,k}\delta\mu_{a,k}$ of the linear system (2.25) describes a hyperplane in $v$-dimensional space on which the solution for $\boldsymbol{\delta\mu_a}$ lies. In ART, $\boldsymbol{\delta\mu_a}$

is iteratively projected onto the hyperplanes described by the rows $i$ of the linear system as given by hyperplane normal $\mathbf{w} = (w_{i,j,\cdot})$ and offset $\delta\Phi_{i,j}$ as

$$\mathbf{w} \cdot \boldsymbol{\delta\mu_a} - \delta\Phi_{i,j} = 0. \tag{2.27}$$

Usually, an orthogonal projection (i.e. along the surface normal) is performed, i.e.

$$\boldsymbol{\delta\mu_a}' = \boldsymbol{\delta\mu_a} - \mathbf{w} \cdot \varrho \frac{\mathbf{w} \cdot \boldsymbol{\delta\mu_a} - \delta\Phi_{i,j}}{\|\mathbf{w}\|^2}, \tag{2.28}$$

where the *relaxation parameter* $\varrho \in \mathbb{R}^+$ determines whether the resulting vector $\boldsymbol{\delta\mu_a}'$ should lie on the plane ($\varrho = 1$), whether the projection should go beyond the plane ($\varrho > 1$) which is used in the systematic symmetric over-relaxation method of matrix preconditioning (SSOR-preconditioning), or whether the projection should only go a bit in the direction of the plane ($\varrho < 1$), as performed in this thesis. The latter method is used whenever inconsistencies (due to measurement errors etc.) are supposed to be contained in the matrix.

A single iteration of the ART-method involves performing projection (2.28) once for every single row of the matrix. In the randomized row access ART-method (r-ART), the order in which rows are accessed is randomly determined prior to every single iteration. This is done to optimize convergence [48].

## 2.4. Numerical Calculation of Green's Functions

Due to the complexity of boundary conditions in the case of complex shaped domains, analytical solutions for the Green functions of the diffusion equation are usually not available. Thus, they have to be determined using appropriate numerical methods.

### 2.4.1. Finite Element Method

The Finite Element Method (FEM) provides a means of solving arbitrary linear partial differential equations (PDE) numerically, i.e., a way of finding a solution function $\Phi$ that satisfies the PDE under given boundary or initial conditions. The problem of determining $\Phi$ is called *forward problem*, and $\Phi$ is sometimes also called *forward solution*.

The PDE consists of a differential operator $\mathscr{L}$, an unknown solution function $\Phi(\mathbf{r}), \mathbf{r} \in \mathbb{R}^d$, where $d$ is the dimension of the domain $\Omega \in \mathbb{R}^d$ in which the problem is defined, and a right hand side $q(\mathbf{r})$:

$$\mathscr{L}\{\Phi(\mathbf{r})\} = q(\mathbf{r}) \tag{2.29}$$

To simplify the problem of determining an appropriate forward solution $\Phi$, the function is to be approximated by a finite linear combination of $N$ given base functions $\varphi(\mathbf{r})$ with constant coefficients $\Phi_i \in \mathbb{R}$, also called *degrees of freedom*,

$$\Phi(\mathbf{r}) = \sum_{i=0}^{N} \Phi_i \varphi_i(\mathbf{r}). \tag{2.30}$$

Due to the linear behavior of the differential operator $\mathscr{L}$, applying operator $\mathscr{L}$ to the linear combination yields:

$$\mathscr{L}\left\{\sum_{i=0}^{N} \Phi_i \varphi_i(\mathbf{r})\right\} = \sum_{i=0}^{N} c_i \left[\mathscr{L}\{\varphi_i(\mathbf{r})\}\right] \tag{2.31}$$

Thus, the differential operator $\mathscr{L}$ is only applied to the given base functions, which are known. Therefore, to find the best approximation of the function, we have to find a set of coefficients $\Phi_i$ that minimize the residual of the PDE, i.e.:

$$\sum_{i=0}^{N} \Phi_i \left[\mathscr{L}\{\varphi_i(\mathbf{r})\}\right] - q(\mathbf{r}) \rightarrow \min! \tag{2.32}$$

The base functions $\varphi_i$ span a *Banach space*, i.e. a complete vector space with a scalar product and a norm. The scalar product of two functions $a(\mathbf{r})$, $b(\mathbf{r})$, $\mathbf{r} \in \Omega$ is defined by:

$$(a,b)_\Omega = \int_\Omega a(\mathbf{r})\, b(\mathbf{r})\, d\mathbf{r} \tag{2.33a}$$

We will also use a scalar product on the domain boundary $\partial\Omega$, i.e. for $\mathbf{r} \in \partial\Omega$:

$$(a,b)_{\partial\Omega} = \int_{\partial\Omega} a(\mathbf{r})\, b(\mathbf{r})\, d\mathbf{r} \tag{2.33b}$$

Connected to these two definitions of the scalar product are the norms

$$\|a\|_\Omega^2 = (a,a)_\Omega = \int_\Omega \big(a(\mathbf{r})\big)^2 d\mathbf{r}, \qquad \|a\|_{\partial\Omega}^2 = (a,a)_{\partial\Omega} = \int_{\partial\Omega} \big(a(\mathbf{r})\big)^2 d\mathbf{r}. \tag{2.34}$$

When using the—usually not orthogonal—vector base $\{\varphi_i\}$ the global minimum of equation (2.32) is defined as a solution where any change in the coefficients $\alpha_i$ would increase the residual. Thus, the residual projected into base function space should be zero:

$$\forall_i \sum_{i=0}^{N} \Phi_i \big(\varphi_i, \mathscr{L}(\varphi_j)\big)_\Omega = -(\varphi_i, q)_\Omega \tag{2.35}$$

This is known as Galerkin formulation of the problem. Equation (2.35) describes a linear system of equations that can be written $\mathbf{M\Phi} = \mathbf{q}$ where vector $\mathbf{\Phi}$ consists of the unknown coefficients $(\Phi_j)$ while the matrix $\mathbf{M} = (m_{ij})$ contains the expressions $m_{ij} = (\varphi_i, \mathscr{L}(\varphi_j))_\Omega$ that only depend on test functions $\varphi$; $\mathbf{q} = (q_i)$ is the vector containing the source function's projection into test function space, i.e. the expressions $q_i = (\varphi_i, q)_\Omega$.

For an appropriate choice of functions $\varphi$, the matrix is sparse and the equation can be inverted quickly, resulting in a solution for $\mathbf{\Phi}$, and thus for $\Phi$. Commonly, in a finite element approach the domain $\Omega$ is tessellated into tetrahedral or hexahedral "elements". Within these elements, only a small number of base functions $\varphi_i$ are nonzero, so that $(\varphi_i, \varphi_j)_\Omega$ is nonzero only for a small number of indices $j$, thus making $\mathbf{M}$ sparse.

In applications of the method presented in this thesis, bilinear interpolation functions $\varphi_i(\mathbf{r})$ are chosen, with the properties $\varphi_i(\mathbf{r}) \in [0 \ldots 1]$ and $\sum_i \varphi_i(\mathbf{r}) = 1$ for all $\mathbf{r} \in \Omega$, and additionally $\forall i \exists \mathbf{r}_i \in \Omega : \varphi_i(\mathbf{r}) = 1$, and $\varphi_i(\mathbf{r}_i) = \varphi_i(\mathbf{r}) = 1 \Rightarrow \mathbf{r} = \mathbf{r}_i$ where $\mathbf{r}_i$ is called the *support point* of $\varphi_i$. For the diffusion problem, where $\mathbf{M}$ is symmetric and positive definite, matrix inversion was carried out using a conjugate gradient method.

## 2.4.2. Finite Element Solution of the Diffusion Equation

A finite element system for the time independent diffusion equation (2.8b) can be obtained by using the Galerkin approach:

$$\forall \varphi_i : (\varphi_i, -\nabla D \nabla \Phi)_\Omega + (\varphi_i, \mu_a \Phi)_\Omega = -(\varphi_i, q)_\Omega \tag{2.36}$$

The diffusion term containing the second derivative $-\nabla D \nabla \Phi$ can be simplified using Green's theorem [81]:

$$(\varphi_i, -\nabla D \nabla \Phi)_\Omega = (\nabla \varphi_i, D \nabla \Phi)_\Omega + (\varphi_i, \mathbf{n} \cdot \nabla \Phi)_{\partial\Omega} \tag{2.37}$$

For the boundary term in equation (2.37), $\mathbf{n}$ is the outward pointing surface normal. Inserting into (2.36) results in the so-called weak form of the problem [81]:

$$\forall \varphi_i : (\nabla \varphi_i, D(\mathbf{r}) \nabla \Phi)_\Omega + (\varphi_i, \mu_a \Phi)_\Omega - (\nabla \varphi_i, D\mathbf{n} \cdot \nabla \Phi)_{\partial\Omega} = -(\varphi_i, q)_\Omega \tag{2.38}$$

The boundary term $(\varphi_i, D\mathbf{n} \cdot \nabla \Phi)_{\partial\Omega}$ is replaced by an equivalent for the respective boundary condition. Using a Dirichlet boundary condition, the integral evaluates to zero on the constrained boundaries, while for the Robin boundary condition (2.9), it evaluates to

$$(\nabla \varphi_i, D\mathbf{n} \cdot \nabla \Phi)_{\partial\Omega} = -\frac{1}{2AD} \Phi. \tag{2.39}$$

# Chapter 3.

# Detection Operator Notation

Numero pondere et mensura
Deus omnia condidit.*

*(Isaac Newton)*

## 3.1. Introduction

RECONSTRUCTION in the sense of the time-dependent or -independent diffusion equation (2.8a) or (2.8b), respectively, refers to the estimation of coefficient functions $D(\mathbf{r})$ and $\mu_a(\mathbf{r})$ in the differential operator $[-\nabla D\nabla + \mu_a]$. As described previously, the equation is defined within an open subset $\Omega \subset \mathbb{R}^3$ using appropriate boundary conditions on the outer boundary $\partial\Omega$. Coefficient functions are estimated based on a number of physical measurements $\widetilde{\Phi}(\mathbf{d})$ of the photon density $\Phi(\mathbf{r})$ obtained from a number of detectors $\mathbf{d} \in \mathbb{D}$. The set $\mathbb{D}$ will be called *detector space*. For a number of discrete measurements, $\mathbb{D} \subset \mathbb{N}$, or more specifically, $\mathbf{d} \in \mathbb{D} = \{1, \ldots, n\}$ for $n$ measurements. Images as obtained by a camera will later on be described using $\mathbb{D} \subset \mathbb{R}^2$ with $\mathbf{d} \in \mathbb{D}$ denoting the (continuous) coordinate on the acquired image.

Measurements are obtained using detectors physically located either (1) on the imaged object's boundary as represented by $\partial\Omega$, (2) inside the object as represented by $\Omega$ (for invasive measurements), or (3) somewhere outside the object in "free", i.e., non-diffusive, space $\mathbb{R}^3\backslash\Omega$. The latter is the case for camera-based non-contact imaging where the object is imaged through an objective lens. Detection can be described by an operator $\mathcal{P} : \Phi \mapsto \widehat{\Phi}$ mapping the photon density function $\Phi : \Omega \to \mathbb{R}$, as predicted by the diffusion equation, to the *predicted measurement* $\widehat{\Phi} : \mathbb{D} \to \mathbb{R}$. Predicted measurements $\widehat{\Phi}$ have to be distinguished from the experimental realization $\widetilde{\Phi}$. The vector space spanned by functions $\widehat{\Phi} : \mathbb{D} \to \mathbb{R}$ will be

* "God created everything by number, weight, and measure."

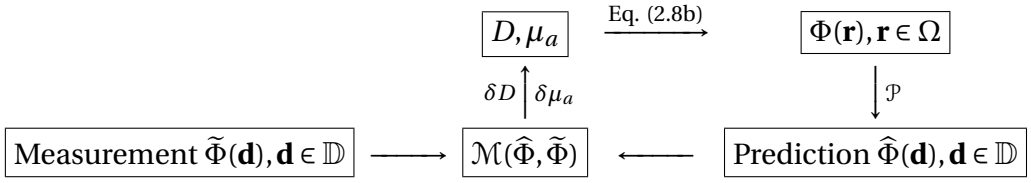


**Figure 3.1:** General layout of an iterative model-based reconstruction algorithm using detection operators

called *measurement space* and denoted by $\mathbb{M}$. A scalar product $(a,b)_{\mathbb{M}}$ and associated norm $\|a\|^2_{\mathbb{M}} = (a,a)_{\mathbb{M}}$ will be defined on the vector space $\mathbb{M}$ as either

$$(a,b)_{\mathbb{M}} = \sum_{i=1}^{n} a_i b_i \tag{3.1a}$$

for discrete measurement spaces where $\mathbb{D} = \{1,\ldots,n\}$, or

$$(a,b)_{\mathbb{M}} = \int_{\mathbb{D}} a(\mathbf{d})\, b(\mathbf{d})\; d\mathbf{d}. \tag{3.1b}$$

Let $\mathcal{M}$ be a functional measuring the deviation between an experimental measurement $\widetilde{\Phi}$ and the prediction $\widehat{\Phi} = \mathcal{P}\{\Phi\}$ which depends on $D$ and $\mu_a$. $\mathcal{M}$ is equivalent to the *measurement functional* as used for example by Bangerth [20] where $\mathcal{M}(\widehat{\Phi}, \widetilde{\Phi})$ is introduced as either $\mathcal{M} = \frac{1}{2}\|\widehat{\Phi} - \widetilde{\Phi}\|^2_{\mathbb{M}}$ or $\mathcal{M} = \frac{1}{2}\|\nabla\widehat{\Phi} - \nabla\widetilde{\Phi}\|^2_{\mathbb{M}}$. Using detector operator notation, the reconstruction process can then be formulated as a minimization problem:

$$\text{Find } D,\ \mu_a \text{ such that } \mathcal{M}\big(\widehat{\Phi}, \widetilde{\Phi}\big) \longrightarrow \min! \tag{3.2}$$

The general layout of an iterative reconstruction algorithm based on $\mathcal{M}$ and $\mathcal{P}$ is shown in figure 3.1. For the iteration depicted on the right hand side of figure 3.1, it is necessary to extract search directions $\delta D$ and $\delta\mu_a$ from $\mathcal{M}$. For gradient based minimizers, search directions should be calculated from the gradients of $\mathcal{M}$ with respect to $D$ and $\mu_a$, respectively. How gradients can be defined on the measurement functional and detection operator is shown in section 3.1.2.

The concept of measurement operators and a number of examples have been discussed previously by Arridge [19]. In this chapter, however, some specialized operators are introduced that were used to model detection with fiber optics detectors and CCD-cameras and will be used in subsequent chapters. The type of linear detection operator introduced here can be introduced in the normalized Born formulation presented in chapter 2.3.1. This modified Born approach will then be used in chapter 4 to compare the quality of reconstructed image data with respect to the detection operator employed.

### 3.1.1. Properties of the Detection Operator

Throughout this work, only *linear detection operators* will be considered, having the properties

$$\begin{aligned}\mathcal{P}\{\Phi_1(\mathbf{r})+\Phi_2(\mathbf{r})\} &= \mathcal{P}\{\Phi_1(\mathbf{r})\}+\mathcal{P}\{\Phi_2(\mathbf{r})\}, \text{ and}\\ \mathcal{P}\{a\Phi(\mathbf{r})\} &= a\mathcal{P}\{\Phi(\mathbf{r})\} \text{ for all scalars or functions } a \text{ invariant of } \mathbf{r}.\end{aligned}$$

Due to the linearity properties, and because the projection operators as defined herein operate on function vector spaces, $\mathcal{P}$ can generally be written as an integral operator of the form

$$\widehat{\Phi}(\mathbf{d}) = \mathcal{P}_{\Omega\to\mathbb{D}}\big\{\Phi(\mathbf{r})\big\}(\mathbf{d}) = \int\limits_{\mathbf{r}\in\Omega} \Phi(\mathbf{r})\Gamma(\mathbf{r},\mathbf{d})\; d\mathbf{r}, \tag{3.3}$$

where $\Gamma$ is a weighting function describing the sensitivity of a detector $\mathbf{d}\in\mathbb{D}$ with respect to a point $\mathbf{r}\in\Omega$. If $\Phi(\mathbf{r})$ is written as a linear combination of base functions as before, i.e., $\Phi(\mathbf{r}) = \sum_i \Phi_i\varphi_i(\mathbf{r})$,then, due to the linearity of $\mathcal{P}$,

$$\mathcal{P}\big\{\Phi(\mathbf{r})\big\} = \sum_i \Phi_i \mathcal{P}\big\{\varphi_i(\mathbf{r})\big\}. \tag{3.4}$$

For a finite number of measurements, i.e., if $\mathbb{D} = \{\mathbf{d}_1,\ldots,\mathbf{d}_n\}$, then $\mathcal{P}$ can be denoted in form of a $n\times m$ matrix $\mathbf{P}$. This matrix is applied according to $\widehat{\mathbf{\Phi}} = \mathbf{P}\mathbf{\Phi}$, where $\widehat{\mathbf{\Phi}} = (\widehat{\Phi}_1,\ldots,\widehat{\Phi}_n)$ is the vector of measurement predictions and $\mathbf{\Phi} = (\Phi_1,\ldots,\Phi_m)$ is the vector of coefficients. The detection matrix generally is of the following form:

$$\mathbf{P} = \begin{pmatrix} p_{1,1} & \cdots & p_{1,m}\\ \vdots & \ddots & \vdots\\ p_{n,1} & \cdots & p_{n,m}\end{pmatrix} = \begin{pmatrix} \mathcal{P}\{\varphi_1\}(\mathbf{d}_1) & \mathcal{P}\{\varphi_2\}(\mathbf{d}_1) & \ldots & \mathcal{P}\{\varphi_m\}(\mathbf{d}_1)\\ \mathcal{P}\{\varphi_1\}(\mathbf{d}_2) & \ddots & & \mathcal{P}\{\varphi_m\}(\mathbf{d}_2)\\ \vdots & & \ddots & \vdots\\ \mathcal{P}\{\varphi_1\}(\mathbf{d}_n) & \ldots\ldots\ldots\ldots & & \mathcal{P}\{\varphi_m\}(\mathbf{d}_n)\end{pmatrix} \tag{3.5}$$

### 3.1.2. Frechét Derivative

For gradient based reconstruction techniques, derivatives of the measurement error $\mathcal{M}(\widehat{\Phi},\widetilde{\Phi})$ with respect to changes in the optical coefficients $D$ and $\mu_a$ need to be evaluated. For finite element systems, often the so-called Fréchet derivatives are used which are the equivalent of a directional derivative in functional analysis. The Fréchet derivative $\nabla_{x;\xi}F$ of a functional $F$ is defined as:

$$\nabla_{x;\xi}F\big(x(\mathbf{r})\big) = \lim_{h\to 0}\frac{F\big(x(\mathbf{r})+h\xi(\mathbf{r})\big)-F\big(x(\mathbf{r})\big)}{h}, \tag{3.6}$$

and if it exists, $F$ is called *Fréchet-differentiable*. The Fréchet derivative is a directional derivative of $F(x(\mathbf{r}))$ along the direction of function $\xi(\mathbf{r})$. Let $x$ be described by a linear combination of base functions $\xi_i$, i.e., $x(\mathbf{r}) = \sum_i x_i \xi_i(\mathbf{r})$. In this case it is reasonable to restrict the search direction $\xi$ of the directional derivative to base functions $\xi_i$. Then the derivative $\nabla_{x;\xi_i} F$ describes the relation between a change of finite element coefficient $x_i$ and the resulting change of $F$.

With respect to the detection operator, it must be determined how a change in one of the optical parameters $\mu_a$ or $D$ relates to a change in the predicted measurements $\widehat{\Phi}$. This derivative cannot be calculated directly but via the chain rule. Using certain assumptions, a change in optical parameters can be related to a change in photon density, i.e., $\nabla_D \Phi$ and $\nabla_{\mu_a} \Phi$ are available. If furthermore $\nabla_\Phi \mathcal{M}$ can be determined, then $\nabla_{D/\mu_a} \mathcal{M} = \nabla_\Phi \mathcal{M} \circ \nabla_{D/\mu_a} \Phi$ according to the chain rule. Using the chain rule for $\mathcal{M}$ also allows to express $\nabla_\Phi \mathcal{M}$ as:

$$\nabla_{\Phi;\varphi} \mathcal{M}\big(\widetilde{\Phi}, \mathcal{P}\{\Phi\}\big) = \big[\nabla_{\widehat{\Phi};\xi} m(\widehat{\Phi}, \widetilde{\Phi})\big] \circ \big[\nabla_{\Phi;\varphi} \mathcal{P}\{\Phi\}\big] \tag{3.7}$$

For a standard least-square minimization, where $\mathcal{M} = \frac{1}{2}\|\widehat{\Phi} - \widetilde{\Phi}\|^2_{\mathbb{M}}$, the derivative results in $\nabla_{\widehat{\Phi};\xi} \mathcal{M} = \big(\widehat{\Phi} - \widetilde{\Phi}, \xi\big)_{\mathbb{M}}$. For a discrete number of detected values $\widetilde{\Phi}_i$, the scalar product on $\mathbb{M}$ turns into $\sum_i \xi(\widehat{\Phi}_i - \widetilde{\Phi}_i)$, equation (3.1). The derivative $\nabla_\Phi \mathcal{P}$ of (3.7) can in turn be calculated directly as

$$\nabla_{\Phi;\varphi} \mathcal{P}\{\Phi\} = \lim_{h \to 0} \frac{\mathcal{P}\big\{\Phi(\mathbf{r}) + h\varphi(\mathbf{r})\big\} - \mathcal{P}\big\{\Phi(\mathbf{r})\big\}}{h} = \mathcal{P}\big\{\varphi(\mathbf{r})\big\}, \tag{3.8}$$

due to the linearity of the operator. Thus, the derivative $\nabla_\Phi \mathcal{M}$ is finally given by

$$\nabla_{\Phi;\varphi} \tfrac{1}{2}\|\mathcal{P}\{\Phi\} - \widetilde{\Phi}\|_{\mathbb{M}} = \big(\mathcal{P}\{\Phi\} - \widetilde{\Phi}, \mathcal{P}\{\varphi\}\big)_{\mathbb{M}}. \tag{3.9}$$

In matrix notation, $\mathcal{M} = \|\mathcal{P}\{\Phi\} - \widetilde{\Phi}\|^2_{\mathbb{M}}$ is written as $\mathcal{M} = \frac{1}{2}(\mathbf{P\Phi} - \widetilde{\mathbf{\Phi}})(\mathbf{P\Phi} - \widetilde{\mathbf{\Phi}})^{\mathrm{T}}$, with $\widetilde{\mathbf{\Phi}}$ being the vector of measurements. For the derivative as given in (3.9), the equivalent matrix expression is

$$\mathbf{\nabla}_{\Phi;\varphi} \mathcal{M} = \big(\mathcal{P}\{\Phi\} - \widetilde{\Phi}, \mathcal{P}\{\varphi\}\big)_{\mathbb{D}} = (\mathbf{P\Phi} - \widetilde{\mathbf{\Phi}})\mathbf{P}^{\mathrm{T}}, \tag{3.10}$$

yielding all derivatives of $\mathcal{M}$ in the direction of base functions $\varphi_i$ simultaneously in a single vector.

### 3.1.3. Normalized Born Approach using Detection Operator Notation

The ratio of measured photon density $\widetilde{\Phi}_m$ at the emission wavelength $\lambda_m$ of a fluorochrome and measured photon density $\widetilde{\Phi}_x$ at the excitation wavelength $\lambda_x$ should be equal to the ratio of predicted measurement values $\widehat{\Phi}_m$ and $\widehat{\Phi}_x$,

$$\frac{\widetilde{\Phi}_m}{\widetilde{\Phi}_x} \stackrel{!}{=} \frac{\widehat{\Phi}_m}{\widehat{\Phi}_x} = \frac{\mathcal{P}\{\Phi_m\}}{\mathcal{P}\{\Phi_x\}},$$

where $\Phi_m$ and $\Phi_x$ are derived similarly to equation (2.21) as

$$\frac{\widetilde{\Phi}_m}{\widetilde{\Phi}_x} = \frac{\mathcal{P}\left\{\int_\Omega G(\mathbf{r},\mathbf{r}_m)\gamma\varepsilon c(\mathbf{r}_m)G(\mathbf{r}_m,\mathbf{r}_s)\right\}\, d\mathbf{r}_m}{\mathcal{P}\{G(\mathbf{r},\mathbf{r}_s)\}}. \tag{3.11}$$

In equation (3.11), $G(\mathbf{r}_1,\mathbf{r}_2)$ denotes again the Green function at $\mathbf{r}_1$ inside the diffuse domain $\Omega$ due to a point source at $\mathbf{r}_2$, while $c(\mathbf{r}_m)$ is the unknown concentration of fluorochrome at $\mathbf{r}_m \in \Omega$. As $\mathcal{P}$ is linear with respect to all expressions that are invariant of $\mathbf{r}$, the equation simplifies to

$$\frac{\widetilde{\Phi}_m}{\widetilde{\Phi}_x} = \int_\Omega \frac{\mathcal{P}\{G(\mathbf{r},\mathbf{r}_m)\}\gamma\varepsilon c(\mathbf{r}_m)G(\mathbf{r}_m,\mathbf{r}_s)}{\mathcal{P}\{G(\mathbf{r},\mathbf{r}_s)\}}\, d\mathbf{r}_m. \tag{3.12}$$

## 3.2. Trivial Operators

"Trivial" measurement operators are those operators that access parts of the domain $\Omega$ in a way usually not accessible during an experiment: they either access interior domain regions, or they access the whole boundary at once. They are called trivial as the corresponding matrix has only one non-zero entry in each row, this entry being equal to one.

### 3.2.1. Identity Operator

The most trivial operator is the identity operator $\mathcal{P}_{\Omega\to\Omega} : \Phi \mapsto \Phi$, so that $\mathbb{D} = \Omega$ and $\widehat{\Phi} = \Phi$, i.e.,

$$\mathcal{P}_{\Omega\to\Omega}\{\Phi(\mathbf{r})\} = \Phi(\mathbf{r}), \tag{3.13a}$$

or, in matrix notation, where **Id** is the identity matrix,

$$\mathbf{P} = \mathbf{Id}. \tag{3.13b}$$

### 3.2.2. Boundary Identity Operator

The second trivial operator introduced here is the boundary operator. Here, $\mathbb{D} = \partial\Omega$ and $\widehat{\Phi} = \Phi|_{\partial\Omega}$. It enables the measurement of all values on the exterior boundary $\partial\Omega$, but not within the full domain $\Omega$:

$$\mathcal{P}_{\partial\Omega\to\partial\Omega}\{\Phi(\mathbf{r})\} = \Phi(\mathbf{r}) \tag{3.14a}$$

If the index set $b$ contains the indices of all shape functions $\varphi_i$ with their support point located on the boundary, i.e., $b = \{b_1,\ldots,b_n\} = \{i|\exists\mathbf{r}_b \in \partial\Omega : \varphi_i(\mathbf{r}_b) = 1\}$, then the matrix elements $p_{i,j}$ of $\mathbf{P}$ are given by:

$$p_{i,j} = \delta_{b_i,j} \qquad \text{with } \delta\text{: Kronecker delta symbol} \tag{3.14b}$$

## 3.3. Detection Operators for Fiber-Based Measurements

The detection operators discussed in this section are used to model measurements obtained by a number of light-guiding fibers located on discrete points $\mathbf{d}_i$ of the boundary $\partial\Omega$. The detection space is given by $\mathbb{D} = \{\mathbf{d}_1,\ldots,\mathbf{d}_n\} \subset \partial\Omega$. The fact that measurements are obtained from discrete points on the boundary only will be denoted in the operator symbol by using the subscript $\mathbf{r}_b$.

### 3.3.1. Point-Like Detector Sensitivity

In this operator it is assumed that a detector fiber collects photons from a singe point on the boundary $\partial\Omega$, which is the simplest model available. Thus, the detector space $\mathbb{D}$ consists of a number of points $\mathbf{d}_i \in \partial\Omega$ on the boundary from which measurements are obtained directly, i.e., $\widehat{\Phi}_i = \Phi(\mathbf{d}_i)$. The operator is given by

$$\mathcal{P}_{\partial\Omega\to\mathbf{r}_b}\{\Phi(\mathbf{r})\}(\mathbf{d}) = \int_{\partial\Omega} \delta_0(\mathbf{d}-\mathbf{r})\Phi(\mathbf{r})\; d\mathbf{r} = \Phi(\mathbf{d}) \tag{3.15}$$

and in matrix notation elements are given by

$$p_{i,j} = \int_{\partial\Omega} \delta_0(\mathbf{d}_i-\mathbf{r})\varphi_j(\mathbf{r})\; d\mathbf{r}. \tag{3.16}$$

### 3.3.2. Finite-Area Sensitivity Profile

It could be argued that assuming a point-like sensitivity profile for fibers that have actual core diameters in the order of several hundred microns might lead to a model-mismatch, inducing artifacts in recovered images. To assess these possible effects in

the comparative study presented in chapter 4, another operator is introduced. In this operator, sensitive fiber tips are not regarded as single points, but as having a finite circular area with radius $\rho$ and center $\mathbf{d} \in \partial\Omega$. Then, $\widehat{\Phi}$ is not equal to values of $\Phi$ at different positions, but is the average or sum of $\Phi$ over the whole area. The according detection operator is given by

$$\mathcal{P}_{\partial\Omega\to\mathbf{r}_b\pm\rho}\{\Phi(\mathbf{r})\}(\mathbf{d}) = \int_{\partial\Omega} H\big(\rho^2 - \|\mathbf{d}-\mathbf{r}\|^2\big)\Phi(\mathbf{r})\; d\mathbf{r}, \tag{3.17}$$

where $H$ is the heaviside step function:

$$H(x) = \begin{cases} 0 & \text{if } x < 0 \\ 1 & \text{if } x \geq 0 \end{cases}$$

### 3.3.3. Interpolated Detector Model

The third fiber-modeling operator presented is different from the previous two in that it assumes that intensities detected by individual fibers can be interpolated between detection points so that virtually a continuous area on the boundary is imaged by a discrete number of detectors. For non-contact imaging as described later on, CCD images are also assumed to cover a connected area of the outer surface $\partial\Omega$. The following operator was introduced to assert the comparability between contact and non-contact imaging and to assess whether or not covering the full area has an effect on reconstruction quality (see chapter 4).

Again, point-detector fibers are considered, located at boundary positions $\mathbf{d}_i \in \partial\Omega$. However, it is additionally assumed that detected intensities can be interpolated between these discrete boundary points at least inside a certain region $\mathcal{H} \subseteq \partial\Omega$, for example the convex hull of $\{\mathbf{r}_d\}$. Given a number of bilinear interpolation functions $\hat{\varphi}_i$ with $\hat{\varphi}_i(\mathbf{d}_j) = 1$ if and only if $i = j$, this interpolation can be expressed by $\Phi|_{\mathcal{H}} = \sum_i \widehat{\Phi}_i \hat{\varphi}_i$. Furthermore, it can be assumed that $\hat{\varphi}_i(\mathbf{r}) = 0$ for all positions $\mathbf{r} \notin \mathcal{H}$.

Detector readings shall not be given by the photon density $\Phi$ at the discrete points $\mathbf{d}_i$. Instead, the projection onto the space spanned by interpolation functions $\hat{\varphi}_i$ shall be used, i.e.,

$$\widehat{\Phi}_i = \big(\Phi, \hat{\varphi}_i\big)_{\mathcal{H}}. \tag{3.18}$$

Then the detection operator becomes

$$\mathcal{P}^i_{\partial\Omega\to\partial\Omega}\{\Phi(\mathbf{r})\}(i) = \int\limits_{\mathbf{r}_b\in\partial\Omega} \hat{\varphi}_i(\mathbf{r}_b)\Phi(\mathbf{r}_b)\; d\mathbf{r}_b. \tag{3.19}$$

The corresponding detection matrix consists of elements

$$p_{i,j} = \big(\hat{\varphi}_i, \varphi_j\big)_{\partial\Omega}. \tag{3.20}$$

## 3.4. Non-Contact Detection Operators

In section 3.3, detectors were assumed to be located on the domain boundary $\partial\Omega$, and thus the detection operators always mapped $\partial\Omega$ to detector readings on a part of $\partial\Omega$. For non-contact detection, detectors in free space are considered, i.e., $\mathbb{D} = \{\mathbf{d}\} \subset \mathbb{R}^3 \backslash \Omega$. All points $\mathbf{d} \in \mathbb{D}$ will, for the examples considered herein, always be located on a plane, resembling the natural topology of CCD-detectors used for the actual experiments. The plane will in the operator symbol be denoted by $\mathcal{D}$.

Both of the operators presented in this section assume that the angular distribution of the exitance is isotropic, i.e., that for any point on the surface, the same amount of light is emitted in any direction. In the diffusion model, this is true for any point inside $\Omega$, as isotropicity is the fundamental assumption of the the diffusion equation. However, at the exterior boundaries, due to the refractive index mismatch and the resulting effect of total internal reflection, the actual exitance distribution should not be isotropic, as reported by Vera et al [87, 88].

This effect, on the other hand, does not only depend on the refractive index mismatch, but also on surface roughness—for a rough surface, any finite area of the boundary will have a large distribution of surface normal vectors, thus reducing the effect of total internal reflection. For optical tomography in plastic phantoms, assuming an isotropic exitance has previously shown good agreement with measurements [2].

### 3.4.1. Ripoll's Fiber-Bundle Operator

The non-contact operator introduced in this section was proposed by Ripoll [2] and has been subsequently used experimentally in phantom studies [4] as well as in animal studies [5]. It considers detection by a bundle of virtual light-collecting fibers located in free space, each fiber having a certain numerical aperture (NA). The numerical aperture is define as the sine of half the acceptance angle of the fiber, see figure 3.3. The detection by such a bundle is described by

$$ {}^{\mathrm{F}}\mathcal{P}^{i}_{\partial\Omega\to\mathcal{D}}\{\Phi(\mathbf{r})\} = \iint\limits_{\substack{\mathbf{d}\in D \\ \mathbf{r}_b\in\partial\Omega}} \Phi(\mathbf{r}_b)\,\Gamma(\mathbf{r}_b,\mathbf{d})\,d\mathbf{r}_b\,d\mathbf{d}, \tag{3.21} $$

where the weighting function $\Gamma$ for each surface-detector point pair is defined by

$$ \Gamma(\mathbf{r}_b,\mathbf{d}) = \xi(\mathbf{r}_b,\mathbf{d})\frac{f\,(\mathrm{NA}-\sin\theta_d)}{|\mathbf{r}_b-\mathbf{d}|^2}\cos\theta_b\cos\theta_d. \tag{3.22} $$

In (3.22), $\xi$ is an indicator function of visibility which is 1 if $\mathbf{r}_b$ is visible from $\mathbf{d}$, and 0 otherwise, and $f$ models the acceptance of the virtual fiber. The acceptance $f$ is

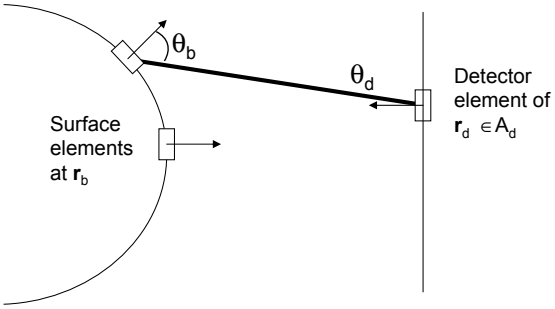


**(a)** Ripoll's operator [2]. This operator models the depth of field via $f$, but it requires telecentric image formation.

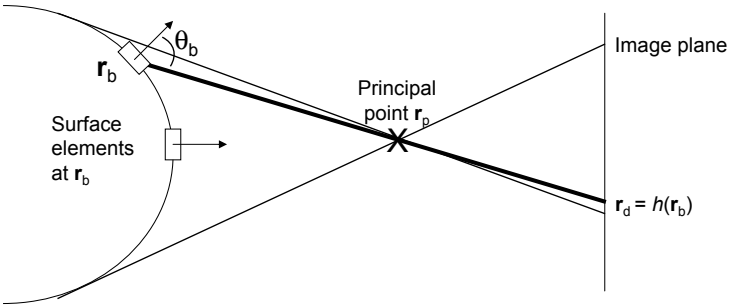


**(b)** Operator for lens detection [3]. While depth of field effects are not included in the model, different magnification ratios are, and thus a correct perspectivic projection can be achieved.

**Figure 3.2:** Non-contact measurement operators

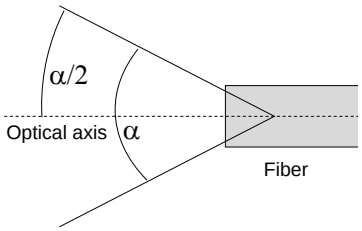


**Figure 3.3:** Definition of the numerical aperture (NA). The NA is defined as the sine value of half the acceptance angle of a light-guiding fiber (or a lens, or an objective). The full acceptance angle in the figure is denoted by $\alpha$, so that NA = $\sin\frac{1}{2}\alpha$.

modeled by a Gaussian bell shape function with a full width half maximum (FWHM) of the numerical aperture NA. Angles $\theta_b$ and $\theta_d$ are the angles between $\mathbf{r}_b - \mathbf{d}$ and the surface and detector normal, respectively, as illustrated in figure 3.2a.

For CCD-based imaging it is assumed that groups (bins) of pixels on the CCD-chip resemble individual fiber tips located on the focal plane of the objective lens.

The lens needs to be slightly defocused so that the focus is located at least at a small distance from the object's exterior surface to avoid that the term $|\mathbf{r}_b - \mathbf{d}|$ becomes zero in equation (3.22).

Disadvantages of the operator in (3.21) are its inability to describe lens-induced aberrations, such as a variable magnification ratio depending on object / lens distance, geometric aberrations, and vignetting [44]. In the following section, a derived operator modeling a lens-based system will be introduced and later on used.

### 3.4.2. Perspectivic Non-Contact Operator

For lens-based non-contact detection, a virtual plane of detectors $\mathbb{D} = \{\mathbf{d}\} \subset \mathbb{R}^3$ is considered, resembling the active area of the image sensor (CCD) used. This plane with surface normal $\mathbf{n}_p$ is located at a certain distance from the diffuse domain $\Omega$. The exitance on $\partial\Omega$ is projected onto this detector plane through a pinhole, which is the simplest model for the effects of an objective in geometrical optics [44]. The pinhole is located at $\mathbf{r}_p \in \mathbb{R}^3$. The detection scheme is presented in figure 3.2b in comparison to Ripoll's fiber-bundle operator described before. While the projection through a pinhole cannot model lens aberrations or depth of field effects, it does model the distance-dependent change in magnification ratios which leads to the "fish eye" effect known from extreme wide angle lens images.

Perspectivic projection through the pinhole is performed using ray tracing. The bijective function $h : \mathbf{r}_b \in \partial\Omega \mapsto \mathbf{d} \in \mathbb{D}$ is implicitly defined by the conditions

$$\mathbf{n}_p \cdot \left(h(\mathbf{r}_b) - \mathbf{d}^0\right) = 0 \tag{3.23a}$$

and

$$\exists \lambda \in \mathbb{R} : \ \mathbf{r}_b + \lambda \left(h(\mathbf{r}_b) - \mathbf{r}_b\right) = \mathbf{r}_p. \tag{3.23b}$$

Equation (3.23a) forces $h(\mathbf{r}_b)$ to be located on the detector plane, while (3.23b) guarantees that the connecting line between $h(\mathbf{r}_b)$ and $\mathbf{r}_b$ goes through the pinhole. The bijectivity of $h$ leads to neglect of depth of field effects, as each point on the boundary $\partial\Omega$ maps to at most one point in $\mathbb{D}$. It is also assumed that no aberrations except for the change in magnification ratio occur.

The detector plane is not divided into individual bins. Instead, the interpolation approach is used which was also employed for the interpolating fiber detector operator from section 3.3.3. Values detected on that plane are approximated as a sum of bilinear interpolation functions $\varphi$, $\Phi(\mathbf{d}) = \sum_i u_i \varphi_i(\mathbf{d})$, defined on a equidistant rectangular grid. This choice of base functions and grid creates a linear interpolation on the entire detection area. In principle, more complex interpolation functions or irregular grids optimized for the system geometry could be used to exploit

features of higher order in the measurements. Coefficients $u$, which take the role of detector values, were determined using the projection operator:

$$ {}^{\mathrm{L}}\mathcal{P}^{i}_{\partial\Omega\to\mathcal{D}}\{\Phi(\mathbf{r})\} = \int_D \Phi\big(h^{-1}(\mathbf{d})\big)\,\Gamma_h(\mathbf{d})\,\varphi_i(\mathbf{d})\,d\mathbf{d} \tag{3.24} $$

The non-contact sensitivity function $\Gamma_h$ is given by

$$ \Gamma_h(\mathbf{d}) = \cos\theta_d |\mathbf{r}_p - h^{-1}(\mathbf{d})|^{-2} f(\mathbf{d}), \tag{3.25} $$

which is again the Lambertian of the exitance multiplied with a "vignetting" function $f$ describing the overall sensitivity of detector position $\mathbf{d}$. Vignetting could be calibrated for; however, the normalization performed in the normalized Born approach also eliminates $f$, so that in the following chapters, $f$ will be discarded and assumed to be constant. The middle term in (3.25) is the square boundary / pinhole distance and models the loss of sensitivity due to the decrease of the solid angle of the lens surface with distance.

# Chapter 4.

# Comparative Analysis of Non-Contact and Fiber-Based Detection Systems

Felix qui potuit rerum cognoscere causas.*

*(Virgil, Georgica 2, 490)*

## 4.1. Overview

WHILE the theoretical framework for non-contact detection of diffused light had been developed before the work presented herein was even started, see for example publications by Ripoll [2, 77, 78], Bluestone [23], or Hebden [43], and even though a proof-of-concept for small animal imaging with free space detectors had already been published previously by the author of this thesis [4, 5], advantages connected to non-contact detection were mostly hypothesized: while the simplification of experimental and calibration procedures are obvious—this can simply be deduced from the rather complex calibration procedures involved in fiber-based imaging, see the sections below—an increase in signal-to-noise ratio and thus in resolution has not been proved yet.

This chapter presents an experimental comparison of "classical" fiber-based optical tomography—where detecting optodes are located on the exterior boundaries of the imaged object—against non-contact detection under otherwise identical experimental conditions. Entities of interest were differences with respect to (1) spatial resolution of reconstructed data sets, (2) the achievable accuracy in quantifying the concentration of fluorescent dyes hidden in tissue, and (3) the overall experimental complexity. Some of the results presented herein have meanwhile been published by the author and colleagues [3].

* "Fortunate is he who can understand the nature of things."

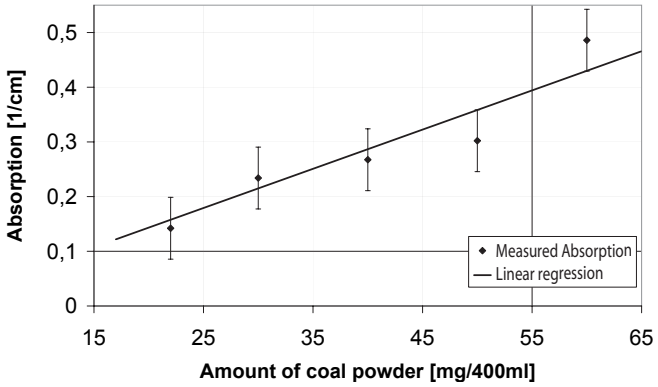


**Figure 4.1:** Plot of the absorption coefficient induced by different amounts of coal powder added to the phantom resin, and linear trend. Whiskers show standard error of measurements. Additionally, 880mg $TiO_2$ per 400ml resin were added to create a scattering of $\mu_s' = 10cm^{-1}$. Absorption and scattering coefficients were measured using diffuse optical spectroscopy (see text).

---

At the end of this chapter, weight matrices for different detection operators—as introduced in chapter 3—and also for different numbers of detectors are analyzed using singular value decomposition. To supplement the numerical analysis, appropriate experimental results are presented.

## 4.2. Methods and Materials

### 4.2.1. Phantom Development

To create controlled experimental conditions, homogeneous phantoms of known optical properties and geometrical shape had to be built first. In the literature, two general types of phantoms are described: liquid phantoms based on fatty suspensions (like intralipid) mixed with absorbing liquids, e.g., india ink [30]; or solid phantoms that are cast using a translucent resin mixed with scattering and absorbing particles [35, 37, 91]. To create an appropriate amount of scattering within the phantoms, usually titanium dioxide ($TiO_2$) particles are added to the liquid resin. $TiO_2$ is chosen due to its white color and high refractive index $n > 2.5$, which makes it a highly reflective substance[†] [83]. As absorbers, again either some dyes or pigments are used, for example active coal, india ink, etc. The amounts of scattering and ab-

[†]Because of its high reflectivity, titanium dioxide is often used as the main color component in white wall paint and in sun blocking lotions.

sorbing particles per volume of phantom have to be calibrated to create specific tissue-like optical properties for the wavelengths used.

As different tissues exhibit different behavior with respect to scattering and absorption, homogeneous "tissue" phantoms usually try to mimic the mean coefficients of mixed tissue [32, 61, 71]. Depending on purpose, a scattering coefficient between 5–20cm$^{-1}$ and an absorption coefficient between 0.1–0.5cm$^{-1}$ are chosen [93].

Phantoms used in the experiments described herein were cast under vacuum conditions using a two-component polyurethane resin (Megithan, Alpina Technische Produkte GmbH, Geretsried, Germany) mixed with titanium dioxide particles (AppliChem GmbH, Darmstadt, Germany) to control the scattering coefficient, and carbon powder (Sigma Aldrich) to control the absorption coefficient. The correct amounts of coal and $TiO_2$ were calibrated by building a series of slab shaped phantoms of 2cm thickness using different concentrations of absorbing and scattering particles. Optical properties resulting from each individual phantom recipe were subsequently determined using time-resolved spectroscopy [31], see figure 4.1, performing five independent measurements on each phantom.

All phantoms used for experiments described later on were cast according to the following instructions which lead to an absorption coefficient of $\mu_a = 0.3\text{cm}^{-1}$ and a reduced scattering coefficient of $\mu_s' = 10\text{cm}^{-1}$, according to the calibration measurements:

1. For **400ml** of phantom volume use 140ml of resin component A (main component) and 260ml of component B (hardener[‡]).
2. Measure **880mg** $TiO_2$ and **40mg** carbon powder. Mix $TiO_2$ and carbon powder in a mortar until the powder takes on a homogeneous gray color.
3. Add component A and powder in a tumbler, put the tumbler in a vacuum bell jar. Remove air bubbles using a vacuum pump while stirring powder and resin with an externally applied magnetic stirrer.
4. After reaching a homogeneous solution, open the bell jar and add the hardener (component B). Stir by hand using a spatula for one minute. Then close the bell jar and switch on vacuum pump again. Stir for 15min.
5. Slowly fill solution into mold, trying to avoid the formation of new bubbles.
6. Let resin harden for 48 hours. Remove from mold and temper for 60min at 80°C in an appropriate oven. According to the manufacturer, tempering increases the durability and hardness of the resin.

[‡]Terms were used according to the manufacturer. The amount of hardener used has to be 1.5–2 times the amount of the "main" component.

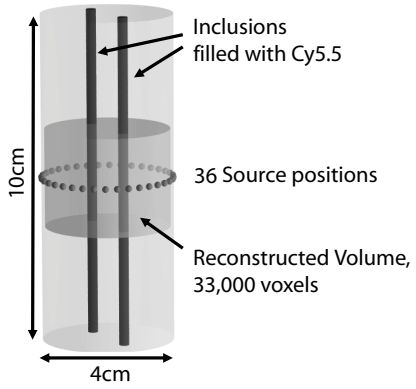


**Figure 4.2:** Sketch of the diffuse cylindrical phantom (length 10cm, diameter 4cm, diameter of each inclusion 4mm) with two inclusions. The single inclusion phantom has similar geometry, but the single inclusion only has a diameter of 3mm.

Phantoms were cast in the shape of cylinders having slightly more than 4cm diameter and 10cm length. Tempered phantom material was then machined to match the exact desired size. Holes were also drilled into the cylindrical phantoms that were subsequently filled with different dyes to create fluorescent inclusions. A sketch of the phantom used in subsequent experiments is shown in figure 4.2.

### 4.2.2. Experimental Setup

Experiments aimed at comparing non-contact versus fiber-based FMT in an otherwise identical setting. The experimental setup, in which the measurements later on described were performed, is shown in figure 4.3. A collimated beam created by a temperature-stabilized diode laser source (emission at 670nm, 5mW optical power, ±2% drift in output power, LGTC diode series manufactured by LG-Laser Technologies, Kleinostheim, Germany) was directed perpendicular onto a diffuse cylindrical phantom (∅4cm, height 10cm, $\mu_a = 0.3\text{cm}^{-1}$, $\mu_s' = 10\text{cm}^{-1}$, fig. 4.2; manufactured as described in the previous section). The cylindrical phantom contained one inclusion of 3mm diameter or two fluorescent inclusions of 4mm diameter parallel to its main axis, each located 1cm off-center. The phantom was mounted on a rotational base to allow measurements from different angles without moving the laser or the detection system.

For fiber-based measurements, a semi-cylindrical aluminum holder was attached to the phantom, 180° opposite of the laser beam's point of incidence, see figures 4.3a and 4.3b. An image of the holder itself, without a phantom mounted in it, is depicted in figure 4.3c. The holder fixed plastic optical fibers (∅1mm, NA of 0.46), allocated in three rows distant 5mm from one another, on the phantom's outer

surface. Within each row, the angular spacing between adjacent fibers was 10°. The holder itself covered 180° of the cylindrical boundary, thus holding 19 fibers per row. A total of 56[§] fiber-based detector readings were acquired per source position. The phantom mounted inside the holder could be rotated at 10° steps while the holder's position was fixed. This resulted in 36 different source positions for which diffuse projection data could be acquired. The other ends of the fibers were arranged in a matrix pattern and imaged by a cooled CCD camera with 512 × 512 pixels and 16bit dynamic resolution (Princeton Instruments, Trenton, NJ, USA).

For non-contact imaging, the fiber holding device was removed and the CCD camera placed directly in front of the phantom, viewing onto the phantom from the opposite side of the laser, i.e., in transillumination geometry (figure 4.3d). A wide angle objective (CNG from Schneider, Bad Kreuznach, Germany) was employed for image acquisition, enabling the camera to view the full phantom of 10cm length even at a short lens-object distance of less than 10cm, thus maximizing sensitivity and minimizing the spatial dimensions of the setup.

The fiber-based setup as used herein has not been used previously in any publication. Usually, for fiber-based imaging data is detected from optode located on the whole surface, not just one half of the surface, as is the case fo the semi-cylindrical fiber holder. It might be that the placement of optodes in this setup is not optimal. However, this geometry was chosen to allow a direct comparison of datasets from fiber-based as well as non-contact imaging, as both techniques use data from the same area of the boundary. Nevertheless, the results as presented herein should be valid in general, as the imaged area could always be enlarged by adding more fibers and, in the non-contact case, by adding more detecting cameras.

In both setups, for the acquisition of fluorescence signal excitation light was filtered out using a combination of two long pass glass filters with 695nm and 715nm limit wavelengths (colored glass types RG695 and RG715, Schott AG, Mainz, Germany), which were placed in front of the lens. The transmission characteristics of the filter combination used is given in figure 4.4. The transmission of each of the filters was measured with a photo spectrometer (V-570, JASCO Corporation, Tokyo, Japan), while the transmission of the combination was calculated by multiplying both transmission curves with each other. It is important to note that transmission measurements were performed by the author, as the Schott only specifies the transmission of their filters for wavelengths where transmission is above $10^{-2}$.

The maximum transmission value is 0.82, the attenuation at the excitation wavelength (solid line in the figure) is $3.6 \cdot 10^{-4}$. Still, some excitation light will leak

[§]The mounting was prepared for 3 × 19 = 57 detector fibers. One fiber position at the boundary of the central ring turned out to be mechanically unusable, leaving 56 detector fibers to be used.

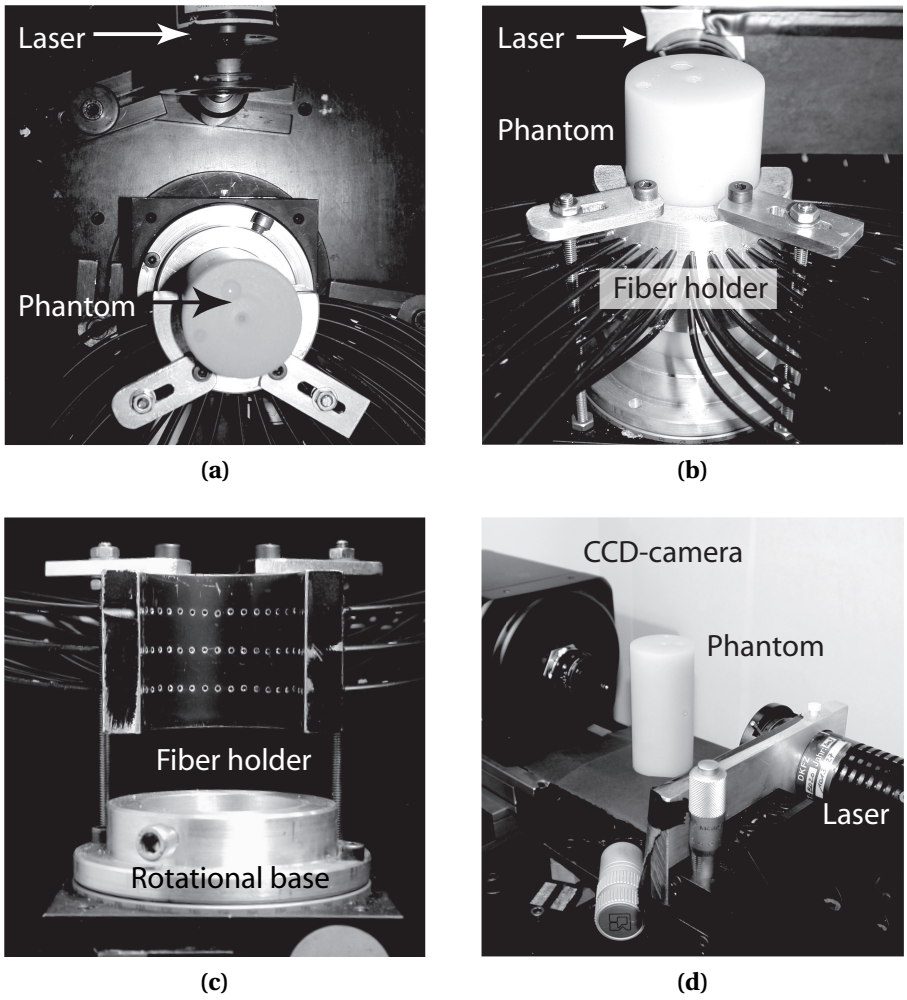


**Figure 4.3:** Experimental setup for (a)–(c) fiber-based and (d) non-contact imaging.

though the filters and cause background signal which has to be removed from the images prior to reconstruction, as described below.

To optimally use the dynamics of the CCD-camera for image acquisition, for both setups—fiber-based and non-contact—exposure times were individually determined for each experiment so that the dynamic range was optimally used in acquired images without leading to saturation. Within each experiment, exposure time was held constant for all 36 projections. For excitation images, acquired without any filters, exposure times were chosen between 100–200ms in both setups. Fluorescence images were acquired for a time of 40–120s for the fiber-based setup and 20–45s for the non-contact setup in most of the experiments, unless stated otherwise. Lower necessary exposure times correlated with higher fluorochrome concen-

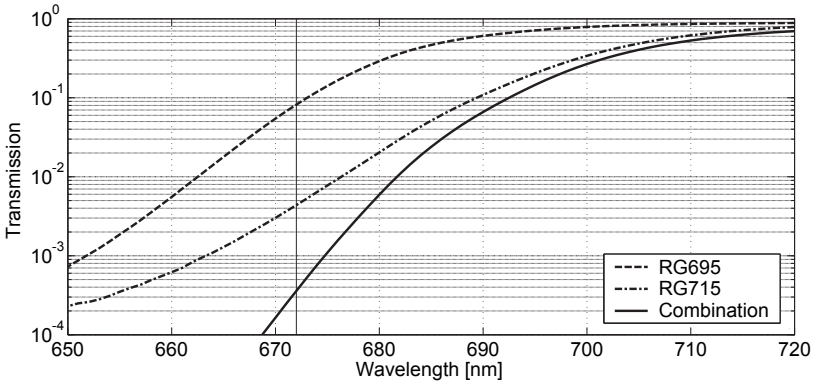


**Figure 4.4:** Transmission diagram for the individual glass filters and their combination, experimentally obtained with spectrometric measurements performed by the author. The excitation wavelength of the laser was 672nm and is indicated by a vertical line in the diagram.

trations, as then the fluorescent signal was, of course, lower. Acquired projection images were normalized by the exposure time used.

To accomplish background removal, it is assumed that $\widetilde{\Phi}_x = \widehat{\Phi}_x$ and that $\widetilde{\Phi}_m = \widehat{\Phi}_m + q\widehat{\Phi}_x$, $q \in \mathbb{R}$, where $q$ is the transmission of the fluorescence filters at the excitation wavelength. In other words, light measured without filters will only contain a negligible amount of emitted fluorescence light, while light filtered through fluorescence filters will still consist of a considerable amount of excitation light. The first assumption $\widetilde{\Phi}_x = \widehat{\Phi}_x$ is justified as the exposure times to acquire $\widetilde{\Phi}_x$ are in the order of 0.1s, while for $\widetilde{\Phi}_m$, exposure times are above 30 seconds. Therefore the fluorescence signal contained in $\widetilde{\Phi}_x$ should be at least two orders of magnitude lower. On he other hand, in the emission images, leakage can clearly be identified in images obtained without fluorescent dye present—although the attenuation through the filter is in the order of $10^{-4}$. Therefore, $\widehat{\Phi}_x > 10^6\widehat{\Phi}_m$ (two orders of magnitude originate from the difference in exposure times). The CCD-camera, however, has a dynamic range of only 16bit, i.e., less than $10^6$. Thus, no fluorescence signal should be detectable in images obtained without a filter.

Experimental measurements of $q$ were performed using the experimental setups as described above by measuring on a homogeneous phantom without fluorescent inclusions. Here, $\widehat{\Phi}_m = 0$, so that $q = \widetilde{\Phi}_m/\widetilde{\Phi}_x$. However, a significant difference from the predicted value of $q$ was observed, also differing between both setups used: for the non-contact setup, $q = 1 \cdot 10^{-3}$ was determined, while fiber detectors gave a ratio of $q = 8 \cdot 10^{-5}$. For background removal, the experimentally determined $q$-values were used.

### 4.2.3. Positioning of the Laser Source

To ensure that the quality of reconstructed images was not compromised by a deviation between assumed and real source position, the laser had to be aligned with the setup to achieve that the point of incidence on the phantom was located exactly 180° opposite the central fiber detector.

To calibrate the position exactly, the central detector fiber was removed. A plastic cylinder the size and shape of the phantom was mounted in the holder. Using a 1mm drill bit, the detector position was marked on the cylinder by drilling from the outside through the detector fiber's mounting hole. Subsequently, the cylinder was rotated by 180° and the laser source positioned to hit the resulting drill mark. After removal of the calibration cylinder, it was verified that the free beam of the laser hit the central fiber hole exactly, additionally asserting that the beam was aligned perpendicular to the phantom's outer surface.

### 4.2.4. Calibration of Fiber Sensitivities and Coupling Issues

When optical fibers are used to transport light from a surface point to a detecting camera, the loss of light in each fiber is influenced by the coupling efficiency at both fiber ends, the length of the fiber, and additionally the bending of the fiber or the presence of small defects in the fiber material. During the setup of the fiber holding device (fig. 4.3c), coupling issues and fiber efficiencies were constantly measured and fibers polished or replaced, if necessary, to optimize detection sensitivity.

Although the normalized Born approach described in equation (3.12) individually corrects for detector sensitivities, and thus it seems unnecessary to have exactly the same efficiency for all fibers, it is desirable to have at least nearly the same coupling and light transport efficiencies. This is due to the fact that fiber outputs were measured using a CCD which has not only a limited dynamic range but also uses the same dynamics for all pixels. Detection fibers exhibiting very weak coupling and transport efficiency would lead to detected values with decreased signal to noise ratio as compared to other fibers.

To assess differences in fiber coupling and transport efficiencies, all fibers were mounted in the holder and then evenly illuminated. To achieve homogeneous light input for the cylindrical arrangement of fibers, *electroluminescent foils* (EL-foils) were employed (Lumitech, Switzerland). EL-foils are flat capacitors where the dielectric insulator between electrodes is made of an organic substance that emits light when exposed to a changing electric field (thus the name "electroluminescence"). Emitted light is completely isotropic and very homogeneous over the whole area of the foil, ±5% deviation in light output as claimed by the manufacturer. The homogeneity was manually verified using an integrating sphere detector.

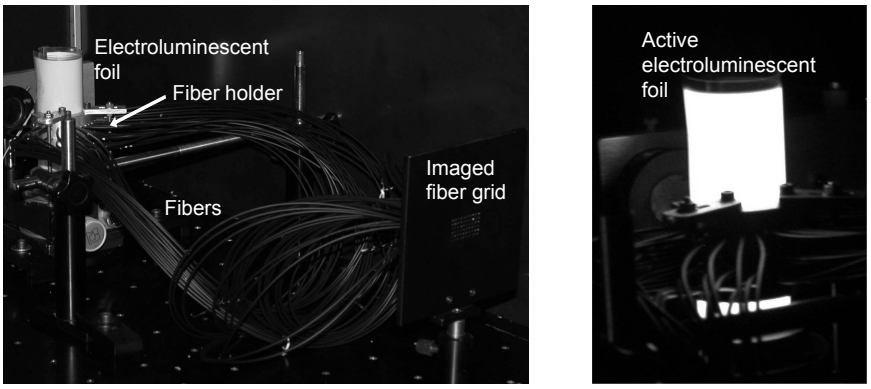


**Figure 4.5:** Calibration of fiber sensitivities using an electroluminescent foil.

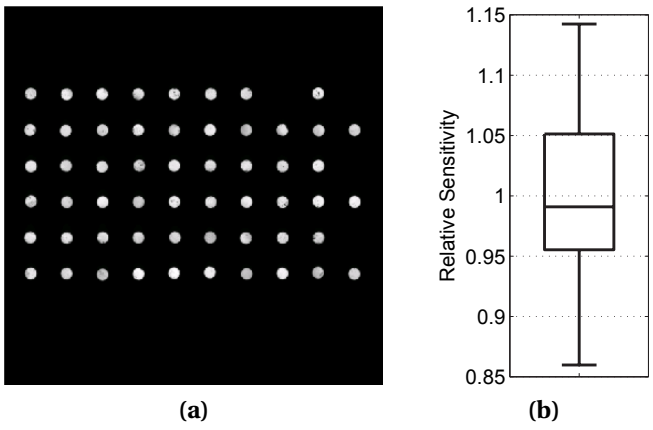


**Figure 4.6:** Fiber coupling efficiencies. Fiber were illuminated using an electroluminescent foil, fig. 4.5. (a) Mounting plate with fiber outputs, as imaged by the CCD-camera. (b) Relative intensity for all fiber ends. The Box show lower, middle and upper quartile. Whiskers span the whole range.

Images of the fiber grid were acquired using a CCD camera. Within these images (as shown in figure 4.6a), fiber tips were automatically segmented. To extract detector readings from every fiber tip, the values of all pixels belonging to one fiber tip in the image were summed up.

The EL-foil was fixed on an aluminum cylinder (fig. 4.5) having the same size as the phantom, and then mounted in the holder. Fibers were removed from the holder, polished or replaced, and remounted until the inter-fiber deviations became negligible (see fig. 4.6). In the final setup the maximum inter-fiber deviation amounted to ±15%.

For the reconstructions presented herein, determined coupling efficiencies were not taken into account, as they did not have a significant effect on image quality in initial experiments. For normalized Born reconstruction, this does not come as a surprise: As stated before, the normalization process corrects for differences in detection sensitivity, and the additional noise introduced by the foil actually was already in the order of the observed inter-fiber efficiency differences (±5% vs. ±15%).

### 4.2.5. Calibration of Fiber Positions

In addition to measuring the individual fiber sensitivities, also the actual fiber positions were controlled. As it proved to be difficult to measure fiber positions directly, an indirect approach of exactly locating the mounting holes in the holder was used. First, the interior side of the holder, where the holder could be mounted to a phantom, was dredged with graphite powder. Second, a sheet of paper was attached to the inner side of the holder to produce a negative image of the fiber holes (fig. 4.7a). Third, the paper sheet was removed and an image of it acquired. On this image, the centers of fiber mounting holes were manually determined and compared to the predicted, ideal positions (fig. 4.7b). As the position of the source in all experiments was determined by positioning the laser exactly opposite of the central fiber, this fiber was used as the reference position, i.e., it was assumed to have a deviation of 0 from its ideal position. The position of all other fibers in the image was determined relative to the central fiber. The accuracy of this type of measurement is in the order of 1/100mm, resembling the pixel resolution of the image shown in figure 4.7a.

The maximum deviation in position was less than 0.5mm in vertical direction, with 50% of the fibers being located within a ±0.1mm range, resulting in a positional error of less than 10% of the mesh resolution used in the reconstruction process (see below). Vertical displacement should not cause strong artifacts in the experiments performed, as the phantom used was invariant along the vartical axis and furthermore, only the quality of central transversal slices was evaluated. Regarding the angular deviation, which should have a stronger effect on quality, actual fibers were displaced at most 0.3mm, resembling a maximum error of 0.3°.

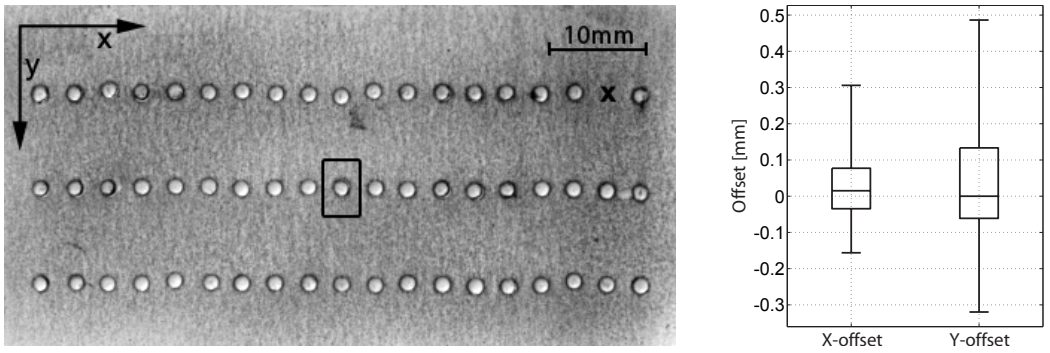


**(a)** **(b)**

**Figure 4.7:** Verification of fiber positions. (a) Image taken of the paper sheet previously attached to the interior side of the holder and showing the fiber positions. The box marks the central fiber, which defines the origin. On the upper right corner, the defect fiber mount is visible, marked by an *x*. (b) Box-whisker plot of deviation from real fiber positions to ideal positions. The position of the central fiber (marked with a box) was used as a reference. An x-offset of 0.1mm is equivalent to an angular error of 0.3° for that fiber. The box indicates the lower and upper quartile of the distribution of deviations, whiskers span the whole range of obtained deviations.

To determine whether the small deviations in fiber positions had an effect on the reconstruction algorithm, both the ideal and the real positions were subsequently used in reconstructions. However, no significant difference could be observed in the results between images reconstructed with the real or ideal fiber positions. All results described in the following sections used the ideal fiber positions.

### 4.2.6. Calibration of Non-Contact Projection

The only parameter to adjust in the non-contact detection operator ${}^{\mathrm{L}}\mathcal{P}^{i}_{\partial\Omega\to\mathcal{D}}$ is the lens-object distance, i.e., the position of the pinhole $\mathbf{r}_p$ used to perform the perspectivic projection. As mentioned before, a decrease in light intensity caused by vignetting will be canceled out due to the normalization performed in the normalized Born approach.

To determine the pinhole position, a paper bearing a regularly dot pattern was wrapped around the imaged phantom. Then, this phantom was imaged with the setup using white light illumination. Dot positions in the images were predicted using projection formulas (3.23a) and (3.23b). The pinhole position, which determines the prediction of dot position, was changed in a fitting process to optimally match predicted and actual dot positions in the image. The pinhole was determined to be located at a distance of 6.5cm from the phantoms central axis. A sketch of the gen-

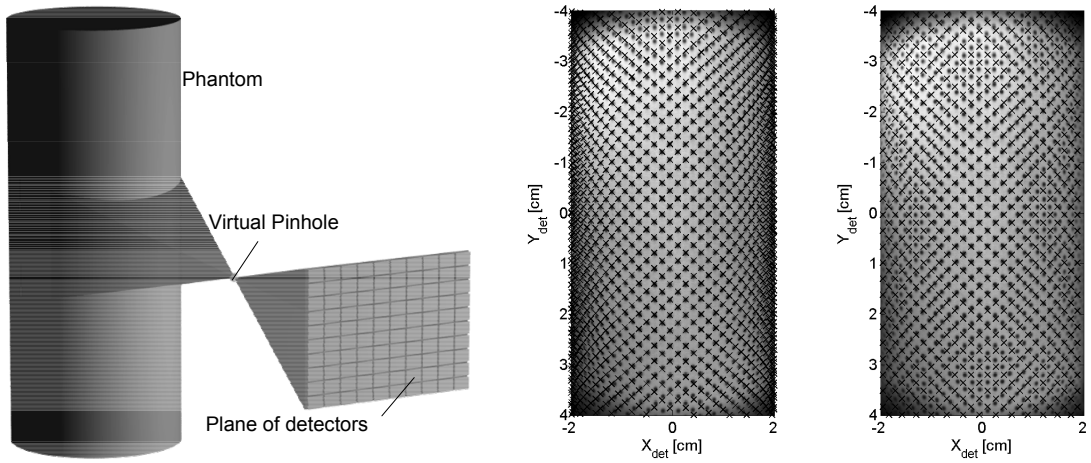


**(a)** Sketch of the setup

**(b)** Perspectivic projection

**(c)** Orthographic projection

**Figure 4.8:** Calibration of non-contact detection. A regular dot pattern on the phantoms surface was captured (background image) and compared against predicted dot positions (shown as crosses). Detector values were extracted from $y$-coordinates between $-0.5\text{cm} \leq y \leq +0.5cm$, as in the fiber-based setup. (a) Depiction of the non-contact detection operator used. (b) Optimal result obtained by using the perspectivic projection formula, as given by equations (3.23a) and (3.23b). The pinhole distance was determined to be 6.5cm. Dots and crosses match fairly well with the exception of regions close to the upper or lower boundaries of the images. (c) The necessity to use perspectivic projection as compared to orthographic projection is illustrated in this image, where orthographic projection was used. Positions of actual and predicted dots located laterally do not match well.

eral principle of the non-contact detection operator is given in figure 4.8a, while the result of the fitting process is presented in figure 4.8b, where little crosses superimposed on the original white light image denote the predicted dot positions.

Apparently, the projection works well in the center of the image, but quality of the fit deteriorates toward the vertical image boundaries due to other lens aberrations. However, detectors for all reconstructions presented in this chapter were placed only within the region of $-2\text{cm} < x < +2\text{cm}$ and $-0.5\text{cm} < y < +0.5\text{cm}$—resembling the same area covered by the fiber optics detector system—where these aberrations did not yet become apparent.

The necessity to use a pinhole model instead of the orthographic model used in (3.21) is clearly illustrated in figure 4.8c. Here, the same dot pattern is shown together with an orthographic mapping of predicted dot positions. The orthographic mapping consists of an orthogonal projection onto the detector plane without using

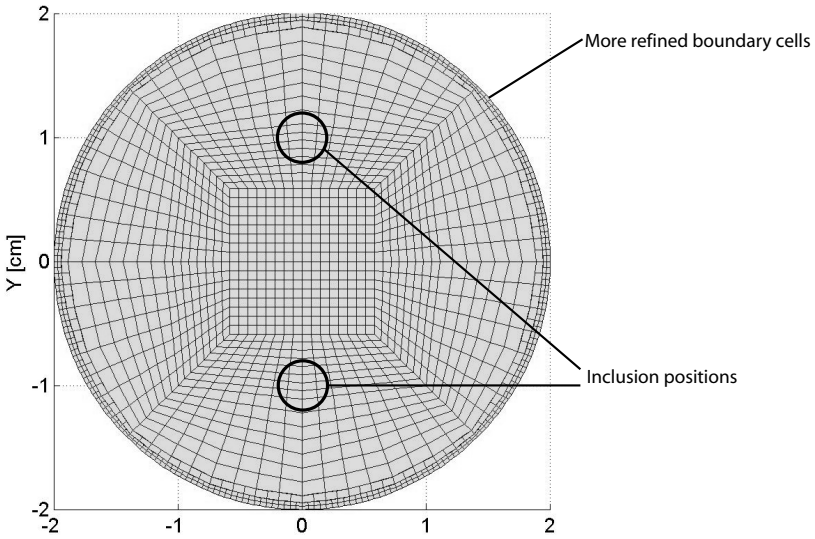


**Figure 4.9:** Central transversal slice of the finite element mesh employed in the reconstructions. The support points of the shape functions used (first order Lagrangian elements) are located at the mesh vertices. The grid was refined toward the border to increase source modeling accuracy (see text). Both circles denote the location of inclusions in the phantom.

the pinhole. This is a valid mapping for telecentric lenses. Apparently, the orthographic projection model does not accurately model the lens used.

### 4.2.7. Reconstruction

Reconstructions were performed using the normalized Born approach extensively described in chapter 2.3. Green functions were calculated through a FEM system implemented in C++ using the DEAL.II library [21]. The system matrix was built applying proper Robin boundary conditions, as described in [18, 81], see also chapter 2.4.2, with a surface reflection coefficient of $A = 10$, resembling a refractive index of $n = 1.5$. For all experiments described herein the same cylindrical finite element mesh consisting of 291,000 degrees of freedom (=unknowns) was employed, of which 33,000 degrees of freedom were used for the reconstruction of fluorochrome concentrations. The central slice of this mesh is depicted in figure 4.9. Elements on the outer boundaries of the cylindrical domain were more refined than interior cells to allow for accurate source modeling, as described by Schweiger et al [81]. To reduce the number of unknowns, this outer rim of small cells was not taken into account for reconstruction. This fact explains the outer black rim in the reconstruction results as presented later on.

Weight matrix inversion was carried out for all experiments using randomized algebraic reconstruction technique (ART) [5, 48] with 50 iterations and a relaxation parameter of $\varrho = 0.1$. Concerning the use of detection operators, for fiber based measurements the point-fiber operator $\mathcal{P}_{\partial\Omega\to\mathbf{r}_b}$ from equation (3.15), the finite area fiber profile operator $\mathcal{P}_{\partial\Omega\to\mathbf{r}_b\pm\rho}$ from (3.17) and the interpolating operator $\mathcal{P}^i_{\partial\Omega\to\partial\Omega}$ from (3.19) were consecutively employed. Results did not differ much, and thus reconstructed images are only presented for $\mathcal{P}^i_{\partial\Omega\to\partial\Omega}$. A discussion regarding the information acquired by different detection operators is given in section 4.4.

For non-contact measurements, an array of 57 detectors ($19\times3$ detectors) was extracted from CCD images acquired unless specified otherwise, covering an angular section of 180° on the phantom's outer surface. The region used for non-contact detection therefore was equal in size to the region measured by the fibers. The non-contact operator ${}^{\mathrm{L}}\mathcal{P}^i_{\partial\Omega\to\mathcal{D}}$ from equation (3.24) was computed numerically by first projecting all boundary points of the FEM-mesh onto the detector plane, as given by the mapping function $h$ defined by (3.23a) and (3.23b), then interpolating linearly between all the projected points and finally solving the integral using Gaussian quadrature. The operator ${}^{\mathrm{F}}\mathcal{P}^i_{\partial\Omega\to\mathcal{D}}$ from (3.21) was not used, as it did not allow for wide angle lens acquisition.

### 4.2.8. Singular Value Decomposition (SVD)

Singular value decomposition is the name of a matrix transformation changing the representation of a matrix $\mathbf{W}$ into $\mathbf{W} = \mathbf{USV}^{\mathrm{T}}$. Here, $\mathbf{W}$ is a rectangular $m\times n$ matrix (the weight matrix as described in previous chapters, with $m > n$), $\mathbf{U}$ is a $m\times n$ matrix with orthonormal columns, i.e., $\mathbf{U}^{\mathrm{T}}\mathbf{U} = \mathbf{Id}$, and $\mathbf{V}$ is an orthonormal $n\times n$ matrix. $\mathbf{S}$ is a diagonal $n\times n$ matrix containing the so-called *singular values* of $\mathbf{W}$. Singular values are equal to the square roots of the eigenvalues of $\mathbf{WW}^{\mathrm{T}}$. The ratio of largest to smallest singular value of a matrix is called the *condition number C* of that matrix. The higher this number, the worse the conditioning of the examined matrix.

In principle, once the decomposition has been calculated, it can be used to easily calculate the matrix inversion (2.26), as $\mathbf{W}^{-1} = \mathbf{VS}^{-1}\mathbf{U}^{\mathrm{T}}$, due to the orthogonality of $\mathbf{U}$ and $\mathbf{V}$. Please note that $\mathbf{W}^{-1}$ shall denote the pseudo inverse $\mathbf{W}^{-1}\mathbf{W} = \mathbf{Id}$, as before. As $\mathbf{S}$ is a diagonal matrix, its inverse is also trivial to calculate. The rapid matrix inversion based on the SVD allows for real time imaging as demonstrated by Hampel [41], but only if the weight matrix can be decomposed prior to imaging. Herein, however, the SVD was employed only to investigate the conditioning of the weight matrix for different detection operators and different detector numbers.

Singular value analysis has been used extensively in publications to investigate differences in image resolution between different optode setups or different number of source / detector pairs, see for example the review by Arridge [19], or the reports

| Experiment | Exposure (no filter) | Exposure (fluor.) |
|---|---|---|
| 500nmol/l | 100ms | 90s |
| 250nmol/l | 100ms | 90s |
| 125nmol/l | 100ms | 90s |
| 63nmol/l | 100ms | 90s |
| 31nmol/l | 100ms | 90s |

**(a)** Fiber-based setting

| Experiment | Exposure (no filter) | Exposure (fluor.) |
|---|---|---|
| 500nmol/l | 100ms | 25s |
| 250nmol/l | 100ms | 25s |
| 125nmol/l | 100ms | 30s |
| 63nmol/l | 100ms | 30s |
| 31nmol/l | 100ms | 45s |

**(b)** Non-contact setting

**Figure 4.10:** Exposure times used for acquiring single-inclusion datasets.

by Culver [29] and Graves [38]. The number of singular values in $S$ that are above the accuracy of the system (the system noise) is equal to the number of equations in the linear system that can be considered linearly independent of each other.

The number of system equations in the case of optical tomography is equal to the number of source / detector combinations, see equation (2.25). Thus, only if an increased number of sources or detectors also increases the number of singular values above system noise level, the resulting image resolution will improve. Otherwise, the matrix will simply become ill-conditioned.

To perform an SVD-analysis of the weight matrix, the according subroutines of the publicly available LAPACK library [16] were used. For large matrices as involved herein, the decomposition required about 20min computation time on a standard Linux PC (Pentium IV processor, 3GHz clock frequency, 2GB of memory). Singular values as presented herein were normalized with respect to the largest singular value for comparability between individual results, as not the absolute values but only the ratio between smallest to largest value decide on ill-conditioning.

## 4.3. Comparison using Equal Detector Resolutions

### 4.3.1. Single Fluorescent Inclusion

In a first series of experiments, the single inclusion phantom was filled with five different dilutions of the fluorochrome Cy5.5 (Amersham Biosciences, Piscataway, NJ, USA) and imaged with both setups, as described above. The dye concentrations used were 500nmol/l, 250nmol/l, 125nmol/l, 63nmol/l, and 31nmol/l, respectively. Calibration of dye dilutions were performed by photospectrometric measurements of the dilutions (using the V-570 photo spectrometer, JASCO Corporation, Tokyo,

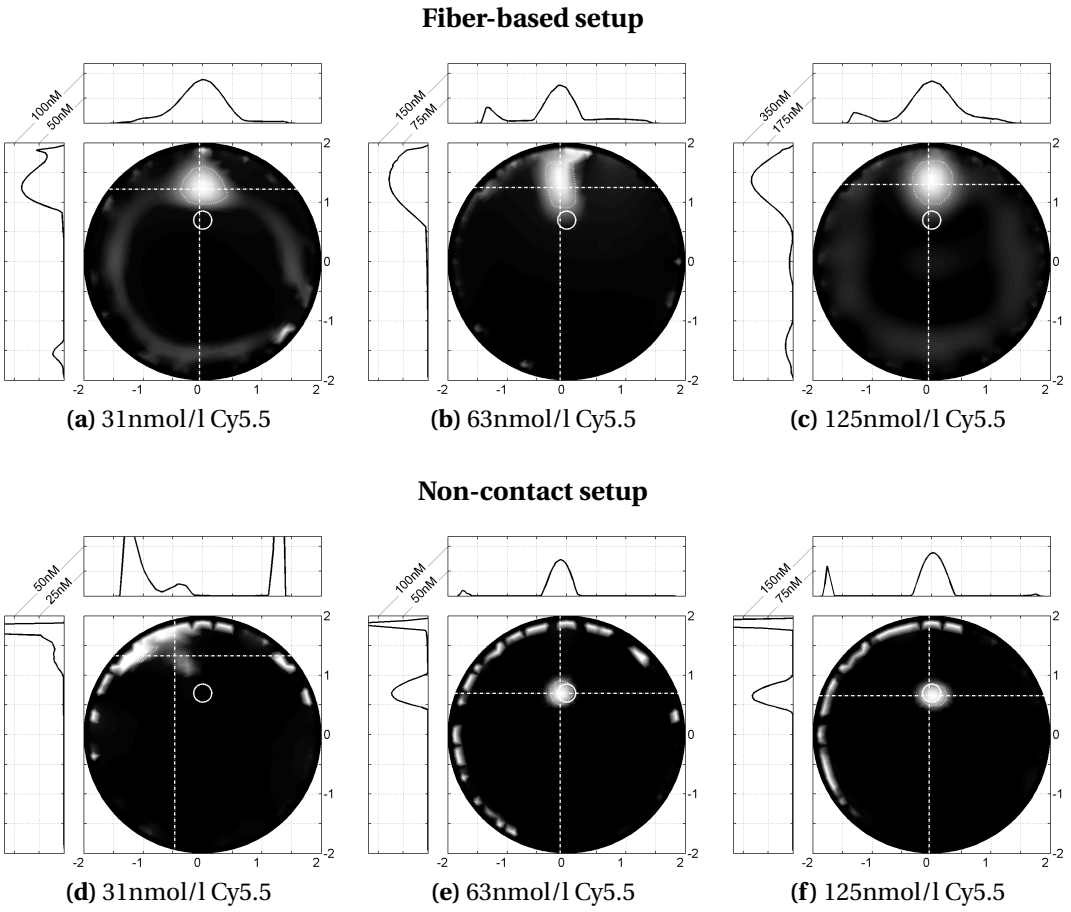


**(a)** 31nmol/l Cy5.5 **(b)** 63nmol/l Cy5.5 **(c)** 125nmol/l Cy5.5

**(d)** 31nmol/l Cy5.5 **(e)** 63nmol/l Cy5.5 **(f)** 125nmol/l Cy5.5

**Figure 4.11:** Central transversal slices of reconstructed volumes with intensity profiles along x- and y-axis. The position where the profiles were extracted are denoted by dashed lines in the image. The gray scale was adjusted for each subfigure individually to cover the full range of values.

Japan). All dilutions of the fluorescent dye were mixed with intralipid and India ink to match the optical properties of the phantom. Exposure times for the experiments are given in figure 4.10.

For fiber-based acquisitions, central transversal slices of reconstructed data sets computed for the three lowest concentrations are shown in figures 4.11a–c (results from higher concentrations look similar to the 125nmol/l slice). In all cases, the fluorescent inclusion appeared in the images as a nearly circular region of increased values close to the phantom border. The estimated diameter of the inclusion in reconstructed images was 1cm (real value: 3mm), located 0.6cm (real value: 1cm) distant from the border. For all experiments, the mean intensity values of the inclusion

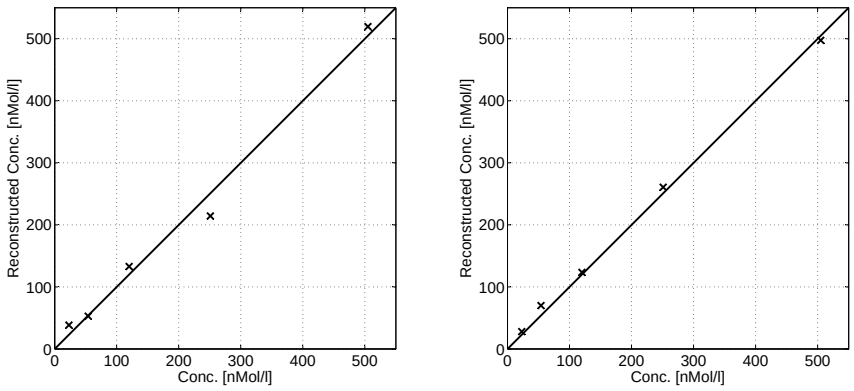


**(a)** Fiber-based system **(b)** Non-contact system

**Figure 4.12:** Linearity of reconstructed fluorochrome concentrations in single inclusion experiments.

were extracted from reconstructed images and plotted against the actual concentration used, see figure 4.12. The extracted mean values show a linear correlation with the concentration of fluorochrome.

Fluorescent inclusions in the reconstructions of data sets acquired with non-contact detection appeared on average 1.1cm away from the boundary in the images, having a diameter < 5mm (fig. 4.11d–f; again, results from higher concentration measurements look similar to the 125nmol/l slice). Again, the mean reconstructed values of the inclusions were extracted. They also scaled linearly with the concentration used in the experiments (figure 4.12b). However, in contrast to the fiber-based measurements described above, in the 31nmol/l experiment the fluorescent inclusion appeared shifted toward the boundary, see figure 4.11d, and did not reconstruct properly.

### 4.3.2. Two Fluorescent Inclusions

A more sophisticated evaluation of the imaging methods was performed using a double inclusion phantom in both setups subsequently. A total of four different fluorochrome concentrations were used for imaging: 500nmol/l (A), 250nmol/l (B), 125nmol/l (C), as well as 63nmol/l (D). As before, the fluorescent dye was calibrated using a spectrophotometer and mixed with intalipid and ink to match the phantom's optical properties. For each experiment the inclusions were filled with two different concentrations of dye. Exposure times were set to the values given in figure 4.13. In total, data sets for eight concentration pairs were acquired and reconstructed (A-A, A-B, A-C, A-D, B-B, C-B, C-C, and C-D). In the central slice of the reconstructed data set a region of interest was extracted automatically for each inclusion by considering

| Experiment | Exposure (no filter) | Exposure (fluor.) |
|---|---|---|
| A-A | 150ms | 40s |
| A-B | 150ms | 40s |
| A-C | 150ms | 50s |
| A-D | 150ms | 50s |
| B-B | 300ms | 120s |
| C-B | 150ms | 90s |
| C-C | 150ms | 90s |
| C-D | 200ms | 90s |

**(a)** Fiber-based setting

| Experiment | Exposure (no filter) | Exposure (fluor.) |
|---|---|---|
| A-A | 100ms | 20s |
| A-B | 100ms | 20s |
| A-C | 100ms | 20s |
| A-D | 100ms | 25s |
| B-B | 100ms | 36s |
| C-B | 100ms | 40s |
| C-C | 100ms | 40s |
| C-D | 80ms | 40s |

**(b)** Non-contact setting

**Figure 4.13:** Exposure times used for acquiring double-inclusion datasets. Exposure times are given for each concentration pair measured. Used concentrations were 500nmol/l (A), 250nmol/l (B), 125nmol/l (C), and 63nmol/l (D).

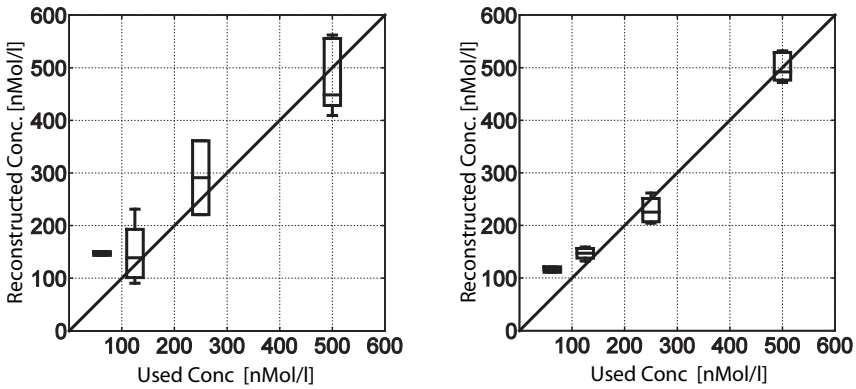


**(a)** Fiber-based system **(b)** Non-contact system

**Figure 4.14:** Linearity of reconstructed fluorochrome concentrations for the double-inclusion phantom. Box-whisker plots for (a) fiber based setup, (b) non-contact setup. Whiskers span the whole range of reconstructed values; boxes show the upper, middle, and lower quartile.

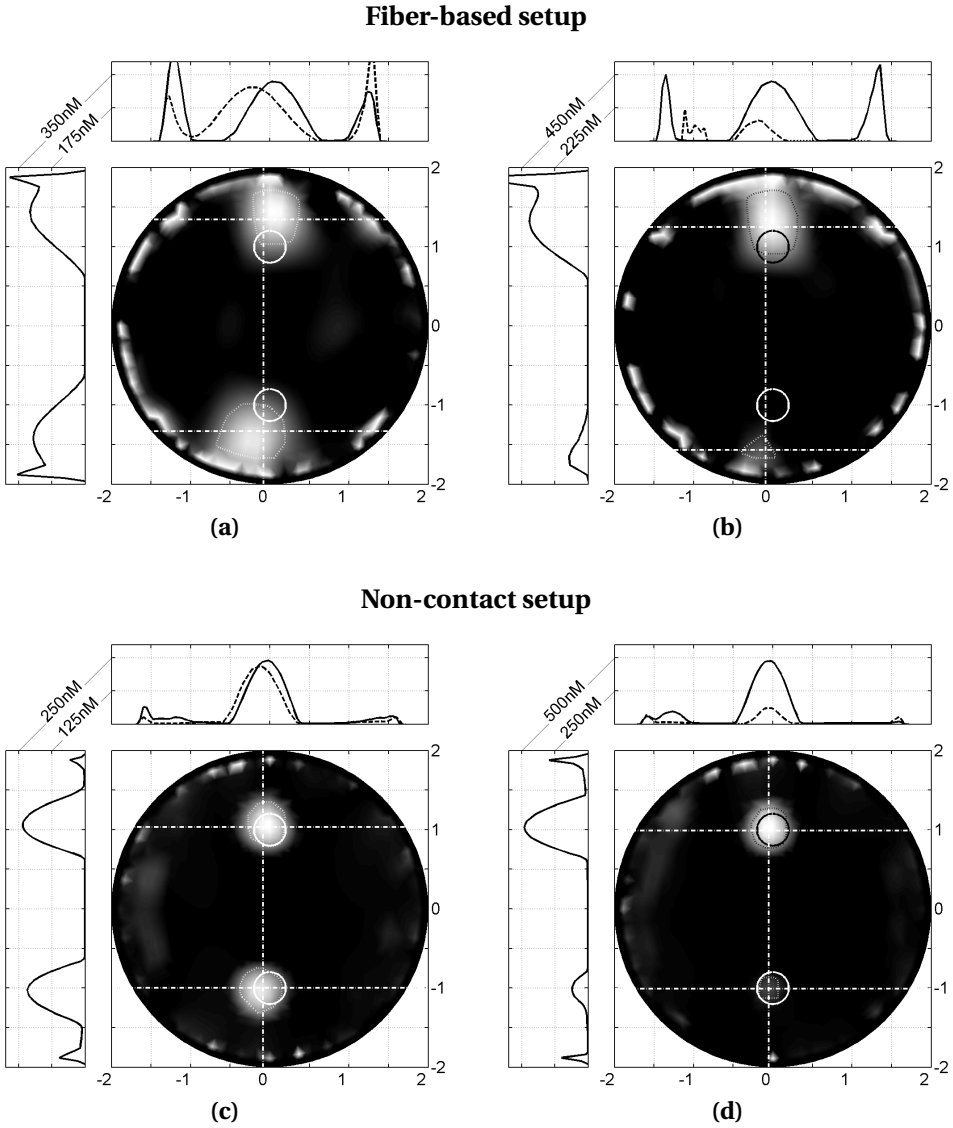


**Figure 4.15:** Central transversal slices of reconstructed volumes (double inclusion phantom) with intensity profiles along x- and y-axis. In the horizontal profiles, dashed lines correspond to the lower inclusion (at $y = -1$). The position where the profiles were extracted are denoted by dashed lines in the image. Parts (a) and (c) show an experiment with 250nmol/l dye in both inclusions. Part (b) and (d) show an experiment with 500nmol/l dye in the upper inclusion and 63nmol/l dye in the lower inclusion. The top row consists of fiber-based results, the bottom row of non-contact results. Circles indicate the actual shape and position of the inclusions. The gray scale was adjusted for each subfigure individually to cover the full range of values.

all data points with values above 50% of the maximum reconstructed value, i.e., by considering the full width half maximum (FWHM) region of the reconstructed inclusion. The mean value of this region was assumed as a measure for the reconstructed concentration of the respective inclusion. This resulted in a total of 5 extracted values for concentration A, 3 for B, 5 for C, and 2 for D, for each setup. These values were plotted against the actual concentration (figure 4.14). The corresponding linear regression line is also shown in the figure. Additionally, location and size of the reconstructed inclusions were analyzed (figure 4.16). Reconstructed slices themselves for two select concentration pairs are shown exemplary for both, fiber-based and non-contact acquisition in figure 4.15. In depicted slices the FWHM region from which reconstructed values were extracted for the concentration linearity charts 4.14 are indicated with dotted lines.

Again, inclusion diameters are overestimated in the fiber-based case, and their location moved toward the boundary. Also, reconstructions seem to depend on the difference in dye concentration. The greater the difference, the smaller the reconstructed inclusion of lower concentration becomes, as exemplary visible in the upper row of figure 4.15. This could be an explanation for the large spread in the linearity charts shown in figure 4.14a.

Reconstructions obtained with both the fiber-based as well as the non-contact setup resolved the two inclusions regardless of the difference in concentrations (see figure 4.15 for representative examples). Reconstructing the fiber-based data, inclusions appeared up to 5.9mm away from the expected position, on average 2.7mm (figure 4.16a). Reconstructed diameters ranged from 2.9mm to 7.3mm, on average 6.2mm, over-estimating the actual value by 50% (figure 4.16b). The quality of reconstructions strongly depended on the concentration difference between the inclusions: for similar concentrations, the accuracy of reconstructed position and size was the highest, while as the concentration difference increased, the inclusion of lower concentration moved towards the border (compare figures 4.15a and 4.15b).

In non-contact reconstructions, location and size of the inclusions were resolved with <1mm accuracy (figure 4.16). The inclusions' centroids were, on average, 0.6mm distant from the actual location, in the worst case 1.3mm, see figure 4.16a. Inclusion diameters were on average 4.3mm, ranging from 1.7mm to 5.3mm (figure 4.16b).

For all data sets, reconstructed values increased linearly with dye concentration. However, a constant bias of unknown origin led to an overestimation of low concentrations (figure 4.14). In fiber-based reconstructions, estimated concentrations spread over ±80nmol/l (figure 4.14a), whereas for the non-contact setup (figure 4.14b) the range was significantly smaller (±20nmol/l).

Theoretically, no constant offset should be needed, i.e., the regression line should go through the origin. However, estimated fluorochrome concentrations are

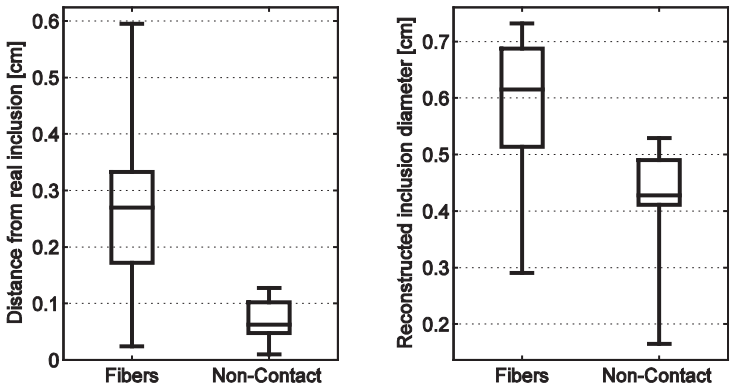


**(a)** Localization accuracy

**(b)** Estimated diameter of inclusions

**Figure 4.16:** Spatial accuracy of reconstructions. (a) Distance between centroid of the reconstructed inclusion and actual inclusion center. (b) Diameter of reconstructed inclusion. The actual diameter was 0.4cm. Whiskers span the whole range of acquired values; the box indicates upper, middle, and lower quartile of the value distribution.

clearly biased, at least for the lowest concentration used (figure 4.14b). Contrary to the fiber-based data, image quality was invariant of the concentration difference (compare figures 4.15c and 4.15d).

### 4.3.3. Influence of Pixel Averaging

A possible explanation of the better reconstruction performance of non-contact acquired data would be the fact that in non-contact images, detector values are extracted by averaging over or interpolating between many image pixels, thus reducing noise in the images. To test the effect of pixel averaging on image quality, reconstructions were additionally computed for all experimental data using only single pixels as detector readings in CCD acquired images.

Exemplary, a slice of the reconstructed image data is shown in figure 4.17a. Other data sets looked similar or better in quality than the slice shown. Both inclusions could always be identified but deteriorated a bit in shape, see especially the lower inclusion in 4.17a. However, although image quality decreased due to using single pixels instead of averaging over multiple pixels, the effect is not strong enough to account for the big quality difference between non-contact images and fiber-based images that could be observed before.

Also, again the regression of reconstructed image values versus used dye concentrations was examined in the same way as described before. The result is shown in figure 4.17b. Here, the use of only single pixels versus averaged pixel values clearly

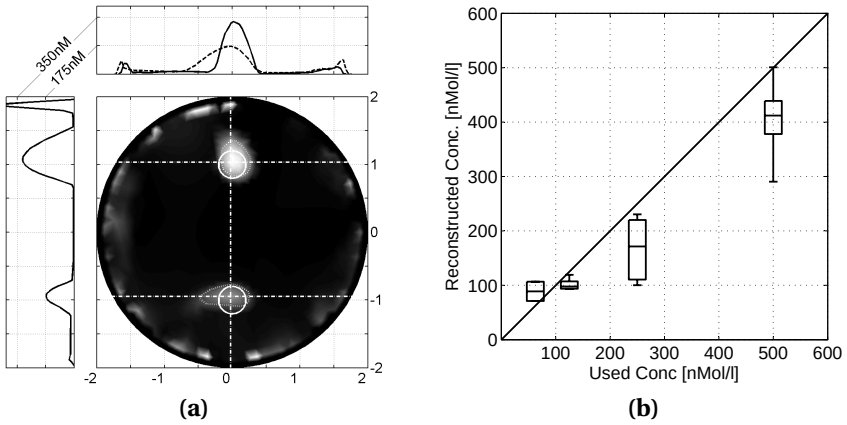


**(a)** **(b)**

**Figure 4.17:** Influence of pixel averaging on image quality. (a) Reconstructed slice of the experiment with 250nmol/l of dye in both inclusions (36s exposure time for fluorescence images), computed by using only single pixels on the projection images to extract detector values; compare to figure 4.15c. (b) Linearity of reconstructed concentration values using single pixels instead of pixel averaging; compare to figure 4.14b. As before, whiskers span the whole range of values, boxes indicate lower, middle and upper quartile.

disturbs the ability of the algorithm to clearly quantify concentrations. This can also be observed in the reconstruction shown in figure 4.17a, where the lower inclusion did result in an estimate of only half the concentration of the upper inclusion, although both inclusions contained the same amount of dye. The spread of concentration estimates was in the region of the spread observed for fiber-based measurements, as presented earlier in figure 4.14a.

### 4.3.4. Influence of Signal-to-Noise Ratio on Image Quality

Instead of pixel averaging, it could also be argued that the improvement in reconstruction quality for the non-contact case might be caused by the fact that the dynamics of fiber-based acquisitions are higher than the dynamics observed in the detected non-contact data. Thus, the signal to noise ratio for fiber-based data sets is lower for data points having low intensity, which could lead to a deterioration of results. The difference in dynamics is depicted in figure 4.18, where the signal acquired without filters by the middle row of the fibers (figure 4.18a) is compared to the central horizontal profile of the corresponding image acquired with the non-contact setup (figure 4.18b). For central fibers, the acquired intensity is by a factor of 8 lower than for lateral fibers. In the non-contact images, central pixels detect intensities that are only by a factor 2 lower than the intensities detected by lateral pixels.

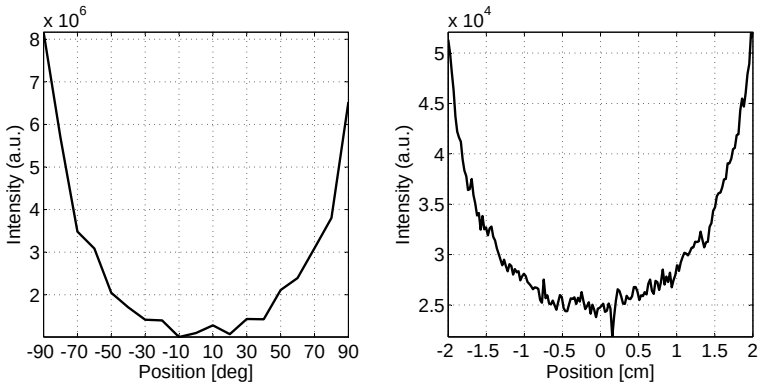


**(a)** Fiber-based setup **(b)** Non-contact setup

**Figure 4.18:** Dynamics of fiber-based vs. non-contact measurements. Shown are intensities measured without the use of a filter. (a) Intensitites detected on the central row of a fiber-based measurement. (b) Horizontal profile of an image acquired with the non-contact setup. The difference in absolute values between (a) and (b) is due to the non-contact measurements being actual pixel values, but the fiber-based data being the integral over the whole region appearing as a fiber output on the image (as shown for instance in figure 4.6a). Of importance are not the absolute values, but rather the ratio between lowest and largest value (see text).

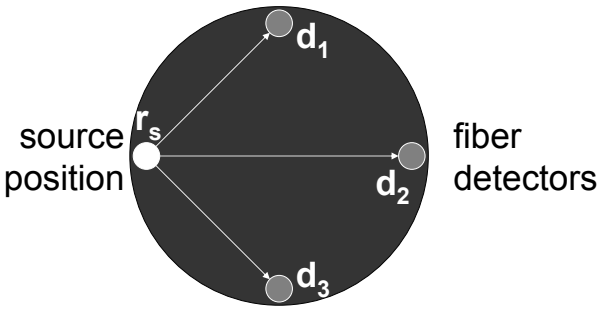


**Figure 4.19:** Origin of different dynamics for fiber-based imaging. Lateral detector fibers ($\mathbf{d}_1$ and $\mathbf{d}_3$ in the sketch) are located closer to the source $\mathbf{r}_s$ than more central fibers ($\mathbf{d}_2$), and thus detect higher signals. As all fiber detectors are captured using a single CCD, this decreases the signal-to-noise ratio of central detectors, as the exposure time is determined by laterally recorded intensities.

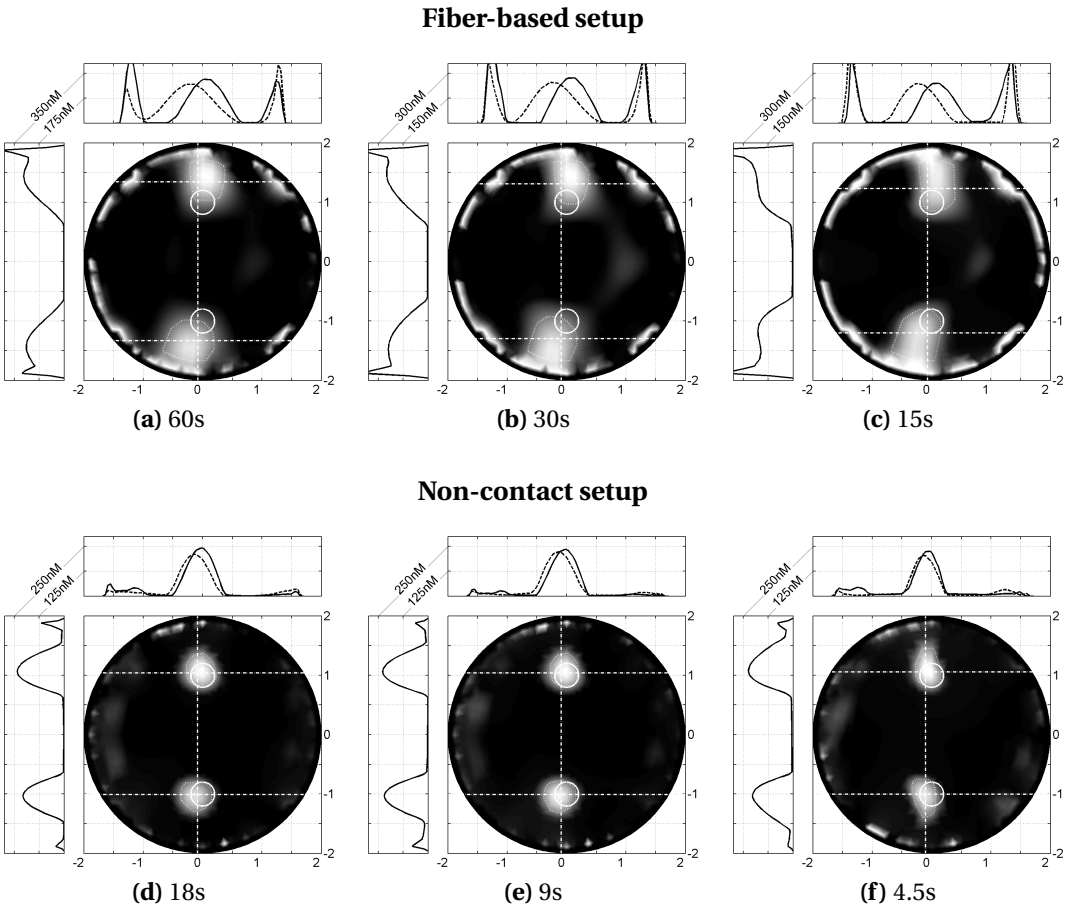


**Figure 4.20:** Sensitivity of image quality in fiber-based and non-contact measurements on the signal to noise ratio. Signal to noise was decreased by deliberately using lower than necessary exposure times, as stated below the images.

---

This effect is caused by the fact that in non-contact detection geometry, due to the fact that the lateral surface areas of the cylindrical phantom are imaged under a nearly 90° angle, which strongly attenuates detected light intensities in these regions. This attenuation is modeled by the cosine term in non-contact detection equations (3.22) or (3.25). In fiber-based measurements, however, there is no such weighting term as fibers are mounted perpendicular to the surface to yield optimal coupling. The lateral surface areas are located closest to the incident source position, so they receive the highest signal, figure 4.19. On the other hand, the information obtained from these fibers is lower than for central fibers, as for the latter light has probed a greater part of the imaged domain.

To verify if the decreased signal-to-noise ratio in fiber-based data sets leads to the observed lower reconstruction quality, for both setups, fiber-based as well as non-contact, the original exposure times used for the experiments were decreased by a factor of 2, 4 and 8. According data sets were reconstructed for the concentration combination B-B. Results are shown in figure 4.20. The original exposure times amounted to 120s for the fiber-based setup and 36s for the non-contact setup. Depicted are only slices reconstructed from measurements acquired using 50%, 25% and 12.5% of the optimal exposure time. Reducing the exposure time by a factor of 1/2 leads to the loss of one bit in dynamics, so the results as illustrated in 4.20c and 4.20f were obtained from data having a dynamic range reduced by 3bit in total.

Surprisingly, the change in image quality is not very strong for either setup. While artifacts present in the center of fiber based reconstructions become more pronounced (visible in the top row of figure 4.20), the actual intensity profiles and shape of the reconstructed inclusions do not change. For non-contact measurements, after the loss of three bits, image quality deteriorates (figure 4.20, bottom row), but apparently reconstructions are still of significantly higher resolution than in the fiber-based reconstructions. This illustrates that the different dynamics of the two different detection techniques do not have a strong effect on image quality and that the improvements are due to a different factor.

## 4.4. SVD Analysis and Increased Detector Resolutions

In this section, weight matrices for different detection operators and different detector resolutions were calculated and their singular values analyzed. This was performed for the three fiber detection operators discussed (section 4.4.1, as well as for different numbers of non-contact detectors (section 4.4.2). As these investigations are primarily of theoretical nature, implications were consequently verified on actual experimental data (section 4.4.3).

As described in section 4.2.8, the useful information contained in a matrix is related to the number of singular values above the system's bit precision. The bit precision is not easy to determine: The weight matrix was calculated with double precision, using a mantissa of 52bits, which would support a minimum singular value of $2^{-52} \approx 2 \cdot 10^{-16}$. However, Green functions used to calculate weight matrix entries were computed using the finite element method with a maximum residual of $10^{-18}$ and thus will not be completely accurate. The precision will be below 52bits, but should be better than single precision, using a mantissa of 23bits and therefore supporting a minimum singular value of at least $2^{-23} \approx 2.3 \cdot 10^{-10}$.

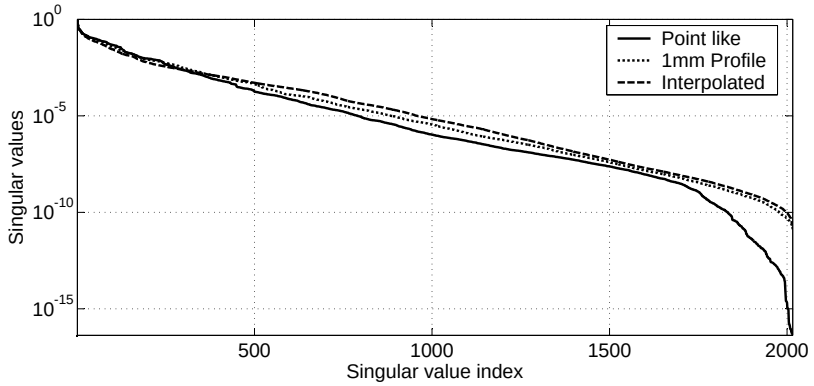


**Figure 4.21:** Plot of the normalized singular values for different fiber-based measurement operators.

### 4.4.1. SVD Analysis of Fiber-Based Weight Matrices

First of all, the influence of using different fiber-based detection operators for calculating weight matrix entries was investigated. Weight matrices for $19 \times 3$ detectors and 36 source positions, as used in the experiments, were determined for the point operator $\mathcal{P}_{\partial\Omega\to\mathbf{r}_b}$, the finite area operator $\mathcal{P}_{\partial\Omega\to\mathbf{r}_b\pm\rho}$ using a fiber diameter of 1mm, and the interpolating fiber detector $\mathcal{P}^i_{\partial\Omega\to\partial\Omega}$. Subsequently, the respective SVDs were calculated. Plots of the normalized singular values for all three detection operators are shown in figure 4.21.

For point measurements $\mathcal{P}_{\partial\Omega\to\mathbf{r}_b}$, the smallest normalized value was $4.2\cdot10^{-17}$, yielding a condition number of $C > 10^{16}$. Using the finite area operator $\mathcal{P}_{\partial\Omega\to\mathbf{r}_b\pm\rho}$, the smallest singular value computed to $1.3\cdot10^{-11}$, therefore $C > 10^{10}$, which results in an improvement of over six orders of magnitude. It actually boosts matrix conditioning enough to bring it within single floating point precision. With the interpolation operator $\mathcal{P}^i_{\partial\Omega\to\partial\Omega}$, conditioning improved slightly and the smallest singular value increased to $2.2\cdot10^{-11}$.

To conclude, an interpolation of values located on the boundary $\partial\Omega$—either by integrating over finite areas or by using interpolation function—where the boundary is discretized using finite elements, conditioning of the weight matrix will improve. It is therefore in its effects similar to a regularization of the problem. However, while this regularization might lead to faster convergence during matrix inversion—which was not examined further in this thesis—except for the reduction of boundary artifacts, it did not have a significant effect on the quality of reconstructed images.

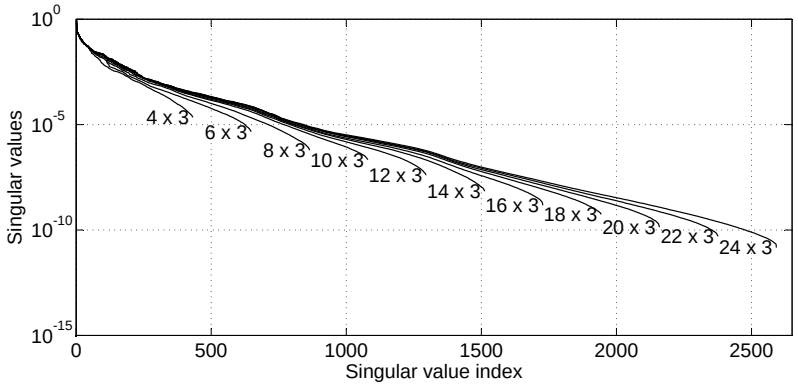


**Figure 4.22:** Plot of normalized singular values for different non-contact detector resolutions. The number of detectors is given next to each plot.

## 4.4.2. SVD Analysis of Non-Contact Weight Matrices

Non-contact weight matrices were created for a number of different detector numbers and arrangements, all spanning the same detector area but employing coarser or finer detection grids, as described in section 3.4.2. The detector grids ranged between $4 \times 3$ detector elements up to $24 \times 3$ detectors. The number of detector rows was kept constant, as the phantoms used for imaging did not exhibit variations along their vertical axis. For a number of different detector resolutions the resulting normalized singular values are plotted in figure 4.22.

In comparison to fiber-based operators, conditioning is improved again, with a minimum normalized singular value for $19 \times 3$ detectors computing to $3.4 \cdot 10^{-10}$, and so $C > 10^9$. This slight improvement of just one order of magnitude probably is not sufficient to explain the significant improvements perceivable in the reconstructed images presented in previous sections. Nevertheless it is interesting to note that an increase in detector number only slightly deteriorates conditioning but linearly increases the number of useful singular values.

## 4.4.3. Influence of Detector Numbers on Image Quality

To show the effect of an increasing number of detectors, reconstructions were performed using the experimentally acquired projection data for concentration pair B-B with non-contact weight matrices for different detector resolution as calculated in the previous section. Three exemplary images for $3 \times 3$, $9 \times 3$ and $27 \times 3$ detectors are shown in figure 4.23. For 36 source positions, these amount to 324, 972, and 2916 source / detector pairs, respectively.

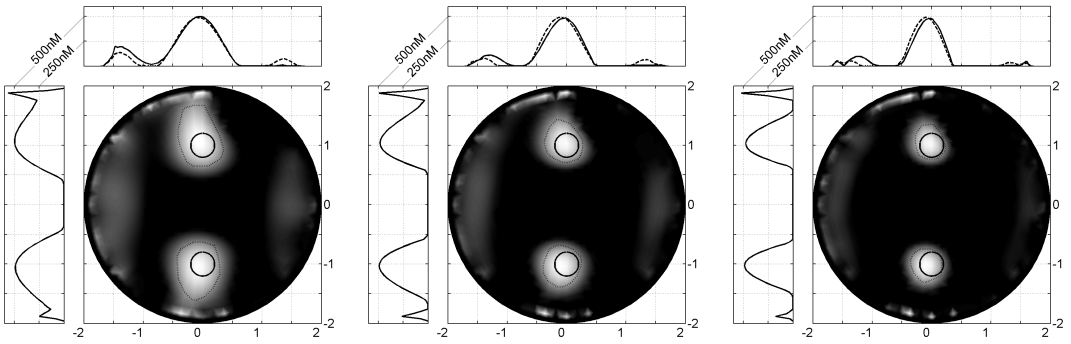


**(a)** 3 × 3 detectors **(b)** 9 × 3 detectors **(c)** 27 × 3 detectors

**Figure 4.23:** Reconstructions for different detector resolutions in the non-contact setup, using the experimental data acquired for 250nmol/l in both inclusions (36s exposure time for fluorescence imaging).

In all examples, both inclusions still appear in reconstructed image data. However, boundary artifacts improve when more detector readings become available. Resolution is also improved; the estimated horizontal diameter of the inclusions decreases from 8mm for 3 × 3 detectors (figure 4.23a), 6mm for 9 × 3 detectors (figure 4.23b), to just below 4.5mm for 27 × 3 detectors (figure 4.23c) which had already been reached for 19 × 3 detectors, as depicted in figure 4.16b.

While the resolution therefore did not increase significantly for more than 19 × 3 detectors, reconstruction quality with respect to artifacts did improve. In chapter 5, where reconstructions for nearly 7000 source / detector pairs are presented, this effect can also be observed, in conjunction with a slight improvement in resolution.

## 4.5. Discussion

Herein two different detection methods for fluorescence tomography were compared, a classical fiber-based approach (based on the $\mathcal{P}_{\partial\Omega\to\mathbf{r}_b}$, $\mathcal{P}_{\partial\Omega\to\mathbf{r}_b\pm\rho}$, or $\mathcal{P}^i_{\partial\Omega\to\partial\Omega}$ operators) and the proposed non-contact detection model, ${}^{\mathrm{L}}\mathcal{P}^i_{\partial\Omega\to\mathcal{D}}$, which was used instead of Ripoll's fiber-bundle operator ${}^{\mathrm{F}}\mathcal{P}^i_{\partial\Omega\to\mathcal{D}}$ due to the use of a wide angle lens in the experiments. Except for the detection operator used, all other parameters of the reconstruction, that is the calculated Green's functions, voxel resolution, number of sources and detectors were equivalent in according experiments. Therefore differences in the quality of reconstructed images should directly result from the change in detection methods.

In additional studies, also the number of detectors used for the non-contact model was reduced or increased to show the effect of the number of available detectors on image resolution as predicted by singular value analysis of the weight matrix.

Reconstructed images were analyzed with respect to the accuracy of estimated size, location, and fluorochrome concentration inside reconstructed inclusions. It could be shown in a series of different experiments that in all images and for all imaging methods used for reconstruction, estimated concentration values in the images increased linearly with the actual dye concentration used. However, strong differences could be observed in comparing both imaging methods with respect to the accuracy of estimated location and size of reconstructed inclusions. Clearly, in results computed from fiber-based data, inclusions appeared very close to the phantom's exterior boundary and inclusion diameters were largely overestimated by a factor of up to four in the single inclusion experiments (figure 4.11), while they behaved more or less randomly in the two inclusion data sets (figure 4.15). For non-contact data sets, size and location of the inclusions could be determined within voxel resolution in the images (4.16). Reconstructed values again scaled linearly with fluorochrome concentration.

While in both imaging methods, a linear correlation between reconstructed values and fluorochrome concentration could be observed, the spread in estimated concentration values differed significantly between the two methods (figure 4.14). It had been speculated before that non-contact detection schemes would result in an increased quality of reconstructed images simply due to the fact that higher density data sets become available [5, 39]. However, in the experiments presented, the actual numbers of detectors used in the computations was kept constant. The fact that even with the same number of detectors the concentration estimation performs better for non-contact experiments indicates an inherent superiority of non-contact detection data itself.

To find the reason of the improvement in image quality different possibly influencing factors were analyzed. A number of different calibration procedures were performed to guarantee optimal quality of fiber based detector readings: First, the exact positions of fibers in the holder were determined and showed deviations from the ideal holder model; however, this deviation did not have a significant effect on the images. Second, fiber coupling efficiencies were carefully calibrated.

It is of course possible that even the strong efforts made to properly calibrate the fiber-based setup did not suffice. Nevertheless, if this was the case, which is considered unlikely by the author, it would also clearly prove the superiority of non-contact detection, as the number and complexity of calibration procedures is significantly lower.

Additionally, there are two more possible reasons for improved image quality: the advantageous pixel value dynamics in non-contact detection, and the pixel

averaging scheme used to determine virtual detector readings. Both issues were examined in detail. Decreased dynamics turned out to have a small effect on reconstructed non-contact data: a reduction in exposure time by a factor of eight, which is equivalent to a decrease by three bits in signal-to-noise ratio, minimally distorted the shape of reconstructed inclusions, see figure 4.20f. However, the effect was not strong enough to explain the big difference between fiber-based and non-contact results.

Weight matrices were also analyzed using singular value decomposition. Singular value spectra showed a strong regularizing effect of interpolation procedures for fiber-based detector readings, but the condition numbers of non-contact matrices were only one order of magnitude lower than of their interpolated fiber-based counterparts (sections 4.4.1 and 4.4.2). One order of magnitude is in fact equal to a loss in precision by three bits; this could very well be caused by the difference in dynamics—the effect already discussed.

The second possible issue, pixel averaging, was examined by only using single pixels as detector values. Averaging schemes had a significant effect on quantification: using only single pixel readouts caused a large spread in estimated concentration values. In fact, the deviations observed were similar to the ones seen in fiber-based data sets, see figure 4.17b. The observed deterioration of quantification accuracy went along with a decrease in image resolution / image quality, as demonstrated in figure 4.17a. However, again the decrease in image quality could not fully explain the difference between images reconstructed using both detection methods, fiber-based and non-contact.

Summarizing, the difference in dynamics as well as pixel averaging schemes introduced for non-contact imaging increased the quality and accuracy of reconstructed data sets. As none of these influencing factors themselves suffice to explain the differences observed between fiber-based and non-contact reconstructions it is very probable that multiple factors influenced reconstruction quality, e.g., dynamics, pixel averaging, as well as possibly unresolved fiber-coupling issues.

The results presented herein prove that non-contact detection is a suitable tool for quantitative FMT reconstructions. A larger amount of available measurement data as well as the non-contact detection scheme itself improve image quality and resolution. The non-contact setup with both free-space sources and free-space detectors clearly shows the simplification of optical setups by the absence of fibers.

To the best of the author's knowledge, this is the first direct comparison of fiber-based and non-contact fluorescence tomography of turbid media. While the simplicity of the non-contact experimental setup is obvious, results indicate that non-contact imaging can significantly improve image quality using the same number of source / detector pairs, without increasing the complexity of the inverse problem. Thus far, the possible increase in the number of detectors has been the major

argument in favor of non-contact detection [5]. An improvement due to the detection method itself, however, is a stronger advantage, as neither computational effort nor memory requirements are increased.

Concerning the spatial resolution of the setup presented herein, it must be noted that the determination of the available spatial resolution of any optical tomographic setup is a more difficult task than for other imaging modalities. Due to the scattering, achievable resolution strongly depends on the depth of an inclusion [76]. Furthermore, in experiments it also depends on the number of distinct inclusions and on their concentration as this influences the magnitude of the perturbation from the homogeneous diffusion equation, see chapter 2.3.1. For the relatively simple phantoms used herein, spatial resolution can only be roughly estimated, as the two inclusions are far apart and large in diameter. Nevertheless, it is still possible to compare the quality of reconstructions between results obtained with fiber-based measurements and results obtained through the non-contact setup with respect to the estimated diameter and localization of the inclusion.

Judging from the full width at half maximum size of the reconstructed inclusions and the localization accuracy charts in figure 4.16 the spatial resolution of the non-contact system presented herein should be in the order of 1mm, as previously reported for other FMT systems [39]. However, this value ranges in the order of the voxel size employed for reconstruction; thus, more detailed work on resolution would have to be performed to determine the actual resolution of the system. However, the topic of this work was a comparison between fiber-based and non-contact detection operator efficiencies, as measured by an increase in resolution and accuracy of quantification.

# Chapter 5.

# Tomographic Imaging System

Una cosa sana no respira*

*(Antonio Porchia, Voces)*

## 5.1. Overview

CHAPTER 4 contained an experimental demonstration of how non-contact detection can improve the quality of reconstructed data sets while at the same time offering a method of data acquisition being easy to calibrate and to use. Starting from these results it was aimed at developing a fully non-contact tomography system for small animal imaging, with "fully non-contact" meaning that both, sources and detectors, would be located in free space, which was also the case in the experiments described in the previous chapter.

Existing publications have provided a proof-of-principle for non-contact detection, but the prototype systems used therein were not designed to acquire data from 360° of view [4, 5] (see also figure 5.1). Furthermore, sources were not located in free space but on a rectangular grid of fibers mounted on a plate opposite the detecting camera, similar to the plate used for fiber-based imaging described in the last chapter. Imaged animals needed to be compressed against this source plate to guarantee good source coupling. Compression, however, changes the animal's morphology and blood flow and thus might compromise the results obtained.

Also, the setup could neither be rotated around the animal, nor could the animal be rotated, so that projection angles available were restricted to angles in the order of 120° [39]. The fact that the animal had to be placed on a rectangular grid of fibers additionally decreased the number of usable sources, as for lateral sources only a thin layer of skin was located above the source. This fact caused saturation of projection images acquired for lateral sources, leaving the projection images to be unusable. Consequently, these saturated projection images had to be discarded in

* "Nothing that is complete breathes."

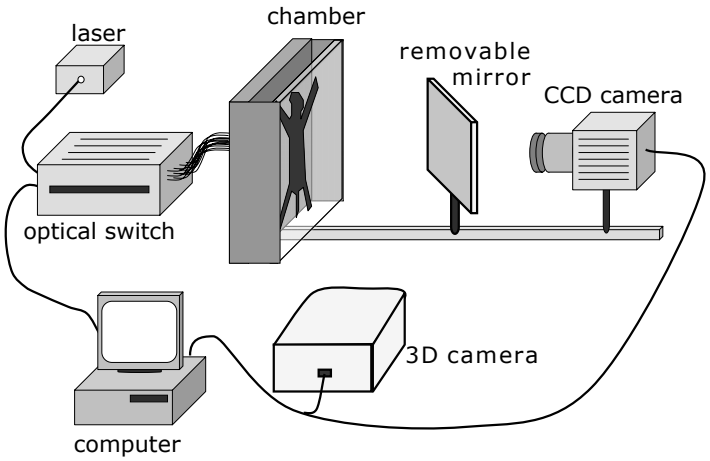


**Figure 5.1:** Experimental setup used in a previously published proof-of-principle for non-contact tomography, taken from [5].

the reconstruction process [5], decreasing the number of available source positions and thus possibly leading to lower resolution images.

Problems of saturation as described above can possible be resolved by using a setup similar to the one described in chapter 4. There, a free laser beam source—directed toward the object's main axis and having an incidence angle perpendicular to the object's exterior boundary—was used to excite fluorochromes within. Different source positions were obtained by rotating the object. The points of incidence, i.e., the source positions, were therefore always located centrally on the object or animal. Thus, it should be possible to obtain useful, non-saturated images for any source position, as long as the imaged object is reasonably cylinder-like, i.e., reasonably rotation-symmetric.

In addition to the setup described in the previous chapter, a laser diode source could be mounted movable along the object's main axis to create different axial source locations per rotational position; an aspect that had been of no importance previously as imaged phantoms were invariant along their main axis.

## 5.2. Device Layout

### 5.2.1. Objectives

In summary, the following objectives were considered important in the development of the tomographic imaging device:

- **Fully non-contact design with flexible source positioning**
  360° angular field of view and an axially movable laser source should enable the acquisition of diffuse projection images of the object or animal from all sides using arbitrarily positioned laser excitation. The laser source should be mounted perpendicular to the object's main axis to guarantee all source positions to be usable, i.e., not lead to saturation of CCD images.
- **Rotation of the scanner, not of the object / animal**
  Rotating the object or animal instead of the entire imaging device is often considered easier, as the objects or animals imaged are usually less heavy than the instrumentation. However, rotating an animal without changing its shape is difficult. Furthermore, for optical tomography, animals cannot be mounted in any kind of translucent holder due to the creation of disturbing reflections or even autofluorescence—most plastics exhibit fluorescence in the near-infrared part of the spectrum. Additionally, moving / rotating the animal changes the blood distribution of the animal, prohibiting the potential use of the system in pharmacokinetic studies.
- **Integrated scanning system for surface capturing**
  As discussed before, in chapter 2, implementation of correct boundary conditions is important to correctly calculate the theoretical model of photon propagation. For a non-contact system, accurate acquisition of the animal's outer shape thus is vital, as the exterior surface will determine the imaging domain's shape. To determine these boundaries, a method of surface capture had to be implemented, preferably a simple method that would not require the use of additional 3D scanning equipment.
- **Possibility of long-term animal studies**
  In previous FMT imaging studies, animals were subcutaneously injected with anesthetics [5, 40, 67]. This type of anesthesia, however, enables imaging a nude mouse for only about half an hour without the risk of accidentally sacrificing the animal. Furthermore, animals develop a tolerance with respect to the used anesthetics, complicating repeated imaging. At DKFZ, for animal studies usually gas anesthesia is performed (using Isoflurane), which is considered safer and more reliable. Thus, the imaging system should be equipped with appropriate animal handling and anesthesia devices.

Starting from the list of objectives as given above, a tomographic imaging system consisting of a rotating, light-tight imaging chamber and a control unit was developed (figure 5.2), which is in detail described in the following sections. At first, the system's central unit—called the imaging chamber—will be introduced, followed by the embedded control system and the animal handling unit. Consecutively, surface

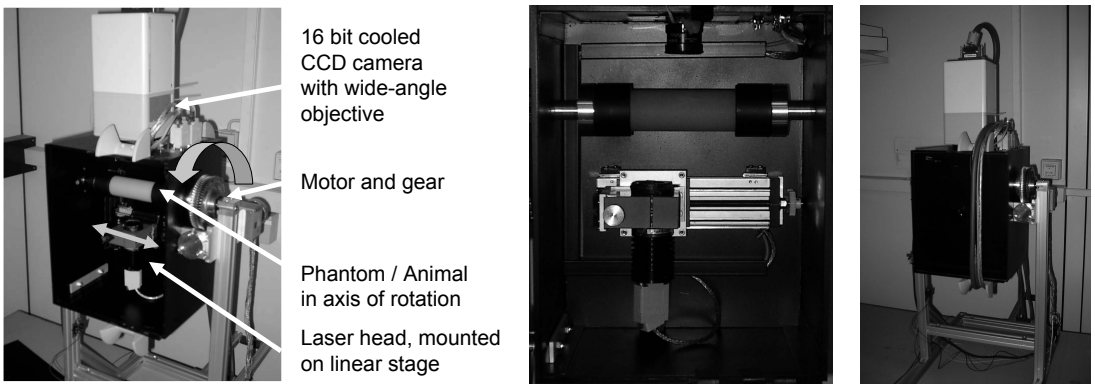


**Figure 5.2:** Picture of the tomography system (a) with opened imaging chamber in initial position and (c) with closed imaging chamber after a full rotation, with the data cables wrapped around the chamber. (b) is a detailed frontal view of the chamber's interior.

capture algorithms and data acquisition procedures are described. Finally, experimental results will be presented.

## 5.2.2. Imaging Chamber

The central unit of the system is a light tight imaging chamber (figure 5.2a), containing a cooled CCD camera (ORCA-II, 512x512 Pixels, 16bit dynamic resolution, Hamamatsu Photonics, Japan) and a collimated, temperature stabilized diode laser source, emitting at 670nm (LG LaserTechnologies, Kleinostheim, Germany) which is mounted on a linear stage (figure 5.2b). The CCD camera is used in conjunction with a wide angle, large aperture objective (NA1.4, SchneiderKreuznach, Germany) which enables imaging of the whole object or animal (max. 10cm axial extension) at a distance of 6cm.

The imaging chamber is mounted between two supporting posts. From each post aluminum rods of 15mm diameter reach into the chamber, around which the chamber can rotate. The rods itself do not move or rotate and thus provide a stationary mount for anything inside the imaging chamber. The rear ends of the rods provide a 10mm thread (M10) to enable mounting any kind of object holder on the axis of rotation. For the cylindrical phantoms used in experiments described later on, holders consisted of two cylindrical parts extending the mounting rods enough to only leave 10cm of space, in which the phantom could be squeezed in fixed position. Phantom holders can be replaced by an animal handling system to support

small animal imaging, see section 5.2.4 and figure 5.5. To allow inflow of anesthesia gas, one of the mounting rods had a hollow center (∅5mm).

Chamber rotation is driven by a 1.8° stepping motor with a gear of 1:3750. It is mounted on the chamber's right mounting post, as depicted in figure 5.2a. Position control is performed using a quadrature encoder with 5000 lines, mounted to the other post with a gear of 1:2. As for each line of the encoder 4 flanks are produced within the readout electronics, over a full 360° movement 40,000 trigger flanks are created. Thus, the angle of rotation can be determined with an accuracy of better than 0.01°.

The minimum and maximum angular positions which are accessible by chamber rotation are determined by two end switches located below the quadrature encoder on the mounting post. These switches are activated by a small aluminum rod mounted on the imaging chamber. They are also used to calibrate the chamber's rotational position during controller initialization as well as provide the controller with a "stop" signal. As they are used as inputs for the software environment controlling stepping motor movements, additional "emergency" end switches are also mounted on the post. These additional switches will be activated later than the normal end switches and which will deactivate the stepping motor and controller system by hardware, i.e., will shut off motor power, to prevent mechanical damage to chamber, mounting posts, or data cables. Power can only be manually reactivated.

In total, a 355° rotation of the chamber is possible[†]. During rotation, all data and control cables mounted to the chamber are wrapped around the chamber (figure 5.2c). The cables consist of power and data cables of the CCD camera, power supply of the laser, as well as control cables for the linear stage, stepper motor, and I/O ports. A detailed pinout of the proprietary cables used can be found in appendix A.1, page 115. The chamber's front plate can be removed to allow access to the interior, i.e., access to the laser source, the imaged object or animal, and the objective lens of the camera to bring the system into focus or mount optical filters.

The linear stage on which the laser source is mounted allows for an axial movement of ±5cm driven by a 12V direct current motor. Its position is controlled by a potentiometer mounted to the linear axis which provides a positional signal through voltage division. The position is sampled using the internal analog-digital-converter of the micro-controller (10bit sampling precision), resulting in a possible resolution of 0.1mm, i.e., 1024 steps on a range of 10cm. Again, axial stopping positions are determined using two end switches.

Illumination inside the chamber is provided by a white electroluminescent foil (Lumitech, Jennersdorf, Austria) which can be switched on for bright light imag-

[†]around 5° total are used as a safety interval between activation of end switches and emergency switches

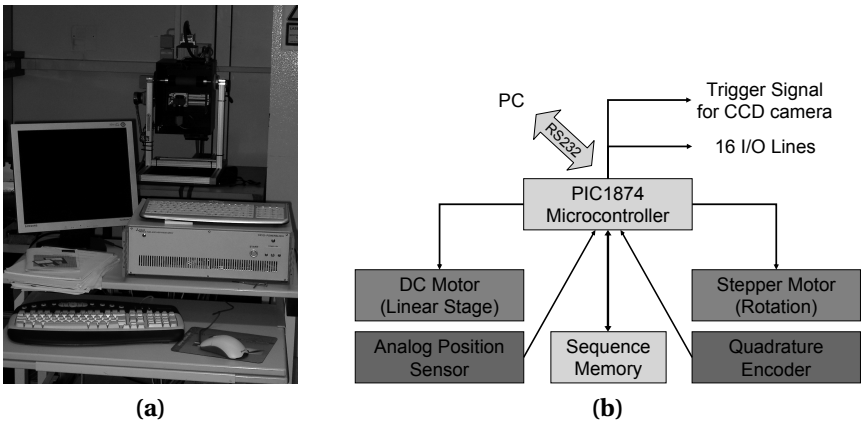


**Figure 5.3:** (a) Image of the controller system with tomographic imaging chamber visible in the background. (b) Schematic drawing of the control unit.

ing and off for transillumination imaging. The luminescence output of the foil employed is strong enough for the sensitive CCD camera used. As this camera employs a relatively slow mechanical shutter, the minimum exposure time is 0.1s. Using the minimal exposure time for bright light images results in an average count value of 5,000 for object pixels and 500 for background pixels, i.e., signal from the black walls of the chamber. For irregularly shaped objects or for objects of unknown geometry, e.g., when imaging small animals, acquired white light images are used to control subject placement and to estimate the object geometry, as described in section 5.3.

### 5.2.3. Control Unit

Control of all rotational and linear movements, the quadrature encoder and end switches is performed through a proprietary controller system. The controller is based on an autonomous microcontroller (PIC18, Microchip Technology Inc., Chandler, Arizona, USA) with 64kB of flash EEPROM and another 64kB of RAM. This controller provides pulse-width modulation (PWM) signals for optimal control of the DC motor, 10bit analog inputs for the linear axis potentiometer, stepper motor control, digital inputs for the quadrature signal and end switches as well as digital outputs to control the illumination and trigger the camera exposure. A schematic drawing of the controller system components is provided in figure 5.3.

A software environment was developed for the micro-controller system to load and autonomously run imaging sequences without further control by a personal computer. A Pentium-based PC is used only for image acquisition through the FireWire interface of the CCD camera, and to load a complete imaging sequence into

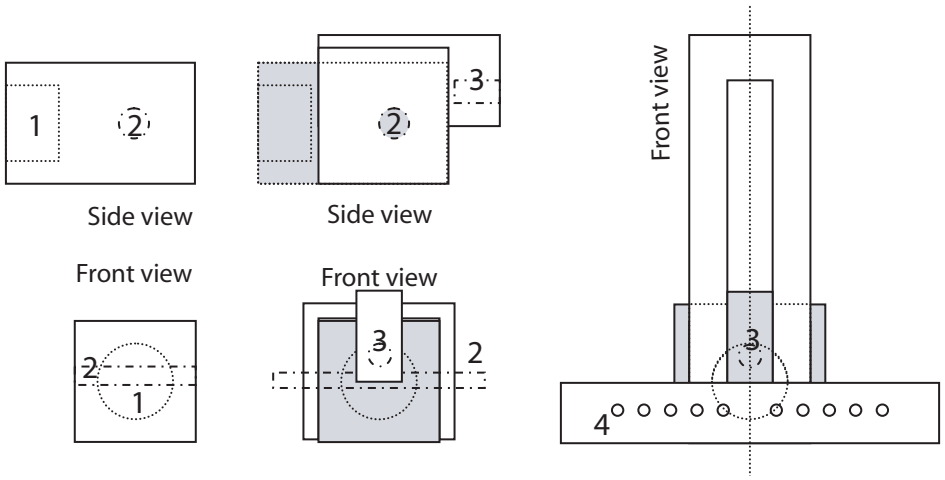


**(a)** Cuboid mount **(b)** Intermediate part **(c)** Main holder

**Figure 5.4:** Schematic drawing of the lateral holders of the animal handling unit in actual dimensions. (a) Cuboid mount that is fixed inside the chamber on the M10 thread provided by the rear end of the chamber's mounting rods (part <1>). (b) Intermediate part to be fixed on the cuboid by use of a split pin (denoted by a small dashed circle / rectangle, part <2>). The cuboid itself is shown in gray. (c) Actual holder, which can slide up and down while fixed on the intermediate part through use of a fixing scre (part <3>). The holder provides several mounting holes (part <4>) for the carbon rods on which the animal is placed.

the controller system memory. Programming of the controller is performed through a standard serial interface.

A list of commands supported by the embedded control system is given in appendix A.2 on page 117. An example on how to program the controller is presented in A.3.

### 5.2.4. Animal Handling

The animal handling unit, used for small animal imaging, was developed to fulfill the following requirements:

- The unit should provide an optimal view of the animal without enclosing the animal in any material, whether transparent or opaque. This should enable optimal use of the field of view without introducing reflections or blocking too many possible source positions.

- The animal should not have to be fixed in any way to the handling unit, simplifying image acquisition. For optimal sedation of animals the unit should provide gas anesthesia.
- The unit should be adjustable to accommodate different animal sizes, especially for imaging of mice and rats.

Starting from these prerequisites, an animal unit was developed that primarily consists of two black carbon rods of 2mm diameter. On these rods, an animal can be placed. The rods are mounted in two holders, which are in turn mounted to the M10 threads provided on the axis of rotation inside the chamber. The two lateral holders consist of three parts: First, a cuboidal element (figure 5.4a) which is screwed onto the M10 thread inside the chamber. In the figure, the M10 thread is denoted by a circle. Both cuboidal elements remain inside the chamber and allow in principle to mount different holding devices. The cuboids are used to fix horizontal and vertical axis of the holder.

The second part exactly matches the cuboid geometry (figure 5.4b) and can be fixed on the first element using a split pin. In the figure, the hole for the split pin is denoted by a small circle. This second part features a rectangular bit which allows the third part of the holding device to slide up and down (figure 5.4c).

The third part is fixed on the second by use of a set screw which allows the third part to be mounted at any vertical position. This allows for height adjustment of the animal handling unit so that animals can always be centered in the axis of rotation. The third part also contains a number of mounting holes in which the two carbon rods can be placed.

The distance between the carbon rods can be adjusted between 7mm and 35mm in 7mm increments. For mouse imaging as presented in this chapter, the distance was set to 14mm.

The two carbon rods are black and thus only minimally disturb acquired images. When the rods are visible in the images, obviously pixels belonging to the imaged rods must be discarded in the reconstruction process, as they do not contain any useful information. Additionally, all rotational positions where the beam of the laser source hits one of the rods have to be exempt from image acquisition. For a measurement with 3° stepping, where for each step an image was acquired, three images had to be discarded for each rod, equivalent to a stepping angle of 12°.

To provide gas anesthesia, the tip of a plastic syringe is used as a mask to cover the animal's nostrils. It is connected to a small flexible plastic tube of 4mm diameter through which a mixture of anesthetic gas and air is flowing. The flexible tube enters the imaging chamber through the hollow mounting rod, as described above, which provides an opening of 5mm diameter reaching through the full rod. The cuboids (figure 5.4a) also contain an open channel leading from the end of the M10 thread

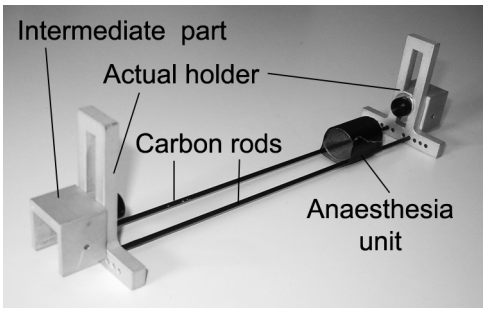


**(a)**

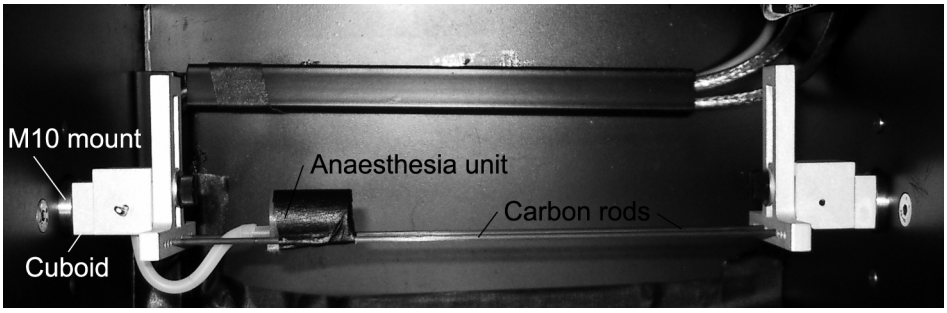


**(b)**

**Figure 5.5:** Photographs of the animal handling unit. (a) Unmounted handling unit. (b) Handling unit mounted inside the chamber, with the gas anesthesia unit connected.

to the lower side of the cuboid. Here, the flexible tube finally enters the imaging chamber.

As the second part of the animal unit (figure 5.4b) covers only the cuboid's top and lateral sides, but not its bottom side, this does not interfere with the gas anesthesia system; the whole handling unit—with exception of the two cuboids fixed to the chamber's mounting rods—can be removed and inserted without disturbing the anesthesia system.

The animal handling unit is mounted or unmounted by inserting / removing the split pins and (dis-)connecting the anesthesia mask. Photographs of the handling unit are depicted in figure 5.5, the unmounted unit as well as the unit as mounted inside the chamber with the anesthesia system connected.

### 5.2.5. Data Acquisition

This section describes all procedures necessary to acquire a full data set which can be fed into the reconstruction algorithm. Prior to imaging, a sequence of movements or other commands is uploaded to the controller using the `PS`–`PE` commands (for a list of available commands, see appendix A.2, page 117). As soon as execution

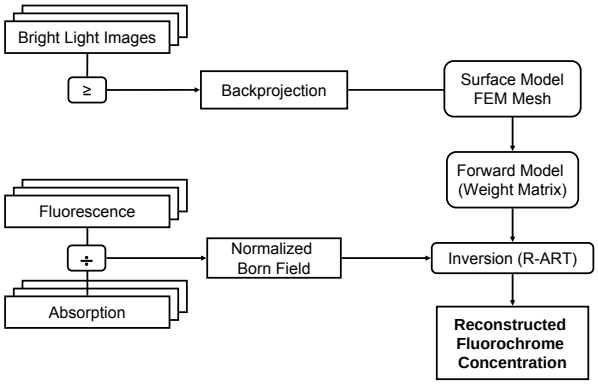


**Figure 5.6:** Data flow diagram, showing the types of acquired images and necessary computation steps for reconstruction. Symbol ≥ is used to denote the application of a threshold.

of this sequence is started using a RP command, the PC only needs to wait for and subsequently store image data acquired by the CCD camera. Image acquisition is in turn automatically triggered by the controller program. An example of a controller sequence is given in appendix A.3, which is also part of the sequence used to acquire the experimental data presented in this chapter.

Imaging procedures themselves involve placing the object or animal inside the chamber and then obtaining a sequence of front-illumination "photographic" (bright light) images at different angles. These images are used to verify the subject's position on the holder and to extract the three-dimensional boundaries of the subject. For the latter, acquired bright-light images are converted into black / white (b/w) images by applying a threshold, which are consecutively used in a standard back projection algorithm to reconstruct the object's volume. The resulting surface description is used to generate a FEM mesh, on which the according Green's functions are calculated. The latter are then used to set up the weight matrix. The procedure of boundary extraction is described in detail in section 5.3.1.

Tomographic data acquisition subsequently employs capturing a number of diffuse projection images at different angular positions and / or axial laser positions. Either the already loaded imaging sequence can be used, or a new one could be loaded into the controller system. For each position, two images have to be obtained, one with a fluorescence filter in front of the objective lens ("fluorescence image") and one without filtering ("absorption image"). Each pair of images is used to gain normalized projection data dividing the fluorescence image by the corresponding absorption image. The resulting data yields the left hand side vector of the weight matrix equation (2.25) used in the matrix inversion equation (2.26), which

results in the 3D distribution of fluorochrome concentration. A flow chart of the acquisition and reconstruction process is presented in figure 5.6.

For fluorescence imaging, a combination of two longpass glass filters with limit wavelengths 695nm and 715nm was used (colored glasses RG695 and RG715, Schott AG, Mainz, Germany), as previously described and characterized in section 4.2.2. The filters have to be mounted manually, as the imaging system does not yet provide an automatic filter changing wheel. Therefore, instead of acquiring two images after one another at each rotational position, two complete imaging sequences are run consecutively, so that the filters had to mounted only once.

## 5.3. Boundary Capture and FEM Mesh Generation

The subject's outer boundaries have to be captured, as described before. Consecutively, an according FEM-mesh needs to be generated. This allows for a correct calculation of necessary Green's functions, which require precise boundary conditions. Mesh generation from acquired boundary images consists of the following steps which will be described below in detail:

1. **White-light image acquisition**
   As mentioned before, this is performed using the EL-foil as a light source.
2. **Application of threshold**
   Acquired images are converted to b/w images by applying a threshold and consecutive morphing operators, if any. Those morphing operations should remove unconnected islands of pixels, and also smooth edges a bit, see 5.3.1.
3. **Back projection (inverse Radon transform)**
   In this step, the b/w images are projected back into a 3D data volume according to a cone beam projection. All projections are added up, where pixels that belong to the object have a value of 1, and background pixels have a value of 0. After this step, the actual 3D volume consists of the subset of voxels with a value equal to the number of available projections, see 5.3.1.
4. **Isosurface extraction**
   The discriminating surface between voxels that belong to the object's volume and voxels outside the object has to be extracted, see 5.3.1.
5. **Grid transformation**
   In this last step, a cylindrical grid is smoothly transformed to the shape of the extracted surface. A cylindrical base grid is chosen as objects are expected to be nearly cylindrical. Points are not translated axially, but only radially, thus simplifying the transformation; see section 5.3.2.

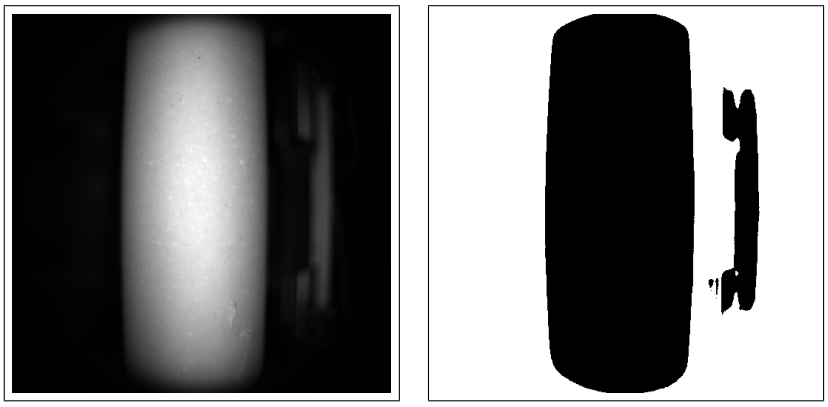

**(a)** **(b)**

**Figure 5.7:** (a) Bright light images for surface acquisition and (b) corresponding b/w image obtained by applying a threshold of 3000 counts. The artifact on the right hand side is a reflection caused by the linear stage.

### 5.3.1. Boundary Capture and Isosurface extraction

As laid out before, the outer boundaries of the object or animal under investigation are estimated by first acquiring bright light images from a number of different rotational positions. These images are converted to b/w images by applying a threshold to separate object from background. As the background intensity ranged around 500 counts for each pixel, while objects were recorded with an intensity of around 5000 counts, object and background can be clearly separated. For the experiments described herein, a threshold of 3000 counts was used. This step is depicted in figure 5.7 for a cylindrical phantom.

A standard back projection algorithm (inverse Radon transform) could then be used to determine the three-dimensional object volume. The object's surface can then be extracted from the volume using a marching cubes algorithm [58]. However, due to the imaging characteristics of the wide-angle lens employed, rather a cone-beam algorithm should be used. This can be seen in the boundaries of the phantom in figure 5.7b which are not parallel but bended due to the fish-eye effect, as induced by the wide angle lens. An exemplary result showing the extracted surface of a mouse is given in figure 5.8.

For each voxel position $\mathbf{r} = (x, y, z)$, where $z$ is the chamber's axis of rotation and the animal's main axis, and each projection angle $\alpha$, the corresponding image position $\mathbf{r}' = (u, v)$, where again $v$ is the axis of rotation, is given by

$$\mathbf{r}' = s(\mathbf{r}, \mathbf{r}_p) \begin{pmatrix} x \sin\alpha - y \cos\alpha \\ z \end{pmatrix}. \tag{5.1}$$

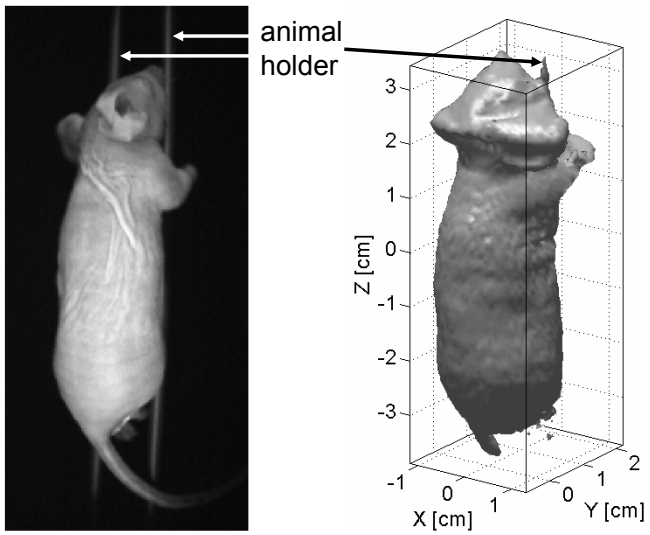


**Figure 5.8:** Bright light image of a nude mouse held in the scanner (left), and rendering of the according surface (right).

In equation (5.1) it is assumed that the image center is located at $(0,0)$, and that the 3D volume's origin is located in the center of the axis of rotation. Function $s(\mathbf{r},\mathbf{r}_p)$ provides a scaling factor depending on the opening angle of the cone and the position $\mathbf{r}_p$ of the lens modeling pinhole (please refer to section 3.4.2); if the fish-eye effect is to be ignored, then $s = 1$.

The artifact on the right hand sides of the images in figure 5.7 are reflections from the laser's linear stage. While these can be removed from the b/w images by using simple segmentation algorithms, they were also experimentally eliminated by fixing a black, strongly absorbing sheet of cardboard in front of the stage for all subsequent experiments.

Projection equation (5.1) is used to project every single b/w image of the object's outline onto the 3D volume. These projections, where a value of 1 is assigned to all object pixels, and 0 to all background pixels, are then added up. In the case of the experiments performed herein, 118 projection images were available. Therefore, all voxels reaching the value 118 belong to the object's volume, as for these voxels in every projection the corresponding pixel belonged to the object.

In practice, however, smoother results are obtained when accepting that not in every projection image the object's boundaries can clearly be identified because of pixel noise. Additionally, the animal handling system described before consists of two black rods that will show up as background in the b/w images. As described before, for 3° angular stepping, each rod appears on a single pixel in about 3 projec-

tion images. Thus, having two rods, for each voxel it must be accepted that about 6 projections might show corresponding voxels to belong to background instead of the object / animal. Therefore, a safety margin of 10 projections was considered for surface extraction. The object's surface was thus defined as the isosurface at value 110, i.e., the surface between voxels of values $\leq 110$ and voxels $> 110$. The surface was extracted using the marching cubes algorithm [58].

Surface extraction results of animal experiments performed in the aforementioned way are given in figure 5.8, where the bright light image as well as a 3D rendering of the final surface from approximately the same projection angle are depicted. It has to be noted that complex, non-convex body parts, e.g., ears and paws, cannot be extracted properly. However, due to the small dimensions of these extremities—this is especially true for the ears—diffusion modeling of light transport is not valid in these regions. The body parts concerned thus have to excluded from imaging. It is also worth noting that, although the holding carbon rods appear mostly as background in the images, there are also sometimes specular reflections appearing on them. As can be also seen in figure 5.8, this leads to the appearance of the rods in some surface regions.

For tomographic imaging of the abdominal region, the insufficient surface extraction of ears and paws will not be a problem as only a small portion of the surface is considered for mesh generation, and thus cranial body parts are simply not taken into account. However, for tomographic imaging of he head, these body parts will create a lot of difficulties. To work around insufficient surface extraction concerning the paws, they have to be fixed against the body, i.e., put between holding rod and animal body, as performed for the experiments shown later on. Concerning the ears, they could either be removed, or be taped onto the head using white tissue tape (translucent tape would create specular reflections, while white tissue tape will just diffuse the light a bit). More experiments are needed to examine this problem in detail, however.

### 5.3.2. FEM Mesh Generation

After isosurface extraction, i.e., after defining the domain boundary $\partial\Omega$, a mesh of non-degenerate cells needs to be created to fill up the interior volume $\Omega$. This mesh is then be used to set up a FEM system for calculation of according Green's functions. As all the objects of interest—either phantoms or small animals, and for small animals especially the abdominal region—are of nearly cylindrical shape, it was chosen to smoothly transform a regular cylindrical grid to fit the acquired boundary shape instead of creating a grid from scratch.

The smooth transformation is performed by starting with a cylindrical grid of very small radius but sufficient axial length which needs to be radially expanded and

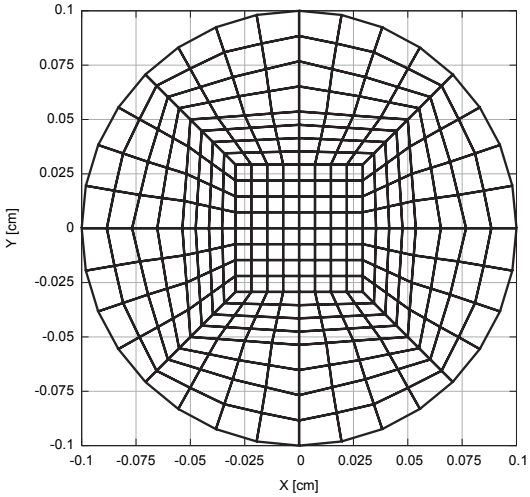


**(a)** Central transversal slice of the original cylindrical grid

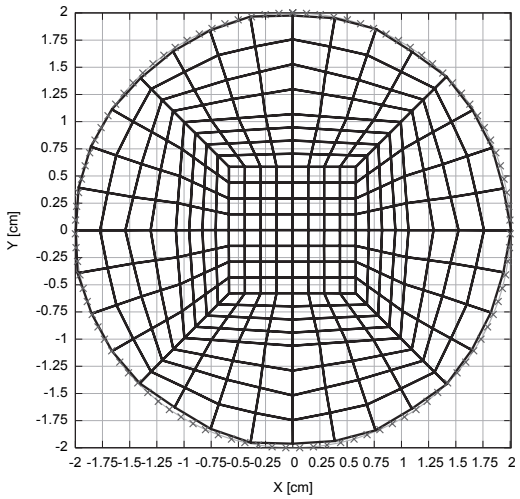


**(b)** Transformation to the surface of a cylindrical phantom placed in the imaging system

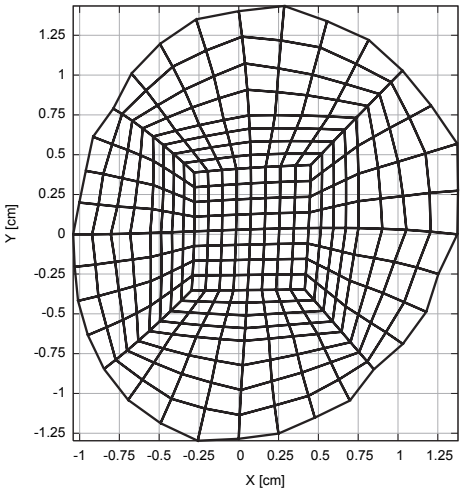


**(c)** Transformation to the surface of a living mouse placed in the imaging system

**Figure 5.9:** Transformation of an originally cylindrical grid to the acquired surface model, either phantom or living mouse. In (b), the actual outline of the phantom of 4cm diameter is depicted by crosses.

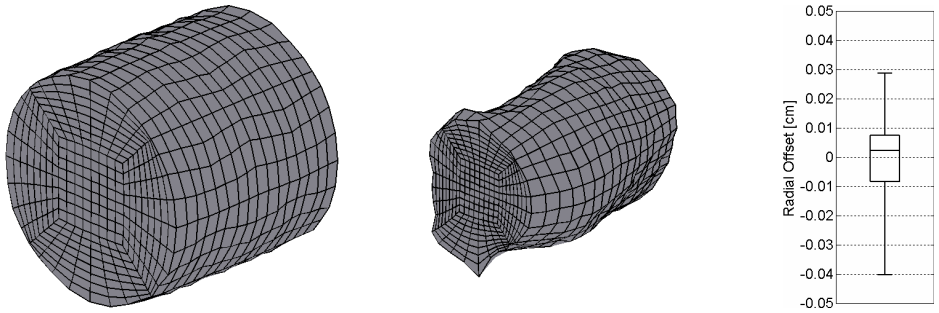


**(a)** **(b)** **(c)**

**Figure 5.10:** Experimentally acquired grids. (a) Rendering of the experimentally acquired cylindrical grid. (b) Rendering of the grid created in an animal experiment, where a nude mouse was imaged. (c) Accuracy of the acquired cylindrical grid, measured as the radial distance between boundary mesh vertices and actual surface. The box marks lower, middle, and upper quartile. Whiskers span the whole range of observed values.

fit to the actual surface. An initial radius of 1mm was chosen for the experiments described herein. The cylinder's height was set to be 4cm.

For each mesh vertex located on the boundary, a translation vector $(\Delta x, \Delta y)$ needs to be determined which will move the vertex radially outward and place it on the extracted object surface. Following this simple first step, smooth translation vectors for each interior vortex have to be computed as well. This smooth transformation is performed by solving two consecutive boundary value problems for the Laplace equation, $\nabla^2 u_{x/y} = 0$. As boundary values, translation distances $\Delta x$ and $\Delta y$ are used for $u_x$ and $u_y$, respectively. This equation using a Dirichlet boundary condition is the mathematical model for the deformation of an elastic surface when forced to a given shape.

The computed offsets $u_x$ and $u_y$ as resulting from the FEM system are then applied to each mesh vertex. Please note that due to the assumption of a nearly cylindrical domain shape, no translation in $z$-direction, i.e., axial direction, is necessary. The mesh transformation is also illustrated in figure 5.9 which depicts the central transversal slice of the original mesh, an experimentally acquired mesh of a cylindrical phantom (∅4cm) as well as the mesh acquired by imaging a nude mouse. Renderings of the complete three-dimensional meshes are given in figure 5.10.

To assess the accuracy of the mesh generation method, the generated cylindrical grid describing the phantom was compared against the actual geometry. This was performed by determining the radial distance between each boundary vortex of the generated grid and the expected radial position of 2cm. The distribution of

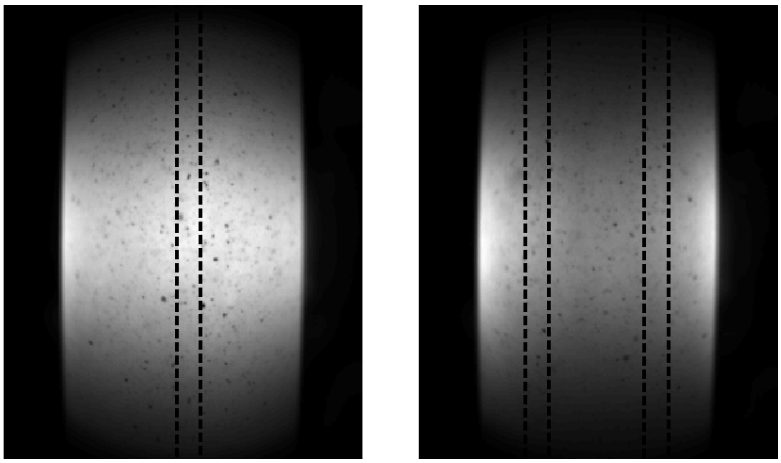

**(a)** **(b)**

**Figure 5.11:** Two exemplary projection images of fluorescence to show the diffusivity of a cylindrical phantom. Dotted lines show the inclusions positions in these projections, taken at (a) 0° and (b) 90°.

these deviations is shown in a box-whisker plot in figure 5.10c. The mean deviation is well below 0.1mm, the maximum deviation is at 0.4mm.

## 5.4. Results from Tomographic Imaging

### 5.4.1. Two-Inclusion Phantom

In a first experiment, imaging was performed on a diffuse phantom of 10cm length and 4cm diameter having two fluorescent inclusions; the same phantom as used in chapter 4. Both inclusions were filled with a Cy5.5 dilution of 388nmol/l concentration. The controller system was programmed to acquire 118 projections at 3° angular stepping. All source positions were located in the same plane, thus the linear stage was not employed for this experiment. The acquisition sequence was run three times to acquire white light, absorption, and emission images as described before.

A suitable mesh for the imaged phantom was generated from white light images as described in section 5.3. The generated mesh is depicted in figure 5.10a; for better source modeling, the grid was post processed by refining it further on the boundary (not shown in the figure). Subsequently, Green's functions were calculated accordingly for all 118 source positions and all mesh points as described in section 2.4.2. In total, 33,000 degrees of freedom were used for reconstructing fluorochrome

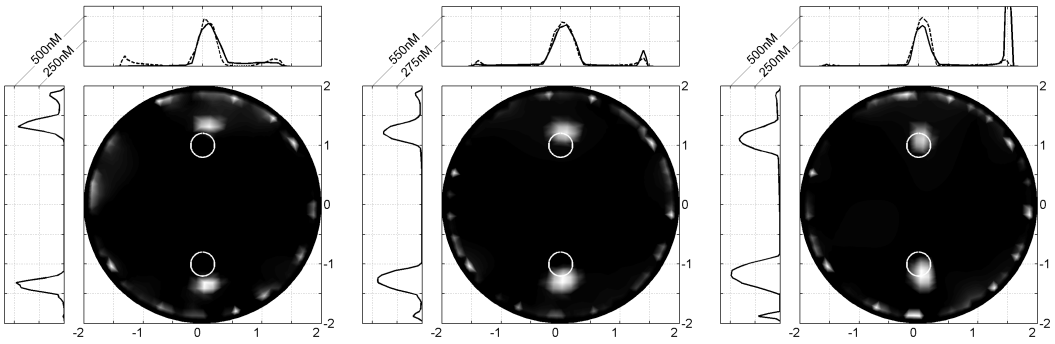


**(a)** 4cm distance **(b)** 5cm distance **(c)** 6cm distance

**Figure 5.12:** Central transversal slice of the reconstructed data set. Circles denote the actual positions where inclusions are located.

concentrations. Matrix inversion employed 50 r-ART iterations with a relaxation of $\varrho = 0.1$, the same parameters used in the experiments described in chapter 4.

Exemplary planar projection images of fluorescence emission are depicted in figure 5.11 for two rotational positions, at 0°, where both inclusions are in line with the camera, and at 90°. The actual outlines of the inclusions are indicated by dashed lines in the figure.

Detection was modeled using the lens based operator ${}^{\mathrm{L}}\mathcal{P}^{i}_{\partial\Omega\to\mathcal{D}}$ (please refer to section 3.4.2). The position of the pinhole needed to model the lens was determined to be located at 6cm distance from the axis of rotation. To demonstrate the effects caused by erroneous pinhole positions, reconstructions were performed additionally for pinhole distances of 4cm and 5cm.

Results are presented in figure 5.12. In all cases, both inclusions are well resolved and show the same intensity values, as seen in the profiles next to each reconstructed slice. Estimated shape and location of inclusions in the reconstructed images strongly depended on the pinhole position used in the detection operator. For underestimated pinhole positions, reconstructed inclusions moved toward the outer boundaries of the domain, figures 5.12a and 5.12b. Furthermore, especially in the 4cm case, boundary artifacts become significantly stronger, indicating inconsistencies in the linear system used.

## 5.4.2. Subcutaneously Implanted Emitters in a Living Mouse

In a second series of experiments, two plastic pipette tips of 2mm diameter and 2cm length were subcutaneously implanted in a nude mouse. Prior to surgery, mice were anesthetized with isoflurane and kept under anesthesia until the end of the exper-

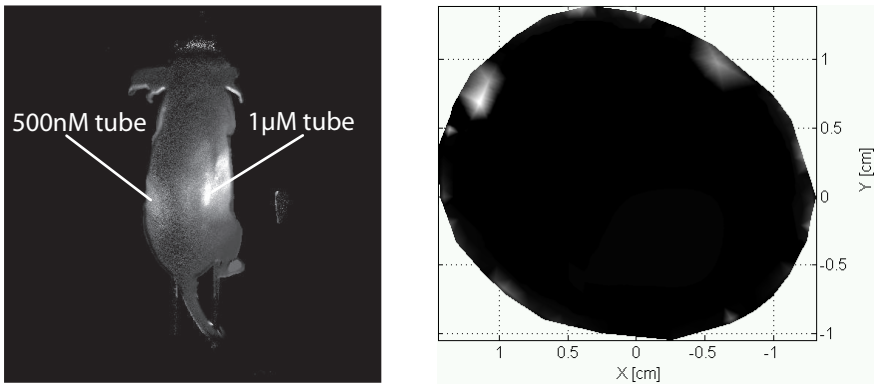


**(a)** **(b)**

**Figure 5.13:** Tomographic data of an animal experiment. (a) Normalized Born data of the mouse in one projection. The appearance of both emitting tubes is denoted in the image. (b) Slice of the reconstructed data set in which both tubes appear.

iments. Animals were sacrificed after the experiments. Treatment of animals was performed according to the ethical guidelines and standards at DKFZ.

Prior to implantation, pipette tips were filled with a 500nmol/l and 1000nmol/l solution of Cy5.5 dye, respectively. Exposure times were set to 100ms for white light and absorption images, and 15s for fluorescence emission images. A normalized projection image after subtraction of background and leaking excitation light is depicted in figure 5.13a. Signal from both tubes appear in this projection; however the signal created by the 500nmol/l solution appears to be very weak.

Again, the imaging sequence with 3° angular stepping and 118 rotational positions was employed, as described for the phantom experiments. The sequence was run three times, for boundary extraction, and imaging at the excitation and emission wavelengths.

The generated finite element mesh is shown in figure 5.10b. Again, in a post processing step it was further refined toward the boundary for better source modeling during computation of Green's functions. Boundary elements were used in the reconstruction this time, as both inclusions were also located on the boundary. To restrict the number of unknowns, for reconstruction only vertices of the coarse mesh—as shown in figure 5.10b—were employed, but not vertices of further refined boundary cells. A total of 5200 elements / degrees of freedom were used in the reconstruction process. Once again, reconstructions were performed using 50 r-ART iterations and a relaxation of $\varrho = 0.1$.

In the reconstructed slice shown in figure 5.13b, both inclusions do appear close to the boundary of the animal having different intensities, although their intensities do not differ by a factor of two, but slightly less.

## 5.5. Discussion

In this chapter, a fully integrated imaging system for fluorescence mediated tomography of small animals was presented. The system can autonomously run different imaging sequences involving free positioning of the integrated laser source and rotation of the central imaging chamber. Images are acquired through a FireWire interface and stored on a personal computer for subsequent reconstruction. The system is equipped with animal handling facilities to safely keep imaged animals anesthetized.

The software environment developed for reconstruction enables the creation of non-degenerate finite element meshes having size and shape of the imaged object or animal. Green functions can be computed based on these meshes and used in the reconstruction process based on a linear perturbation approach as described previously in chapter 2.

The accuracy of the surface extraction and grid creation algorithm was demonstrated in phantoms and showed good agreement with the actual phantom shape (figure 5.10c). However, the phantoms used for calibration and accuracy measurements were cylindrical and thus of a very simple shape. It is therefore necessary to further investigate and validate the approach taken. However, when comparing white light images of an animal with the extracted surface, both seem to agree very well with each other, with the only exception of complex shaped body parts such as paws and ears (figure 5.8). Photon propagation through these parts, however, cannot be modeled by the diffusion equation: they are too thin to allow the scattering to become isotropic, and thus for the diffusion approximation to apply. In conclusion, these parts have to be removed from the field of view in any case.

The experiments performed with the system show the capabilities of acquiring and reconstructing high density data sets involving over 100 source positions. With 118 projections used, and $19 \times 3$ detectors for $\approx 33000$ voxels, the weight matrix involved contained already over 220 million entries. Still, data sets of this size could easily be handled with a standard PC. For the initial animal experiments presented herein, a smaller grid with only $\approx 5000$ elements was employed.

Experimental data was first acquired for the two-inclusion phantom. Shape and location of reconstructed inclusions showed good agreement with the actual experimental situation. However, it could be shown that calibration of the pinhole position used to model perspectivic projection in the detection operator ${}^{\mathrm{L}}\mathcal{P}^{i}_{\partial\Omega\to\mathcal{D}}$ is vital to obtain good results (figure 5.12). Still, this is a much easier calibration step than the calibration involved in fiber-based imaging, described in chapter 4.

An initial animal study demonstrated the feasibility of small animal imaging with the system presented herein. However, relatively high concentrations of dye had to be used. While the two superficially implanted inclusions reconstructed fairly

well, investigations involving deeper inclusions and also biological targets still have to be conducted. Especially the topic of quantification of concentration in heterogeneous diffusive media has to be addressed in more detail.

# Chapter 6.

# Discussion and Outlook

*Δός μοι πῦ στῶ, καὶ τὴν γῆν κινήσω*[*]

*(Archimedes)*

## 6.1. Discussion

In the work presented herein, the implications of non-contact tomographic imaging of fluorescent inclusions in turbid media were examined, and an appropriate imaging device for small animal imaging developed.

For the first time, to the author's best knowledge, a comparative study between fiber-based imaging and non-contact imaging was presented, where the same experimental conditions were exactly matched for both techniques. In both cases the source positions, the phantom geometry, the imaged surface area, as well as the number of detector values per source position were equal. By careful and laborious calibration, it was ensured that differences observed in reconstructed fluorochrome distributions should only be due to the different detection techniques used.

First of all, the experimental simplicity of non-contact imaging and the significantly simpler calibration procedures were practically demonstrated. As a second result, strong differences in image resolution and stability of the concentration estimation were observed. All results indicated that non-contact imaging could indeed be superior to classic techniques.

As the main reason for the improved quality of concentration estimation, the averaging effect of using many CCD pixels was identified. Using only individual pixels led to a deterioration in linearity and significantly increased the spread in concentration estimates to a level worse than results from fiber-based imaging.

As far as the resolution improvements were concerned, it was not possible to assign a single cause to that effect. Instead, several factors could be identified that negatively influenced the results for the fiber-based setup. These factors are (1) again the interpolation procedures possible using a large amount of individual pixels in CCD images for non-contact imaging, while there is only one detector reading

[*] "Give me a place to stand, and I shall move the Earth"

per fiber available; (2) the difference in signal dynamics for central to lateral fibers, decreasing signal to noise ratio for central fibers; and (3) possibly coupling effects not calibrated for.

Some authors argue that higher resolution can simply be achieved by collecting more and more information [39], and thus making the inverse problem increasingly complicated. Herein, it has been demonstrated that the size of the problem can be kept moderate by simply using a large number of pixel values to determine only very few virtual detector readouts by means of a interpolation routine using all available CCD pixels.

From the singular value analysis performed on the linear system used for reconstruction, it can furthermore be concluded that certain interpolation procedures might also regularize the system for fiber-based imaging. This could yield better looking results in some cases; however, for the experiments performed herein, no significant differences were observed which might indicate that the resulting differences in resolution do not originate from ill-conditioning.

The results regarding quantification capabilities and resolution improvement in the non-contact imaging case enabled subsequently the development of a small animal imaging system. The presented system had two major advantages over existing systems, (1) animals do not have to be compressed or positioned upside down, but can be imaged in a physiologically meaningful position, and (2) imaging can be performed using arbitrary source positions and projection angles.

Initial experiments showed the capabilities of the system with respect to an improved localization of fluorescent inclusions, as compared to the system used for the study described above. This can be assigned to the availability of more source positions (118 instead of 36), showing also the usefulness of more information that can be input into the linear solver. However, it must not be overlooked that arbitrarily increasing the number of sources and detectors will increase the size of the weight matrix and in the end will make the whole problem infeasible to solve.

## 6.2. Outlook

While the results presented herein are encouraging the use of non-contact imaging techniques, they at the same time only cast a streak of light into the jungle of unexplored imaging options.

It was shown that using only few virtual detector readings extracted from a large number of pixels can increase resolution and keep problem size small. However, no studies have been performed concerning how to optimize the number of source positions and detector readout values for optimal performance. Furthermore, the interpolation of pixel values as presented herein has only been performed

using bilinear interpolation functions on regular detector grids. Higher order functions, or irregular detector grids making better use of the information contained in the acquired images might result in further improvements.

Another point is imaging of heterogeneous tissues. While reconstructions of fluorescent inclusions or fluorescence labeled tumors in animal experiments have been presented by several authors [5, 24, 26, 40, 65, 96] and also for the imaging system presented herein, the linearity of concentration estimates and the accuracy of localization is still unclear. However, these investigations have to be performed before FMT can become a routine procedure in molecular imaging; if accurate quantification and localization cannot be guaranteed in heterogeneous media, the main reason for tomographic imaging would disappear.

# Appendix A.

# Technical Specifications of the Controller System

## A.1. Data and Control Cable Pinout

The following charts document the pinout for all control cables running between controller and imaging system described in chapter 5. Two cables are not described herein: the camera data and control cable, which was manufactured by Hamamatsu and has a proprietary, non-documented pinout, and the power supply for the laser diode, which was manufactured by LG LaserTechnologies GmbH.

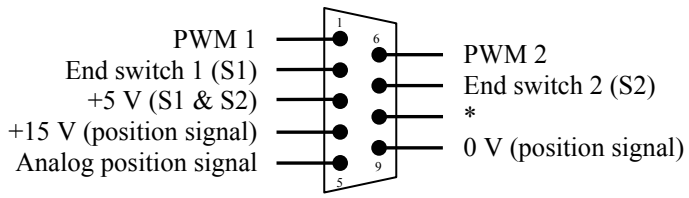


**(a)** Controller side: 9-pin SUB-D male plug

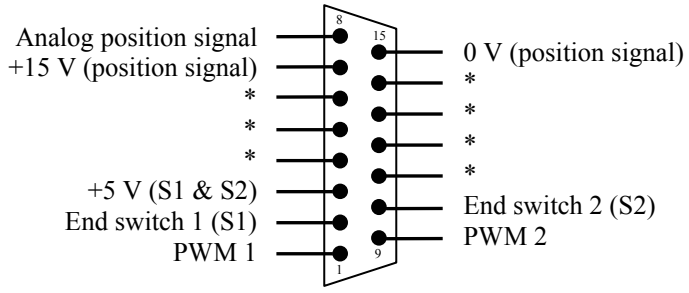


**(b)** Imaging chamber side: 15-pin SUB-D female plug

**Figure A.1:** Linear axis cable pinout

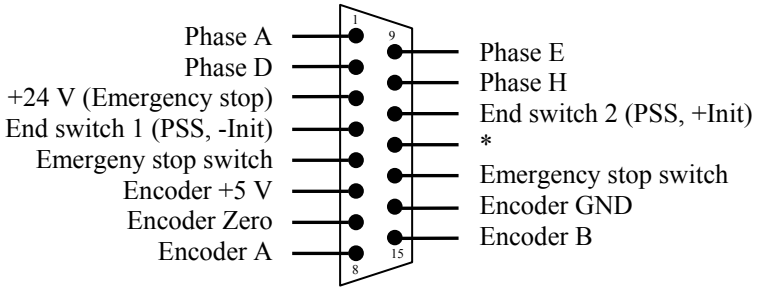


**Figure A.2:** Stepping motor cable pinout. 15-pin SUB-D plug, female (controller side) to male (imaging chamber connector).

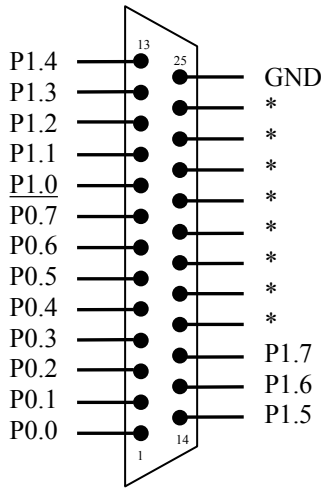


**Figure A.3:** I/O cable pinout. 25-pin SUB-D plug, male (controller side) to female (imaging chamber connector).

# A.2. Commands Supported by the Control System

| Command | Description |
|---|---|
| | **Interactive movement commands** |
| B | Stop all movements, break running program |
| C+ | Interactive commands to start linear axis movement to the right |
| C- | Interactive commands to start linear axis movement to the left |
| C0 | Interactive commands to stop linear axis |
| D | Dump program. This command will print the currently programmed sequence of movements in human readable form on the serial port |
| I | Initialize and calibrate system |
| | **Programming commands** |
| PS | Start programming mode |
| PE | End programming mode |
| | **Commands available during programming mode** |
| P1 *xx* | Set the first I/O port to the value given as hexadecimals |
| P2 *xx* | Set the second I/O port to the value given as hexadecimals |
| PD *xx* | Wait for *xx* seconds given as hexadecimals. If the number of seconds is zero (PD00), then the program waits for a single character sent by the host PC. |
| PL *xxxx* | Move to linear position given as hexadecimals |
| PP | Send position information to the host computer. Position information consists of eight hexadecimal digits: the first four give the position of the linear stage, the last four give the angular position. |
| PR *xxxx* | Move to angular position given as hexadecimals. Angles are given in Number of flanks of the quadrature encoder plus 10,000, i.e., values range between 10,000 (0°) and 50,000 (360°). |
| PT | Send trigger signal to camera to start acquisition. |
| PW | Wait for all current movements to finish. |
| | **Query system information** |
| QP | Query positions. Positions are transmitted in the same format as described for command PP. |
| QV | Query version number and program information of the controller program. This command can be used to see whether the controller has been started and to test the communication channel. |
| | **Program control** |
| RC | Continue program after it was temporarily stopped with RE. |
| RP | Run program—this command starts the execution of a previously transmitted program sequence. If the imaging system has not been initialized since power-on (by a I command), then prior to starting the program, initialization will be performed. |
| RS | Run single instruction. |
| RE | Stop program. |

## A.3. Example: Data Acquisition Sequence

The following excerpt demonstrates how to program the controller system. It is part of the sequence used for the experiments described in chapter 5. Here, the chamber is rotated by 3° in each step, and then an image is acquired, until a full rotation has been performed.

| Commands | Comment |
|---|---|
| PS | Start programming mode |
| PD 00 | Wait for a character from the host PC to start acquisition |
| PR 2710 | Rotate to position 0° (2710h = 10000, and this is defined as zero) |
| PW | Wait for rotation to finish |
| PT | Trigger image acquisition |
| PD 00 | Wait for host PC to acknowledge acquisition |
| PR 2AF8 | Rotate to position 3° (2AF8h = 11000, 1000 steps are equal to 3°) |
| PW | Wait for rotation to finish |
| PT | Trigger image acquisition |
| PD 00 | Wait again for host PC |
| PR 2EE0 | Rotate to 6° (2EE0h = 12000) |
| PW | Wait for rotation to finish |
| PT | Trigger image acquisition |
| ... | ..... |
| PD 00 | Wait again for host PC |
| PR BB80 | Rotate to 354° (BB80h = 48000) |
| PW | Wait for rotation to finish |
| PT | Trigger image acquisition |
| PD 00 | Wait again for host PC |
| PR 0000 | Rotate to initial position. If a position below 10000 (0°) is given, 10000 is assumed. |
| PW | Wait for movement to finish |
| PE | End programming mode—the program can now be executed. |

# List of Symbols and Expressions

## Acronyms

| | |
|---|---|
| ART | Algebraic Reconstruction Technique |
| CCD | Charge Coupled Device |
| CT | Computerized Tomography |
| DEAL.II | Discrete Element Analysis Library [21] |
| DOT | Diffuse Optical Tomography |
| EL | Electroluminescence |
| FEM | Finite Element Method |
| FMT | Fluorescence Mediated Tomography |
| FP | Fluorescent Protein |
| FWHM | Full Width Half Maximum |
| LAPACK | Linear Algebra Package [16] |
| MOBIIR | Model-based Iterative Image Reconstruction |
| NA | Numerical aperture |
| NIR | Near Infrared (this term is used for light of 600nm–900nm) |
| PDE | Partial Differential Equation |
| PWM | Pulse Width Modulation |
| RTE | Radiative Transfer Equation |
| SVD | Singular Value Decomposition |

## General notation

| | |
|---|---|
| $\mathbf{A}, \ldots, \mathbf{Z}$ | Matrices |
| $\mathbf{a}, \ldots, \mathbf{z}$ | Vectors in $\mathbb{R}^N$, $N$ arbitrary (depending on context) |

| | |
|---|---|
| $a, \ldots, z$ | Scalars or scalar functions |
| $(a,b)_\Omega$ | Scalar product within domain $\Omega$, as defined by $\int_\Omega a(\mathbf{r})\,b(\mathbf{r})\,d\mathbf{r}$ |
| $(a,b)_{\partial\Omega}$ | Scalar product on domain boundary $\partial\Omega$, as defined by $\int_{\partial\Omega} a(\mathbf{r})\,b(\mathbf{r})\,d\mathbf{r}$ |
| $A^{\mathrm{T}}$ | Matrix transpose of $\mathbf{A}$ |

## Greek Symbols

| | |
|---|---|
| $\delta_0$ | Dirac delta function |
| $\varepsilon$ | Molar extinction coefficient of the fluorochrome, $[\mathrm{Mol}^{-1}\mathrm{cm}^{-1}]$ |
| $\Phi^0$ | Solution to the homogeneous diffusion equation using $D^0$ and $\mu_a^0$ |
| $\delta\Phi$ | Change in photon density created by a perturbation in the optical coefficient functions |
| $\gamma$ | Quantum yield of the fluorochrome |
| $\lambda_m$ | Emission wavelength of a fluorochrome [nm] |
| $\lambda_x$ | Excitation wavelength of a fluorochrome [nm] |
| $\mu_a$ | Attenuation / absorption coefficient $[\mathrm{cm}^{-1}]$ |
| $\mu_a^0$ | Homogeneous background of attenuation coefficient $\mu_a$, $[\mathrm{cm}^{-1}]$ |
| $\delta\mu_a$ | Small perturbation of the homogeneous attenuation coefficient $\mu_a^0$, having unit $[\mathrm{cm}^{-1}]$ |
| $\mu_s$ | Scattering coefficient $[\mathrm{cm}^{-1}]$ |
| $\mu_s'$ | Reduced scattering coefficient, as defined by $\mu_s' = (1-g)\mu_s$, $[cm^{-1}$ |
| $\nu$ | Speed of light in the medium $[\mathrm{cm}\cdot\mathrm{s}^{-1}]$ |
| $\Omega$ | Spatial domain $\Omega \subseteq \mathbb{R}^3$ enclosing the diffuse medium |
| $\partial\Omega$ | Boundary of $\Omega$ |
| $\Phi$ | Photon density $[\mathrm{Photons}\cdot\mathrm{s}^{-1}\mathrm{cm}^{-2}]$ |
| $\widetilde{\Phi}(\mathbf{d})$ | Measured photon density |
| $\widehat{\Phi}(\mathbf{d})$ | Predicted photon density, i.e., $\widehat{\Phi} = \mathcal{P}\{\Phi\}$. |
| $\varrho$ | Relaxation parameter for ART-based matrix inversion |
| $\tau$ | Fluorescence lifetime [s] |

## Latin Symbols

| | |
|---|---|
| $c$ | Concentration of the fluorochrome, [Mol/l] |

| | |
|---|---|
| $\mathbb{D}$ | Detector space |
| $\mathbf{d}$ | A detector in detector space, $\mathbf{d} \in \mathbb{D}$ |
| $D$ | Diffusion length [cm] |
| $D^0$ | Homogeneous background of diffusion length $D$, [cm] |
| $g$ | Anisotropy of scattering, $-1 \leq g \leq 1$, where $g = \langle \mathbf{s} \cdot \mathbf{s}' \rangle$ for photons that scatter from $\mathbf{s}$ to $\mathbf{s}'$ |
| $G(\mathbf{r}, \mathbf{r}_s)$ | Homogeneous Green's function defined by $\left[-D^0\nabla^2 + \mu_a^0\right] G(\mathbf{r}, \mathbf{r}_s) = \delta_0(\mathbf{r} - \mathbf{r}_s)$ |
| $\mathbf{Id}$ | Identity matrix |
| $\mathscr{L}$ | Any differential operator |
| $\mathbb{M}$ | Measurement space; function vector space spanned by measurement predictions $\widehat{\Phi}$. |
| $p(\mathbf{r}, \mathbf{s}, \mathbf{s}')$ | Scattering probability kernel, defines the probability at $\mathbf{r}$ that a photon scatters from $\mathbf{s}$ to $\mathbf{s}'$ |
| $\mathcal{P}_{\Omega \to \Omega}$ | Full domain measurement operator |
| $\mathcal{P}_{\partial\Omega \to \partial\Omega}$ | Boundary measurement operator |
| $\mathcal{P}_{\partial\Omega \to \mathbf{r}_b}$ | Point-like measurement operator |
| $\mathcal{P}_{\partial\Omega \to \mathbf{r}_b \pm \rho}$ | Finite-area measurement operator for a cylindrical fiber of radius $\rho$ |
| $\mathcal{P}^i_{\partial\Omega \to \partial\Omega}$ | Interpolated fiber-based measurement operator |
| ${}^{\mathrm{F}}\mathcal{P}^i_{\partial\Omega \to \mathcal{D}}$ | Ripoll's non-contact operator using depth-of-field effects but using a telecentric lens / fiber bundle, as described in [2] |
| ${}^{\mathrm{L}}\mathcal{P}^i_{\partial\Omega \to \mathcal{D}}$ | Simplified non-contact operator for lens-based systems |
| $q$ | Source emitting inside the domain $\Omega$. For the RTE, the unit is [Photons$\cdot$ $\mathrm{s}^{-1}\mathrm{cm}^{-2}\mathrm{sr}^{-1}$], while for the diffusion equation, it is [Photons$\cdot\mathrm{s}^{-1}\mathrm{cm}^{-2}$]. |
| $\mathbf{r}$ | Coordinate within the diffuse domain, $\mathbf{r} \in \Omega$ |
| $\mathbf{r}_b$ | Point on the domain boundary, i.e., $\mathbf{r}_b \in \partial\Omega$ |
| $\mathbf{s}$ | Direction of propagating photon; $\mathbf{s}$ is a vector on the unit sphere, i.e., $\mathbf{s} \in S$ |
| $S$ | The unit sphere, i.e. $S = \left\{\mathbf{s} \in \mathbb{R}^3 \mid \|\mathbf{s}\|^2 = 1\right\}$ |
| $t$ | Time [s] |
| $u$ | Photon radiance [Photons $\cdot\, \mathrm{cm}^{-2}\mathrm{s}^{-1}\mathrm{sr}^{-1}$]. The equivalent of $u$ in the diffusion equation, the photon density, is given by $\Phi$ ( see there). |

| | |
|---|---|
| $\mathbf{W}$ | Weight matrix in the linear reconstruction problem |

# List of Figures

# Bibliograpy

## Own Contributions

This is a list of contributions by the author of this thesis, in chronological order.

### Peer-Reviewed Publications


[1] A. Altmann, R. B. Schulz, G. Glensch, H. Eskerski, S. Zitzmann, M. Eisenhut, and U. Haberkorn. Effects of Pax8 and TTF-1 thyroid transcription factor gene transfer in hepatoma cells: Imaging of functional protein-protein interaction and iodide uptake. *Journal of Nuclear Medicine*, 46:831–839, 2005.

[2] J. Ripoll, R. B. Schulz, and V. Ntziachristos. Free-space propagation of diffuse light: Theory and experiments. *Physical Review Letters*, 91:103901, 2003.

[3] R. B. Schulz, C. D'Andrea, G. Valentini, R. Cubeddu, J. Peter, and W. Semmler. Comparison of noncontact and fiber-based fluorescence-mediated tomography. *Optics Letters*, 31:769–771, 2006.

[4] R. B. Schulz, J. Ripoll, and V. Ntziachristos. Non-contact optical tomography of turbid media. *Optics Letters*, 28:1701–1703, 2003.

[5] R. B. Schulz, J. Ripoll, and V. Ntziachristos. Experimental fluorescence tomography of tissues with noncontact measurements. *IEEE Transactions on Medical Imaging*, 23:492–500, 2004.

[6] R. B. Schulz and W. Semmler. Principles of optical and fluorescence mediated tomography in turbid media. *Zeitschrift für Medizinische Physik*, 15:177–186, 2005.


### Selected Proceedings Papers


[7] V. Ntziachristos, E. E. Graves, R. B. Schulz, and J. Ripoll. Fluorescence molecular tomography: New detection schemes for acquiring high information con-

tent measurements. In *IEEE International Symposium on Biomedical Imaging: From Macro to Nano*, volume 2, pages 1475–1478. IEEE, 2004.

[8] J. Peter, H. Ruehle, V. Stamm, R. B. Schulz, M.F. Smith, B. Welch, V. Popov, B. Kross, R. Wojcik, A. Weisenberger, S. Majewski, and W. Semmler. Development and initial results of a dual-modality SPECT/optical small animal imager. In *Nuclear Science Symposium Conference Record*, volume 4, pages 1969–1972. IEEE, 2005.

[9] J. Peter and R. B. Schulz. Time-resolved monte carlo simulation of optical and isotopic photons in hybrid phantoms. In *Nuclear Science Symposium Conference Record*, volume 5, pages 2926–2928. IEEE, 2004.

[10] J. Peter, R. B. Schulz, and W. Semmler. PET-MOT—a novel concept for simultaneous positron and optical tomography in small animals. In *Nuclear Science Symposium Conference Record*, volume 3, pages 1757–1760. IEEE, 2005.

[11] J. Ripoll, R. B. Schulz, and V. Ntziachristos. Noncontact diffuse optical tomography. In V. V. Tuchin, editor, *Saratov Fall Meeting 2003: Optical Technologies in Biophysics and Medicine V*, volume 5474 of *Proceedings of SPIE*, pages 215–223. SPIE, 2004.

[12] R. B. Schulz, W. Bangerth, J. Peter, and W. Semmler. Independent modeling of fluorescence excitation and emission with the finite element method. In *Proceedings of the OSA BIOMED topical meeting*, 2004.

[13] R. B. Schulz, G. Echner, H. Ruehle, W. Stroh, J. Vierling, T. Vogt, J. Peter, and W. Semmler. Development of a fully rotational non-contact fluorescence tomographer for small animals. In *Nuclear Science Symposium Conference Record*, volume 4, pages 2391–2393. IEEE, 2005.

[14] R. B. Schulz, J. Peter, W. Semmler, C. D'Andrea, G. Valentini, and R. Cubeddu. Quantifiability and image quality in noncontact fluorescence tomography. In K. Licha and R. Cubeddu, editors, *Photon Migration and Diffuse-Light Imaging II*, volume 5859 of *Proceedings of the SPIE*. SPIE, 2005.

[15] R. B. Schulz, J. Ripoll, D. Yessayan, and V. Ntziachristos. Non-contact fluorescence molecular tomography (FMT) of small animals. In *Proceedings of the OSA BIOMED topical meeting*, 2004.

# Other References

[16] E. Anderson, Z. Bai, C. Bischof, S. Blackford, J. Demmel, J. Dongarra, J. Du Croz, A. Greenbaum, S. Hammarling, A. McKenney, and D. Sorensen. *LAPACK User's Guide*. Society for Industrial and Applied Mathematics, Philadelphia, PA, third edition, 1999.

[17] D. S. Anikonov, A. E. Kovtanyuk, and I. V. Prokhorov. *Transport Equation and Tomography*. VSP, Leiden, 2002.

[18] R. Aronson. Boundary conditions for diffusion of light. *Journal of the Optical Society of America A*, 12:2532–2539, 1995.

[19] S. R. Arridge. Optical tomography in medical imaging. *Inverse Problems*, 15:R41–R93, 1999.

[20] W. Bangerth. *Adaptive Finite Element Methods for the Identification of Distrbuted Parameters in Partial Differential Equations*. PhD thesis, University of Heidelberg, Faculty of Physics, 2001.

[21] W. Bangerth, R. Hartmann, and G. Kanschat. deal.II differential equations analysis library, technical reference. web page, 2005. http://www.dealii.org.

[22] F. G. Blankenberg. Molecular imaging: the latest generation of contrast agents and tissue characterization techniques. *Journal of Cellular Biochemistry*, 90:443–453, 2003.

[23] A. Y. Bluestone, G. Abdoulaev, C. H. Schmitz, R. L. Barbour, and A. H. Hielscher. Three-dimensional optical tomography of hemodynamics in the human head. *Optics Express*, 9:272–286, 2001.

[24] A. Y. Bluestone, M. Stewart, J. Lasker, G. Abdoulaev, and A. H. Hielscher. Three-dimensional optical tomographic brain imaging in small animals, part 1: hypercapnia. *J.Biomed.Opt.*, 9:1046–1062, 2004.

[25] D. A. Boas, D. H. Brooks, E. L. Miller, C. A. DiMarzio, M. Kilmer, R. J. Gaudette, and Q. Zhang. Imaging the body with diffuse optical tomography. *IEEE Signal Processing Magazine*, 18:57–75, 2001.

[26] B. A. Brooksby, H. Dehghani, B. W. Pogue, and K. D. Paulsen. Near-infrared (nir) tomography breast image reconstruction with a priori structural information from MRI: Algorithm development for reconstructing heterogeneities. *IEEE Journal of Selected Topics in Quantum Electronis*, 9:199–209, 2003.

[27] J. P. Culver, R. Choe, M. J. Holboke, L. Zubkov, T. Durduran, A. Slemp, V. Ntziachristos, B. Chance, and A. G. Yodh. Three-dimensional diffuse optical tomography in the parallel plane transmission geometry: Evaluation of a hybrid frequency domain/continuous wave clinical system for breast imaging. *Medical Physics*, 30:235–347, 2003.

[28] J. P. Culver, T. Durduran, D. Furuya, C. Cheung, J. H. Greenberg, and A. G. Yodh. Diffuse optical tomography of cerebral blood flow, oxygenation and metabolism in rat during focal ischemia. *Journal of Cerebral Blood Flow & Metabolism*, 23:911–924, 2003.

[29] J. P. Culver, V. Ntziachristos, M. J. Holboke, and A. G. Yodh. Optimization of optode arrangements for diffuse optical tomography. *Optics Letters*, 26:701–703, 2001.

[30] S. Del Bianco, F. Martelli, F. Cignini, G. Zaccanti, G. Sansone, A. Pifferi, A. Torricelli, A. Bassi, P. Taroni, and R. Cubeddu. Liquid phantom for investigating light propagation through layered diffusive media. *Optics Express*, 12:2102, 2004.

[31] D. T. Delpy and M. Cope. Quantification in tissue near-infrared spectroscopy. *Philosophical Transactions of the Royal Society of London Series B—Biological Sciences*, 352:649–659, 1997.

[32] R. M. P. Doornbros, R. Lang, M. C. Aalders, F. W. Cross, and H. J. C. M. Sterenborg. The determination of in vivo human tissue optical properties and absolute chromophore concentrations using spatially resolved steady-state diffuse reflectance spectroscopy. *Physics in Medicine and Biology*, 44:967–981, 1999.

[33] A. Dunn. *Light Scattering Properties of Cells*. PhD thesis, University of Texas at Austin, Biomedical Engineering, 1997.

[34] M. J. Eppstein, D. J. Hawrysz, A. Godavarty, and E. M. Sevick-Muraca. Three-dimensional, bayesian image reconstruction from sparse and noisy data sets: Near-infrared fluorescence tomography. *Proceedings of the National Academy of Science*, 99:9619–9624, 2002.

[35] M. Firbank, M. Oda, and D. T. Delpy. An improved design for a stable and reproducible phantom material for use in near-infrared spectroscopy and imaging. *Physics in Medicine and Biology*, 40:955–961, 1995.

[36] D. F. Gleason. Classification of prostate carcinomas. *Cancer Chemotherapy Reports*, 50:125–128, 1966.

[37] A. Godavarty, A. B. Thompson, R. Roy, M. Gurfinkel, M. J. Eppstein, C. Zhang, and E. M. Sevick-Muraca. Diagnostic imaging of breast cancer using fluorescence-enhanced optical tomography: phantom studies. *J.Biomed.Opt.*, 9:488–496, 2004.

[38] E. E. Graves, J. P. Culver, J. Ripoll, R. Weissleder, and V. Ntziachristos. Singular-value analysis and optimization of experimental parameters in fluorescence molecular tomography. *Journal of the Optical Society of America A*, 21:231–241, 2004.

[39] E. E. Graves, J. Ripoll, R. Weissleder, and V. Ntziachristos. A sub-millimeter resolution fluorescence molecular imaging system for small animal imaging. *Medical Physics*, 30:901–911, 2003.

[40] E. E. Graves, R. Weissleder, and V. Ntziachristos. Fluorescence molecular imaging of small animal tumor models. *Curr.Mol.Med.*, 4:419–430, 2004.

[41] U. Hampel, E. Schleicher, and R. Freyer. Volume image reconstruction for diffuse optical tomography. *Applied Optics*, 41:3816–3826, 2002.

[42] R. C. Haskell, L. O. Svaasand, T. T. Tsay, T. C. Feng, M. S. McAdams, and B. Tromberg. Boundary conditions for the diffusion equation in radiative transfer. *J.Opt.A—Pure Appl.Opt.*, 11:2727–2741, 1994.

[43] J. C. Hebden, A. Gibson, R. M. Yusof, N. Everdell, E. M. C. Hillman, D. T. Delpy, S. R. Arridge, T. Austin, J. H. Meek, and J. S. Wyatt. Three-dimensional optical tomography of the premature infant brain. *Physics in Medicine and Biology*, 47:4155–4166, 2002.

[44] E. Hecht. *Optics*, volume 4th edition. Addison-Wesley, Boston, 2002.

[45] L. Henyey and J. Greenstein. Diffuse radiation in the galaxy. *Astrophysics Journal*, 93:70–83, 1941.

[46] T. Heyduk and E. Heyduk. Molecular beacons for detecting DNA binding proteins. *Nature Biotechnology*, 20:171–176, 2002.

[47] A. H. Hielscher, R. E. Alcouffe, and R. L. Barbour. Comparison of finite-difference transport and diffusion calculations for photon migration in homogeneous and heterogeneous tissues. *Physics in Medicine and Biology*, 43:1285–1302, 1998.

[48] X. Intes, V. Ntziachristos, J. P. Culver, A. G. Yodh, and B. Chance. Projection access order in algebraic reconstruction technique for diffuse optical tomography. *Physics in Medicine and Biology*, 47:N1–N10, 2002.

[49] A. Joshi, W. Bangerth, J. Hwang, K. ans Rasmussen, and E. M. Sevick-Muraca. Plane-wave fluorescence tomography with adaptive finite elements. *Optics Letters*, 31:193–195, 2006.

[50] A. C. Kak and M. Slaney. *Principles of Computerized Tomographic Imaging*. Society of Industrial and Applied Mathematics, 2002.

[51] M. Keijzer, W. M. Star, and P. R. Storchi. Optical diffusion in layered media. *Applied Optics*, 27:1820–1824, 1988.

[52] A. Kienle, F. K. Forster, R. Diebolder, and R. Hibst. Light propagation in dentin: influence of microstructure on anisotropy. *Physics in Medicine and Biology*, 48:N7–N14, 2003.

[53] A. Kienle, F. K. Forster, and R. Hibst. Anisotropy of light propagation in biological tissue. *Optics Letters*, 29:2617–2619, 2004.

[54] M. King and T. Farncombe. An overview of attenuation and scatter correction of planar and SPECT data for dosimetry studies. *Cancer Biother. Radiopharm.*, 18:181–190, 2003.

[55] A. D. Klose and H. Hielscher. Fluorescence tomography with simulated data based on the equation of radiative transfer. *Optics Letters*, 28:1019–1021, 2003.

[56] K. Licha, C. Hessenius, A. Becker, P. Henklein, M. Bauer, S. Wisniewski, B. Wiedenmann, and W. Semmler. Synthesis, characterization, and biological properties of cyanine-labeled somatostatin analogues as receptor-targeted fluorescent probes. *Bioconjugate Chemistry*, 12:44–50, 2001.

[57] D. S. Lidke, P. Nagy, R. Heintzmann, D. J. Arndt-Jovin, J. N. Post, H. E. Grecce, E. A. Jares-Erijman, and T. M. Jovin. Quantum dot ligands provide new insights into erbB/HER receptor-mediated signal transduction. *Nature Biotechnology*, 22:198–203, 2004.

[58] W. E. Lorensen and H. E. Cline. Marching cubes: A high resolution 3D surface construction algorithm. *Computer Graphics*, 21:163–169, 1987.

[59] T. Massoud and S. S. Gambhir. Molecular imaging in living subjects: Seeing fundamental biological processes in a new light. *Genes and Development*, 17:545–580, 2003.

[60] A. B. Milstein, S. Oh, K. J. Webb, C. A. Bouman, Q. Zhang, D. A. Boas, and R. P. Millane. Fluorescence optical diffusion tomography. *Applied Optics*, 42:3081–3094, 2003.

[61] J. Mobley and T. Vo-Dinh. Optical properties of tissue. In *Biomedical Photonics Handbook [89]*, pages 2.1–2.75, 2003.

[62] M.-A. Mycek and B. W. Pogue, editors. *Handbook of Biomedical Fluorescence*. Marcel Dekker, 2003.

[63] M. Nieto-Vesperinas. *Scattering and Diffraction in Physical Optics*. John Wiley and Sons, New York, 1991.

[64] S. J. Norton and T. Vo-Dinh. Theoretical models and algorithms in optical diffusion tomography. In *Biomedical Photonics Handbook [89]*, pages 4.1–4.24, 2003.

[65] V. Ntziachristos, A. H. Hielscher, A. G. Yodh, and B. Chance. Diffuse optical tomography of highly heterogeneous media. *IEEE Transactions on Medical Imaging*, 20:470–478, 2001.

[66] V. Ntziachristos, J. Ripoll, and R. Weissleder. Would near-infrared fluorescence signal propagate through large human organs for clinical studies? *Optics Letters*, 27:333–335, 2002.

[67] V. Ntziachristos, E. A. Schellenberger, J. Ripoll, D. Yessayan, E. E. Graves, A. Bogdanov, L. Josephson, and R. Weissleder. Visualization of antitumor treatment by means of fluorescence molecular tomography with an Annexin V-Cy5.5 conjugate. *Proceedings of the National Academy of Science*, 101:12294–12299, 2004.

[68] V. Ntziachristos, C. H. Tung, C. Bremer, and R. Weissleder. Fluorescence-mediated tomography resolves protease activity in vivo. *Nature Medicine*, 8:757–760, 2002.

[69] V. Ntziachristos, G. Turner, J. Dunham, S. Windsor, A. Soubret, J. Ripoll, and H. A. Shih. Planar fluorescence imaging using normalized data. *J.Biomed.Opt.*, 10:064007, 2005.

[70] V. Ntziachristos and R. Weissleder. Experimental three-dimensional fluorescence reconstruction of diffuse media by use of a normalized born approximation. *Optics Letters*, 26:893–895, 2001.

[71] M. S. Patterson, B. Chance, and B. C. Wilson. Time resolved reflectance and transmittance for the non-invasive measurement of tissue optical properties. *Applied Optics*, 28:2331–2336, 1989.

[72] Y. L. Pei, H. L. Graber, and R. L. Barbour. Normalized-constraint algorithm for minimizing inter-parameter crosstalk in DC optical tomography. *Optics Express*, 9:97–109, 2001.

[73] A. Petrovsky, E. Schellenberger, L. Josephson, R. Weissleder, and A. Bogdanov. Near-infrared fluroescent imaging of tumor apoptosis. *Canc. Res.*, 63:1936–1942, 2003.

[74] P. Ray, H. Pimenta, R. Paulmurugan, F. Berger, M. E. Phelps, M. Iyer, and S. S. Gambhir. Noninvasive quantitative imaging of protein-protein interactions in living subjects. *Proceedings of the National Academy of Science*, 99:3105–3110, 2002.

[75] R. W. Redmond. Introduction to fluorescence and photophysics. In *Handbook of Biomedical Fluorescence [62]*, pages 1–28, 2003.

[76] J. Ripoll. *Light Diffusion in Turbid Media with Biomedical Applications*. PhD thesis, Universidad Autónoma de Madrid, 2000.

[77] J. Ripoll, M. Nieto-Vesperinas, R. Weissleder, and V. Ntziachristos. Fast analytical approximation for arbitrary geometries in diffuse optical tomography. *Optics Letters*, 27:527–529, 2002.

[78] J. Ripoll, V. Ntziachristos, R. Carminati, and M. Nieto-Vesperinas. Kirchhoff approximation for diffusive waves. *Physical Review E*, 64:051917, 2001.

[79] M. Rudin and R. Weissleder. Molecular imaging in drug discovery and development. *Nature Reviews*, 2:123–131, 2003.

[80] R. Sanchez and N. J. McCormick. A review of neutron transport approximations. *Nuclear Science and Engineering*, 80:481–535, 1982.

[81] M. Schweiger, S. R. Arridge, M. Hiraoka, and D. T. Delpy. The finite element method for the propagation of light in scattering media: Boundary and source conditions. *Medical Physics*, 22:1779–1792, 1995.

[82] N. C. Shaner, P. A. Steinbach, and R. Y. Tsien. A guide to choosing fluorescent proteins. *Nature Methods*, 2:905–909, 2005.

[83] J. R. Smyth and D. L. Bish. *Crystal Structures and Cation Sites in the Rock-Forming Minerals*. Unwin Hyman, 1988.

[84] L. H. Sobin and Ch. Wittekind, editors. *TNM Classification of Malignant Tumours*. John Wiley and Sons, 6th edition, 2002.

[85] D. N. Stratis-Cullum, D. L. Stokes, B. M. Cullum, J.-M. Song, P. M. Kasili, R. Jagannathan, J. Mobley, and T. Vo-Dinh. Spectroscopic data of biologically and medically relevant species and samples. In *Biomedical Photonics Handbook [89]*, pages 65.1–65.136, 2003.

[86] R. Y. Tsien. Imagining imaging's future. *Nature Reviews Molecular Cell Biology*, 4:SS16–SS21, 2002.

[87] M. U. Vera and D. J. Durian. Angular distribution of diffusively transmitted light. *Physical Review E*, 53:3215–3224, 1996.

[88] M. U. Vera, P. A. Lemieux, and D. J. Durian. Angular distribution of diffusely backscattered light. *Journal of the Optical Society of America A*, 14:2800–2808, 1997.

[89] T. Vo-Dinh, editor. *Biomedical Photonics Handbook*. CRC Press, 2003.

[90] D. J. Wagenaar, R. Weissleder, and A. Hengerer. Glossary of molecular imaging terminology. *Acad.Radiol.*, 8:409–420, 2001.

[91] G. Wagnières, S. Cheng, M. Zellweger, N. Utke, D. Braichotte, J. P. Ballini, and H. van den Bergh. An optical phantom with tissue-like properties in the visible for use in PDT and fluorescence spectroscopy. *Physics in Medicine and Biology*, 42:1415–1426, 1997.

[92] R. Weissleder. Scaling down imaging: Molecular mapping of cancer in mice. *Nature Reviews Cancer*, 2:11–18, 2002.

[93] R. Weissleder and V. Ntziachristos. Shedding light onto live molecular targets. *Nature Medicine*, 9:123–128, 2003.

[94] P. Winnard and V. Raman. Real time non-invasive imaging of receptor-ligand interactions in vivo. *Journal of Cellular Biochemistry*, 90:454–463, 2003.

[95] X. Wu, H. Liu, J. Liu, K. N. Haley, J. A. Treadway, J. P. Larson, N. Ge, F. Peale, and M. P. Bruchez. Immunofluorescent labeling of cancer marker Her2 and other cellular targets with semiconductor quantum dots. *Nature Biotechnology*, 21:41–46, 2003.

[96] G. Zacharakis, H. Kambara, H. Shih, J. Ripoll, J. Grimm, Y. Saeki, R. Weissleder, and V. Ntziachristos. Volumetric tomography of fluorescent proteins through small animals in vivo. *Proceedings of the National Academy of Science*, 102:18252–18257, 2005.